

ENHANCING LASER-DRIVEN PROTON ACCELERATION THROUGH COMPUTATIONAL METHODS

DISSERTATION

Presented in Partial Fulfillment of the Requirements for the Degree Doctor of
Philosophy in the Graduate School of The Ohio State University

By

Ronak Desai, B.S., M.S.

Graduate Program in Physics

The Ohio State University

May 2025

Dissertation Committee:

Professor Chris Orban, Advisor

Professor Douglass Schumacher

Professor Alexandra Landsman

Professor Brian Skinner

© Copyright by

Ronak Desai

May 2025

ABSTRACT

When an ultra-intense laser irradiates a thin (around a micron in thickness) and flat target, highly energetic protons emerge from the back of the target. Since these protons are primarily accelerated in the target normal direction, this phenomena is often called target normal sheath acceleration (TNSA). The sheath refers to the cloud of laser-heated electrons that drive the protons forward via strong electrostatic forces. Due to their unique properties, proton beams have a wide variety of applications like proton therapy for cancer, materials characterization, and radiography. Additionally, the extremely short timescales and high intensities of modern lasers give these beams certain characteristics that conventional beams from linear accelerators do not have. Furthermore, the laser facilities accelerate protons over a much smaller distance compared to conventional accelerators which has potential space (and cost) savings. Unfortunately, modern laser facilities are not able to produce TNSA proton beams of sufficient quality for many of these applications. The ideal proton beam should consist of a significant number of high energy protons that are well collimated in one direction. Due to the highly complex nature of laser-matter interactions, it is often unclear exactly how one might find such a beam.

In this work, I explore various ways to optimize the properties of TNSA beams. First, an incident laser beam is split in two equal energy pulses that irradiate the target at angles above and below the target normal direction. The constructive interference of the laser fields at the target front enhances both the maximum proton energy and beam collimation in a process termed enhanced target normal sheath acceleration. I explored this mechanism through computational particle-in-cell simulations in a complementary effort to an experimental effort at the Titan Laser early in 2024. Next, I borrowed and modified an existing proton acceleration model in the literature that predicts a TNSA proton energy distribution based on various target and laser parameters. From this, a synthetic dataset was constructed that enabled comparison of various machine learning algorithms in proof-of-principle optimization efforts. Finally, I had the opportunity to test out some of the lessons learned on the synthetic data to real data collected at the Wright-Patterson Air Force Base. There, I wrote code to parse data collected from a laser run where multiple laser parameters were varied. From this data, I sent instructions back to the control

system to automatically choose an optimal set of input parameters by using machine learning algorithms. While these machine learning efforts are certainly in preliminary stages, high repetition rates of both modern ultra-intense lasers and liquid targets provide a fertile ground for future optimizations.

Dedicate to ...

ACKNOWLEDGMENTS

I would like to thank my ...

VITA

September 2015 - May 2019	B.S. Physics, B.A. Mathematics, Rowan University, Glassboro, NJ
August 2020 - July 2021	Graduate Fellow, The Ohio State University, Columbus, OH
August 2021 - April 2023	Graduate Teaching Associate, The Ohio State University, Columbus, OH
May 2023 - August 2023	Graduate Research Associate, The Ohio State University, Columbus, OH
August, 2023	M.S. Physics, The Ohio State University, Columbus, OH
August 2023 - December 2024	Graduate Research Associate, The Ohio State University, Columbus, OH
January 2025 - May 2025	Graduate Teaching Associate, The Ohio State University, Columbus, OH

Publications

Applying Machine Learning Methods to Laser Acceleration of Protons: Lessons Learned from Synthetic Data

Towards Automated Learning with Ultra-Intense Laser Systems Operating in the kHz Repetition Rate Regime

Intelligent Control of MeV Electrons and Protons

Can Two Pulses Enhance Proton and Electron Acceleration?

Fields of Study

Major Field: Physics

Table of Contents

	Page
Abstract	ii
Dedication	iv
Acknowledgments	v
Vita	vi
List of Figures	xi
List of Tables	xvii

Chapters

1 Introduction	1
1.1 Lasers	1
1.2 Applications	4
1.2.1 Proton Therapy	5
1.2.2 Proton Radiography and Laser Fusion	7
1.2.3 Materials Characterization	9
1.3 Outline	10
2 Physics Background	12
2.1 Electric Fields	12
2.1.1 Gaussian Laser	12
2.1.2 Single Particle Motions	14
2.2 Plasma Physics	15
2.2.1 Plasma Electron Oscillations	16
2.2.2 Fluid Model	17
2.2.3 Plasma Conditions	19
2.3 Absorption of Energy	19
2.3.1 Critical Density	19
2.3.2 Absorption Mechanisms	20
2.4 Ion Acceleration	24
2.4.1 Target Normal Sheath Acceleration	25
2.4.2 Other Acceleration Mechanisms	28
3 Computational Methods	30
3.1 The Particle-In-Cell Method	30
3.1.1 Densities and Shape Factors	31

3.1.2	Field Solver and Particle Push	32
3.2	Machine Learning	34
3.2.1	Pre-processing	35
3.2.2	Model Selection	36
3.2.3	Model Types	37
4	Particle-in-Cell Simulations of Enhanced Target Normal Sheath Acceleration	41
4.1	Background	41
4.1.1	Spatially Aligned Pulses	41
4.1.2	Enhanced TNSA from Ferri et. al.	43
4.1.3	Other eTNSA Simulations	45
4.1.4	Recent Experiments	45
4.2	Titan Experiment	46
4.2.1	Gold Simulations	47
4.2.2	Comparison to Experiment	52
4.3	Discussion	53
5	Machine Learning Methods Applied to Synthetic Ion Acceleration Data	55
5.1	Modified Fuchs et. al. Model	56
5.1.1	Plasma Expansion into a Vacuum	56
5.1.2	Modified Fuchs Model	60
5.1.3	Further Model Modifications	61
5.2	First Analysis	63
5.2.1	Methods	64
5.2.2	Results	65
5.2.3	Optimization Task	68
5.3	Second Analysis	70
5.3.1	Methods	70
5.3.2	Results	72
5.3.3	Optimization Task	72
5.3.4	Constrained Data Campaign	75
5.4	Conclusion	79
6	Optimization and Control of a kHz Laser System	81
6.1	Background	82
6.1.1	Experimental Chamber	82
6.1.2	Data Sources	85
6.2	Optimization Experiments	87
6.2.1	Automated Data Extraction	88
6.2.2	Optimization Feedback Loop	90
6.3	Conclusion	91
7	Conclusion	94
	Bibliography	96

Appendices

A Energy Conservation in EPOCH Particle-in-Cell Simulations Due to Finite Numbers of Particles	107
A.1 Background	107
A.1.1 Electric Field Fluctuations	107
A.1.2 Empirical Heating Estimates	108
A.2 Simulation	109
A.2.1 Methods	109
A.2.2 Results	109
A.3 Conclusion	115

List of Figures

Figure	Page
1.1 The components of a laser are depicted which include the pump source, active laser medium, and optical cavity. Image source: [1].	2
1.2 The stretch, amplification, and compression stages of chirped pulse amplification are depicted. Taken from [2].	3
1.3 History of focused laser intensities from the inception of the laser in 1960. The graph is labeled with intensity regimes, technological milestones, and acronyms of laser facilities. Taken from Figure 4 in Yakovlev [3].	4
1.4 The dose delivered as a function of depth traveled in water for two types of beams are depicted – 200 MeV protons and 16 MV x-rays. Taken from Figure 1 in Mohan [4].	6
1.5 Visualization of two different approaches to laser fusion are depicted at the top. Lasers can irradiate the inside of a hollow gold can (called a hohlraum) to indirectly heat a fusion capsule or instead directly heat it. At the bottom, multiple stages of the fusion process are depicted including capsule ablation, compression, and burn. Taken from Figure 1 of Betti et al. [5].	8
1.6 Mass concentrations of three metal alloys are shown using two different techniques: Energy Dispersive x-ray Fluorescence (EDF) and X-ray and Particle-Induced Fluorescence. Taken from Figure 4 of Boivin et al. [6].	10
2.1 The intensity profile of a gaussian beam with laser parameters seen in the Extreme Light Laboratory at Wright-Patterson Air Force Base ($\lambda = 0.8\mu\text{m}$, $I_0 = 5 \times 10^{18} \text{ W cm}^{-2}$, $w_0 = 1.5 \mu\text{m}$, $\tau_{\text{FWHM}} = 40\text{fs}$). The beam radii w_0 and $w(x_R)$ are displayed in addition to the rayleigh range x_R	13
2.2 An initially charge-neutral plasma is depicted on the left. On the right, the electrons are displaced by a distance x creating a charge separation and electric field akin to a parallel-plate capacitor directed towards the right. Adapted from Smith [7].	16
2.3 Visualization of the electric potential as a function of radial distance away from a positive point charge at the origin in three scenarios: vacuum (left), plasma (center), ideal conductor (right). Brighter colors show a higher value of ϕ . In the center panel, the debye length λ_D is shown.	18

2.4	Absorption fraction as a function of incidence angle θ_i . For resonance absorption, the density scale length L_p is varied in terms of the laser wavelength $\lambda = 0.8 \mu\text{m}$. For the Brunel mechanism, fractions are plotted for two regimes $a_0 \ll 1$ (where a value of $a_0 = 0.1$ was chosen) and for $a_0 \gg 1$ (which has no dependence on a_0)	22
2.5	Experimentally recorded hot electron temperatures as a function of irradiance $I\lambda^2$ are plotted as red squares. The empirical scaling models are given by Wilks [8](pink, solid), Gibbon and Bell [9](blue, ashed), Forslund et. al. [10](green, dash-dot), and Brunel [11](black, dotted). Figure is taken from Gibbon [12]	25
2.6	The target normal sheath acceleration process is depicted. First, an intense laser pulse irradiates the front side of a target foil of few μm thickness. This generates hot electrons that stream through the foil and re-emerge in a cloud on the rear side. The charge separation of the hot electrons and positively charged target creates intense longitudinal fields ($\sim \text{TV/m}$) that accelerate light ions in the mostly target normal direction. This figure was taken from Roth [13]	26
2.7	The regimes of three different acceleration mechanisms are displayed in terms of eq. (2.35). This figure was taken from Roth [14]	29
3.1	The top hat ($S_0(x)$), triangle ($S_1(x)$) and 3 rd order spline ($S_3(x)$) are plotted in 1D.	32
3.2	The “Yee” grid is depicted (left) where the electric and magnetic field components are staggered by half a cell. The fields, currents, position, and velocity make use of the staggered grid by leapfrog time integration (right). This picture was taken from the WarpX documentation [15] (which is another PIC code).	33
3.3	A neural network architecture with labeled weights between the nodes in adjacent layers. This network has 2 inputs, 1 output, and 2 hidden layers (which have 3 or 2 nodes in each).	38
3.4	The neural network architecture used in section 5.3. This network has 4 inputs, 3 outputs, 12 hidden layers, and 64 neurons per hidden layer.	40
4.1	Proton energy spectrum from 1D particle-in-cell simulations depicted for three different temporal delays (including $\Delta t = 0$) from FIG. 3 in Markey et. al. [16].	42
4.2	Schematic of the incident laser on the half-cavity target (left) in Scott et. al. [17]. The radius of the cavity foil determines the delay ($\tau = 2r/c$) between the main pulse and the post-pulse (reflected laser light of $\sim 40\%$ energy of the main pulse).	42
4.3	Geometry of the two pulse scheme as shown in Figure 1 of Ferri et. al. (2019) [18]. The single pulse has a total energy of 1.1J at an incidence angle of $\phi = 45^\circ$ and is shown through several time snapshots (a-c). In (d-f), the double pulse is shown through those same time snapshots with energies of 0.55 J in each pulse (the 1.55 J is a typo from the original figure). Other parameters include $\tau_{\text{fwhm}} = 38 \text{ fs}$, thickness = $3 \mu\text{m}$, material = aluminum, $w_{0,\text{fwhm}} = 5 \mu\text{m}$, $I_0 = 7 \times 10^{19} \text{ W cm}^{-2}$	43

4.4	Double pulse effectiveness in terms of changing preplasma scale length (a) and total laser energy (b,c) from Ferri et. al. (2019) [18].	45
4.5	FIG. 2 from Yao et al. [19]. Case 0 shows electron signals from a single pulse. Case 1 shows electron signals from a double pulse with spatial separation 120 μm . Case 2 shows electron signals from a double pulse with no spatial separation.	46
4.6	Target chamber schematic showing the split beam configuration at the Laser-Net Titan experiment conducted in March of 2024. Two independent off-axis paraboloid mirrors focus each beam onto a 15 μm Au target which record proton spectra from multiple electron positron proton spectrometers.	47
4.7	Electric field in the target normal direction at simulation time of 800 fs for the (a) flat single 41 $^\circ$ pulse, (b) expanded single 41 $^\circ$ pulse, (c) flat double pulse, (d) expanded double pulse (on gold 65 J). The hatched gold rectangle is overlaid for a visual of the size of the initial, unperturbed target.	48
4.8	Proton distribution as a function of angle $\phi = \tan^{-1}(p_y, p_x)$ and energy at simulation time of 2100 fs for the (a) flat single 41 $^\circ$ pulse, (b) expanded single 41 $^\circ$ pulse, (c) flat double pulse, (d) expanded double pulse. Only protons with energy greater than 1 MeV are plotted.	49
4.9	Spectrum at 2100 fs for (a) protons and (b) electrons. Particles that have left the simulation before 2100 fs are included in the spectrum from their energy at the time of crossing the boundary.	50
4.10	Conversion efficiency of laser energy into greater than 1 MeV (a) protons and (b) electrons.	51
4.11	Three slices of radio-chromic film stacks that measure proton doses at 2.9, 16.55, and 21.3 MeV for 3 different pulse arrangements. A darker blue color indicates a higher proton dose at a given spatial location. For reference the stacks are 2 \times 2 inch squares that are placed 18.6 cm behind the target. . .	52
4.12	The radio-chromic film total estimated dose for all 50J shots. The blue circles indicate when both beams were used, while the orange + and green x markers indicate when beams 1 and 2 were used, respectively. These results are not calibrated, they are estimated from a calibration in Chris Willis' dissertation. This is why the y axis is estimated in units of Gy/sr. The implementation of sr allows for comparison of different size RCF stacks.	53
5.1	The net charge density (left) as a function of position $x/c_s t$ and normalized electric field E/E_0 (right) for $\omega_{pi} t = 50$ taken from Fig 1 and 2 in Mora's Paper [20]. On the right, the self-similar electric field from Equation 5.9 is plotted with a dashed line.	59
5.2	The electron density profile of the pre-expanded target is depicted for various times t_0 . In this figure, $n(0) \equiv n_{\max}$. Taken from Desai et al. [21] where z was used as the distance along the laser axis instead of x as done in this work.	62

5.3	The dotted black line shows the maximum proton energy predicted by Equation 5.19 with the pump depletion considerations in subsection 5.1.3 assuming $t_0 = 60 \text{ ps}$, $I_0 = 10^{19} \text{ W cm}^{-2}$, $\kappa = 10^{-7}$, $d = 0.5 \mu\text{m}$. The red stars indicate the predicted positions of maximum proton energy $\sim 12 \mu\text{m}$. This plot is overlayed on top of an experimental maximum proton energy distribution from Morrison et. al. [22]. This figure is taken from Desai et. al. [21].	63
5.4	MAPE versus number of training points from ML model predictions for (a) max proton energy, (b) total proton energy, (c) average proton energy and noisy testing data. Each panel shows results from (solid) 0%, (dashed) 15% and (dotted) 30% added noise in the data. Black lines with different line types indicate the MAPE between the noisy and noiseless data. Because we only compare ML models to noisy data in this figure, these black lines indicate the best that any ML model could conceivably do. Figure and caption taken from Figure 3 of Desai et al. [23].	66
5.5	Solid lines show the typical MAPE in (a) maximum proton energy, (b) total proton energy, and (c) average proton energy when the models (which were trained on 2000 synthetic data points with noise) are evaluated on data with different levels of noise. Dashed lines show the typical error when those same ML models are evaluated on noiseless test data. Black solid lines indicate the MAPE between the noisy and noiseless data. Figure and caption taken from Figure 4 of Desai et al. [23].	67
5.6	The execution time of the different ML models averaged across noise levels in computing the maximum, total, and average proton energies. Figure and caption taken from Figure 5 of Desai et al. [23].	68
5.7	Parameters that produce maximum proton energy cutoffs in three different desired ranges: 1.0 MeV, 0.5 MeV and 0.25 MeV. Combinations of thickness and focal distance that produce these energy cutoffs (irrespective of the laser to proton conversion efficiency) are shown with dotted red lines. With each red line we also show with dotted gray lines the thicknesses and focal distances that produce proton energy cutoffs that are +15% or -15% of the cutoff goal. Green shaded areas show regions where the laser to proton conversion efficiency is high (i.e. within 5% of the optimal value). A green star shows the ideal conditions for maximizing the proton conversion efficiency. The blue region corresponds to using all the terms in Equation 5.31 and the blue star indicates the ideal conditions according to that minimization scheme. Figure and caption taken from Figure 6 of Desai et al. [23].	69
5.8	Parameters that produce maximum proton energy cutoffs according to three trained ML Models on 2,000 data points with 30% added noise: (a) GPR, (b) SVR, (c) NN compared against the red and gray lines plotted in Figure 5.7. The green and blue shaded regions are scatter plots of a subset of evaluated points that fall within 5% of the model's predicted optimum according to the same criteria in Figure 5.7. Figure and caption taken from Figure 7 of Desai et al. [23].	70

5.9	Model training results using data with 10% added noise. Testing MAPE (a) is plotted for the three ML models against the number of training points and averaged between results for maximum, average, and total proton energy. The training time (b) of the ML models in minutes is plotted on a logarithmic scale. The vertical bars are standard deviations computed from running the training splits 3 times with different seeds to control the data splitting and random parameter initialization of the NN and SVGP models.	73
5.10	Testing MAPE is plotted against different levels of gaussian noise using the full training dataset for the three models with the three output energy results averaged.	74
5.11	Colormaps in the 2D parameter space of target thickness and target focal position that display (left panel) the maximum proton energy (i.e. energy cutoff KE_c) and (right panel) laser to proton energy conversion efficiency η_p as calculated from the modified Fuchs et al model. These plots were generated assuming 14.14 mJ of laser energy and a pre-pulse contrast of 10^{-7} . 75	
5.12	Colormaps that show estimates of Equation 5.32 assuming $KE_{c,\text{goal}} = 1 \text{ MeV}$ for the three ML models (NN, POLY and SVGP) and the modified Fuchs et al. model dataset with no added noise (FUCHS). The modified Fuchs et al. model with 30% added noise was used to produce the training data for the ML models. For each β value (i.e. each column), the same color levels are used in order to facilitate comparison between the models. A cyan colored star is placed at the location where each ML model predicts a minimum value for Equation 5.32 which can be compared to the analytic model prediction indicated by a white star.	76
5.13	Synthetic data was generated in one of two “campaigns”. In (a) campaign 1, the target focus and thickness is varied in discrete steps and each blue dot varies the laser energy from minimum to maximum. In (b) campaign 2, the depicted intensity and contrast looping is performed for discrete steps in target thickness from $0.5 \mu\text{m}$ to $5\mu\text{m}$	78
5.14	Testing set MAPE evaluated on several ML models trained on data combined from two separate campaigns shown in Figure 5.13. The dashed line differs from the solid blue line in the polynomial degree.	79
6.1	A schematic of the experimental chamber, targetry system, diagnostics, and laser pulses entering the chamber at a kHz repetition rate. Figure taken from a manuscript in review by Tamminga et al.	83
6.2	(A) Microscope Shadowgraphy image of the central region of the liquid sheet target in vacuum. (B) Spatially dependent thickness map across the liquid sheet, collected with a Filmetrics white-light interference profiler. The white cross indicates the location of the minimum sheet thickness at 450 nm. For scale, the width of the sheet in (B) is $560 \mu\text{m}$. Figure reprinted from Figure 5 of George et al. [24].	84
6.3	The pixel number to proton or electron kinetic energy mapping for the two CCDs present in the magnetic spectrometer. This is the same mapping that was used in Morrison et al. [22].	86

6.4	(a) An example of the voltage trace each individual shot registers on the laser diode. (b) The peak of the voltage trace is plotted for a range of shots.	86
6.5	Linear relation from voltage to energy for both the main pulse (blue) and pre-pulse (red). The slope and intercept are displayed on the graphs.	87
6.6	(A) A list of instruction on how to use the GUI and a button that loads in data already saved to a compressed HDF5 file. (B) A panel that shows two variables plotted against each other. (C) The mapping between cosine-squared of the waveplate angle and the measured voltage on the laser diodes. (D) Two variables are plotted as a function of time and shot number. (E) Instructions for the optimization task with options to choose a machine learning model, desired inputs, and displayed error metrics after training the model. (F) A visual of the optimization task which shows darker purple colors in regions of the parameter space that best optimize the chosen metric from Equation 6.1.	89
6.7	(A) A list of instructions on how to load in the data. (B) A heatmap that shows the pixel counts for the shot numbers throughout the run. (C) A diagnostic that shows where (if any) shots are erroneously being missed due the lab equipment. (D) An electron spectrum plotted for a specified shot. (E) An electron spectrum binned by energy in MeV on a log scale.	90
6.8	Electron spectra plotted for various levels of β for a specified cutoff energy $KE_{c,\text{goal}} = 0.7$ MeV. The different spectra are predicted optimal parameters from a random forest model trained on data collected in an earlier run.	92
A.1	The total energy and how it is distributed over time in the simulation. The black line is amount of energy that should be in the system from the laser pulse in the simulation.	110
A.2	A spearman correlation matrix of the inputs and outputs of all the simulations	111
A.3	Plot of Arber et al. model (Equation A.9) compared to the effective particle per cell model (using Equation A.10) plotted against the electron particles per cell.	113

List of Tables

Table	Page
4.1 Summary of Titan Simulations that varied the number of pulses, incidence angle (θ_i), intensity at peak focus (I_0), total laser energy (E_{laser}), and pre-plasma scale length (L_p). The maximum kinetic energy KE_{max} and conversion efficiency η are shown for both electrons (e) and protons (p). The top half of the table includes simulations with $E_{\text{laser}} = 65$ J which are used in the figures in this section. The bottom half of the table includes simulations with (otherwise identical) lower laser energy.	51
5.1 Optimal hyperparameters found through grid searches and cross-validation using only the training set for the results in section 5.2.	65
5.2 Optimal hyper-parameters including the root mean square error (RMSE) and mean fit time, determined from a grid search of hyperparameters for the NN, POLY, and SVGP. For the NN, the batch size (BS), learning rate decay (γ), patience (P), learning rate (LR), and architectures (layers x neurons per layer) were changed throughout the scans. For the POLY, the regularization parameter (α) and degree (deg) were varied. For the SVGP, the number of inducing points (IP), latent functions (LF), and learning rate (LR) were changed throughout the scans.	72
5.3 Comparison metrics evaluated from Figure 5.12. The RMSE row shows the root mean squared error between the colormap values of the ML models and the analytic model for each value of β . The Δ_{opt} row calculates the Euclidean distance between the predicted optimum and true optimum (i.e. distance in μm between the cyan and white stars in Figure 5.12).	77
6.1 A description of the experimental parameters, the range they were scanned through, and the period of the parameter scan. This table was reproduced from forthcoming work in Tamminga et al. (2025).	91
A.1 Summary of Simulation Parameters (constant)	110
A.2 Particles per cell and conversion efficiencies for all 44 simulations.	112
A.3 Effective ion charge for all simulations	114

ACRONYMS

- AFIT** Air Force Institute of Technology. [64](#)
- ALLS** Advanced Laser Light Source. [9](#)
- BO** bayesian optimization. [38](#), [55](#), [81](#)
- CCD** charge coupled device. [84](#), [85](#), [87](#), [88](#), [91](#), [92](#)
- CPA** chirped pulse amplification. [3](#), [25](#)
- CSU** Colarado State University. [81](#)
- CSUCI** California State University - Channel Islands. [64](#), [82](#)
- DAQ** data acquisition system. [82](#)
- EDX** energy dispersive x-ray fluorescence. [9](#), [10](#)
- EPICS** Experimental Physics and Industrial Control System. [88](#), [91](#), [92](#)
- EPPS** Electron Positron Proton Spectrometer. [47](#)
- eTNSA** enhanced target normal sheath acceleration. [27](#), [41](#), [43–45](#), [81](#)
- FWHM** full width at half maximum. [13](#), [82](#)
- GPR** gaussian process regression. [38](#), [64](#), [65](#), [70](#), [71](#)
- GPU** graphics processing unit. [65](#), [71](#), [92](#)
- GUI** graphical user interface. [89](#), [90](#)
- HDF5** Hierarchical Data Format 5. [85](#), [87](#), [88](#), [90](#)
- HEDS** high energy density science. [2](#), [55](#)
- HHG** high-harmonic generation. [22](#)
- IBA** ion beam analysis. [9](#)

- IMPT** intensity modulated proton therapy. 6
- JLF** Jupiter Laser Facility. 41
- LANL** Los Alamos National Laboratory. 9
- LLE** Laboratory for Laser Energetics. 9
- LLNL** Lawrence Livermore National Laboratory. 26, 41
- LSP** Large Scale Plasma: An implicit particle-in-cell code. 33
- LWFA** laser wakefield acceleration. 28
- MAPE** mean absolute percentage error. 36, 65, 71, 72, 78
- ML** machine learning. 34–37, 55, 56, 64, 65, 68, 72, 74, 75, 77, 78, 81, 90, 92, 93
- MSE** mean squared error. 36, 37, 39, 115
- NGP** nearest grid point. 31
- NIF** National Ignition Facility. 4, 9
- NIF-ARC** National Ignition Facility - Advanced Radiographic Capability. 7, 9
- NN** neural network model. 38, 39, 55, 64, 65, 70–72, 75, 78, 92, 93
- OAP** off-axis paraboloid mirror. 47, 82
- OMEGA-EP** OMEGA Extended Performance System. 9
- OSC** Ohio Supercomputer Center. 65
- OSUCCC** The Ohio State Comprehensive Cancer Center. 6, 7
- PIC** particle-in-cell. 30, 32, 41, 43, 45, 47, 55, 107, 115
- POLY** polynomial regression. 71, 72, 75
- PPC** particles per cell. 48
- RAL** Rutherford Appleton Laboratory. 25, 45, 81
- RBФ** radial basis function. 37, 65
- RCF** radio-chromic film. 52, 53
- ReLU** Rectified Linear Unit. 38
- RF** radio frequency. 9
- RMSE** root mean squared error. 75

- RPA** radiation pressure acceleration. 28
- SOBP** spread-out Bragg peak. 6
- SRIM** stopping range of ions in matter. 6
- SVGP** stochastic variational gaussian process. 71, 72, 75, 78
- SVR** support vector regression. 37, 64, 65, 70, 71
- TNSA** target normal sheath acceleration. 5, 9–11, 24–28, 41, 43, 45, 48, 61, 81, 93, 107
- WP-ELL** Extreme Light Laboratory at the Wright-Patterson Air Force Base. 55, 56, 64, 70, 81, 82, 91, 109
- XPIF** x-ray and particle-induced fluorescence. 9

Chapter 1

INTRODUCTION

This chapter introduces ultra-intense lasers, gives applications of laser-accelerated protons, and presents an outline of the topics in this work.

1.1 Lasers

The word laser should actually be written as “LASER” because it is an acronym: light amplification by stimulated emission of radiation. Stimulated emission refers to Albert Einstein’s idea that photons (particles of light) could “stimulate” atoms to produce identical photons [25]. These identical photons form a coherent light source which possess the same quantum-mechanical phase and wavelength. It wasn’t until 1954 that Charles Townes and Arthur Schawlow first explored using stimulated emission to generate electromagnetic radiation¹ with a device called the maser (because it produced *microwave* wavelength light). Today, these devices are more often called lasers because they produce *light* in other wavelengths (like visible and infrared).

A typical laser operates by adding energy to some material from a strong flash of light called the pump source. This material is called the active lasing medium. The atoms in the medium absorb light which excites electrons to higher energy states. Over time, these electrons relax back into lower energy states, emitting photons that collide with excited atoms to stimulate emission of more photons. The medium is situated in an optical cavity (or resonator) which is composed of two reflecting mirrors that bounce these photons back and forth many times. With each reflection, photons pass back through the lasing medium, gaining more photon energy through stimulated emission in the process. As a result, the active lasing medium is sometimes called the gain medium. Since one of the reflectors is

¹Electromagnetic radiation is just another word for light and is made up of oscillating electric and magnetic fields. The distance between adjacent wave crests in the fields is called the wavelength. Visible light has a wavelength between 400 and 700 nanometers and other forms of light (invisible to the naked eye) are similarly classified according to their wavelengths: radio, microwave, infra-red, ultra-violet, x-ray, gamma.

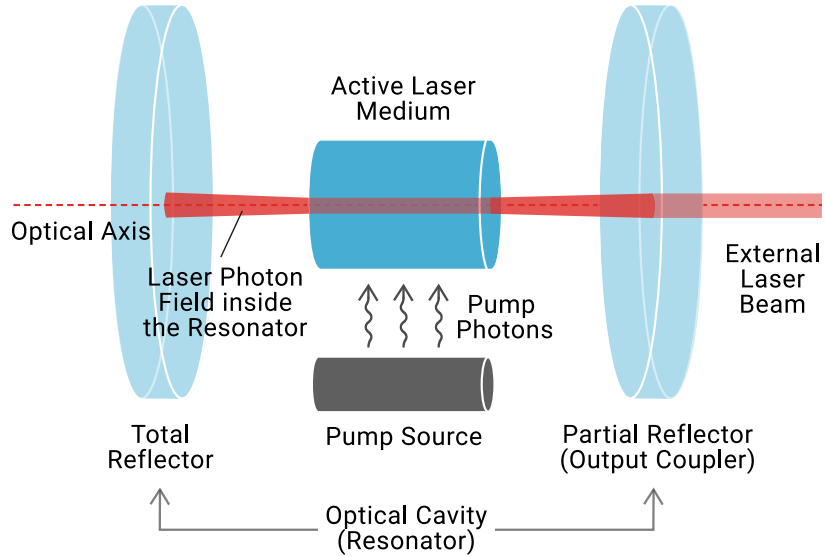


Figure 1.1: The components of a laser are depicted which include the pump source, active laser medium, and optical cavity. Image source: [1].

only partially reflective, some of this laser light will pass through to become an external laser beam. This process is visualized in Figure 1.1.

Lasers are best known for their ability to produce focused, high intensity light at a particular wavelength. Low powered lasers can be used as a laser pointer for a presentation, while higher powered lasers can cut solids in half. From both fundamental physics and industry perspectives, scientists are interested in increasing the intensity of lasers to explore various [high energy density science \(HEDS\)](#) phenomena. The most basic definition of intensity is

$$\text{Intensity} = \frac{\text{Energy}}{\text{Area} \times \text{Time}} \quad (1.1)$$

So, for a given laser pulse, increasing the intensity would involve increasing the energy, decreasing the area (in terms of the surface that the laser beam hits), or decreasing the time. The energy can easily be increased by letting the laser stimulate emission of photons in the optical cavity with more passes. However, when the intensity in the cavity becomes too large, damage to the optical components (like the gain medium) can occur. In 1985, this problem was resolved by Donna Strickland and Gerard Mourou [26] by first stretching an initial pulse in time before reaching the amplification stage in the gain medium. A stretched pulse can continue to gain energy while being sufficiently spread out (less intense) to not damage optical components. After amplification, the pulse is then compressed back into a

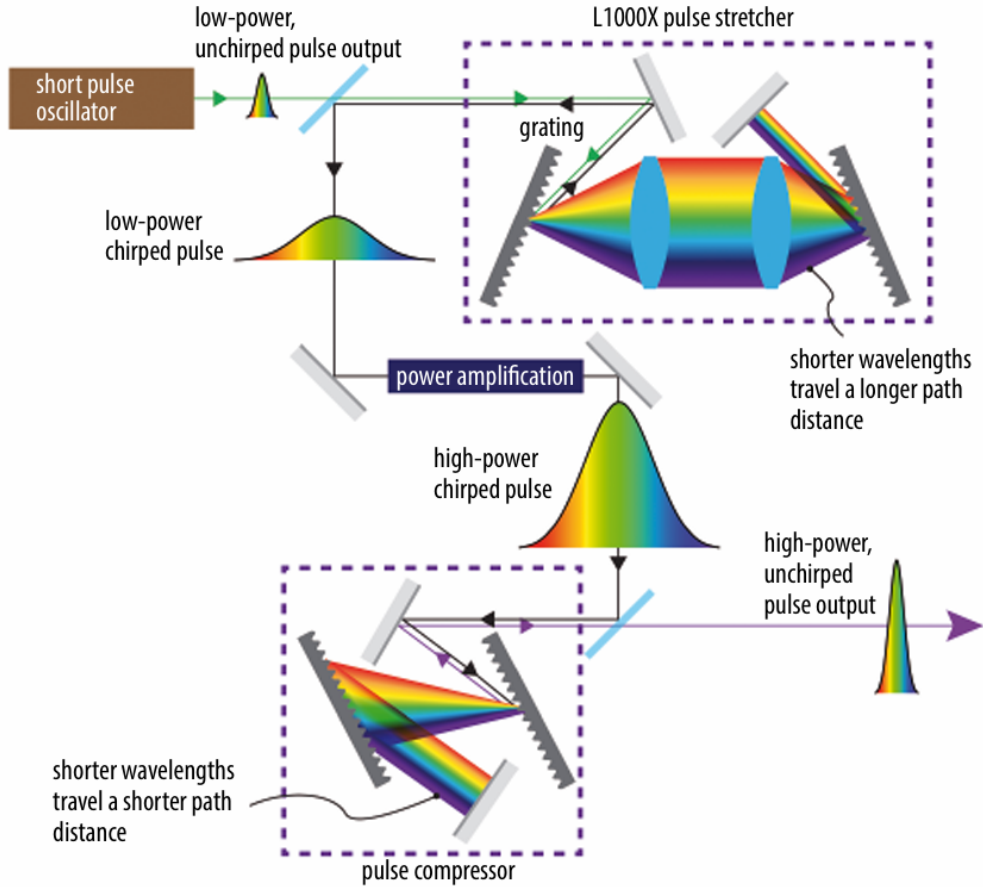


Figure 1.2: The stretch, amplification, and compression stages of chirped pulse amplification are depicted. Taken from [2].

shorter pulse. The clever use of gratings that separate light of different wavelengths allows pulses to easily be stretched and compressed in time. This method called **chirped pulse amplification (CPA)**, is visualized in Figure 1.2 and resulted in a nobel prize [27].

The **CPA** technology enabled lasers to produce high energy, extremely short femtosecond (a billionth of a millionth of a second) long pulses that drove intensities into the relativistic regime where electrons can be accelerated to (nearly) the speed of light. The history of laser intensity since the production of the first laser in 1960 is depicted in Figure 1.3. The graph shows that between 1970-1985, laser intensities did not increase very much, but the invention of **CPA** allowed intensities to increase 2-3 orders of magnitude every decade. The most intense lasers today are capable of accelerating protons near the speed of light in the so-called ultra-relativistic regime. If the intensities of lasers continue to increase in the coming decades, physics at the most fundamental level could be explored by analyzing what is going on inside the nucleus of an atom. These intensities would provide insights into the

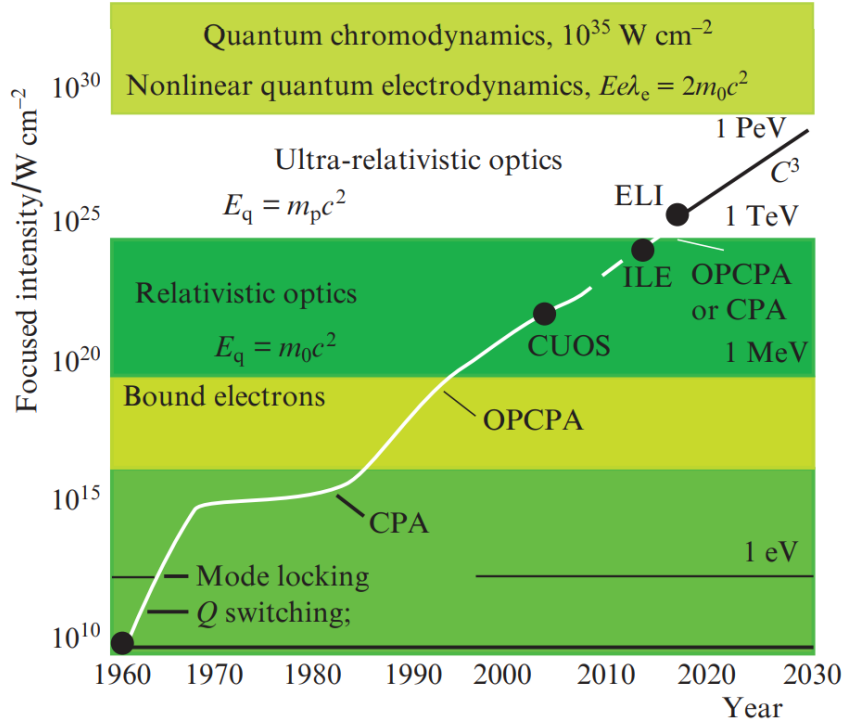


Figure 1.3: History of focused laser intensities from the inception of the laser in 1960. The graph is labeled with intensity regimes, technological milestones, and acronyms of laser facilities. Taken from Figure 4 in Yakovlev [3].

fields of quantum electrodynamics and quantum chromodynamics.

In this work, the lasers mentioned employ a titanium sapphire gain medium which is produced by doping (adding impurity) titanium ions in a sapphire² crystal. These typically output micron wavelength (infra-red) laser beams and are very commonly used in laser facilities across the globe.

1.2 Applications

The lasers described in the preceding section are used to study materials at high energy density scales. These laser-matter interactions are important for a variety of reasons. First, lasers can heat up materials to be as hot and dense as the core of the sun (if only for a tiny fraction of a second) which can provide astrophysical insights. Second, these hot, dense conditions are needed for nuclear fusion which is an extremely promising future source of clean energy (explored at places like the [National Ignition Facility \(NIF\)](#)). Finally, laser-matter

²Corundums are a mineral composed of aluminum oxide (Al_2O_3) with trace amounts of impurities that replace a small fraction of the aluminum ions. Blue sapphires have trace amounts of titanium and iron, while rubies have trace amounts of chromium.

interactions can produce high energy, pulsed beams of protons, electrons, and ions. The most well-studied proton acceleration mechanism is called [target normal sheath acceleration \(TNSA\)](#) whose physical origins will be explored more in [section 2.4](#).

During the course of my PhD, I have worked on ways to optimize the [TNSA](#) mechanism for accelerating protons and this section highlights some its most important applications: (1) proton therapy for cancer treatment, (2) proton radiography for imaging, and (3) ion beam analysis for materials characterization.

1.2.1 Proton Therapy

Finding a cure for cancer is one of the largest medical challenges faced worldwide and cancer generally requires the use of harsh treatments like invasive surgery, chemotherapy, and immunotherapy. Another relevant treatment is called radiotherapy and more than half of all people with cancer will receive it as a part of their medical care [28]. Typically, a large machine will provide a source of x-rays (a type of energetic ionizing radiation) that kills the tumor. However, this radiation does not discern whether the cells are cancerous or not – healthy tissue along the radiation beam path surrounding the tumor will also be damaged. This damage can be mitigated by shooting many beams from different angles such that they overlap at the site of the tumor. In this way, the dose delivered in the beam overlap region will be significantly higher than the surrounding tissue. This approach is typically employed by situating the machine on a rotating “gantry”

As early as 1905, Bragg [29] identified that charged particles have different properties than x-rays when passing through matter. Specifically, he identified that radium particles lost more energy (i.e. delivered a higher dose) at a lower speed. Physically, the slower the radium particles, the more time it has to interact with each of the individual atoms and the more energy it can deposit. This means that when the radium first enters a material at its highest speed, it is losing energy slowly. In contrast, when the radium is at a slow speed and about to stop, it is losing energy very quickly. In 1946, Wilson [30] identified that this property of charged particles enables the deliver of a concentrated dose close to a tumor site. In [Figure 1.4](#), these differences are explicitly highlighted between x-rays and proton beams traveling through water. It can be seen that the proton beam is sharply peaked at a particular distance of around 24 centimeters, where the x-ray beam delivers a higher dose just a few centimeters in. One can see the advantage of protons quite readily from this picture – if a tumor is located 24 centimeters into the body, the protons, comparatively to the x-rays, will deliver more energy at the tumor site and less energy to the surrounding tissue. The shape of the proton beam curve in this graph is appropriately referred to as a “Bragg Curve” which peaks at the “Bragg Peak”.

The specifics of the depth-dose curve depend on the material that the particles are traveling through as well as initial energy of the protons. These conditions are well-studied

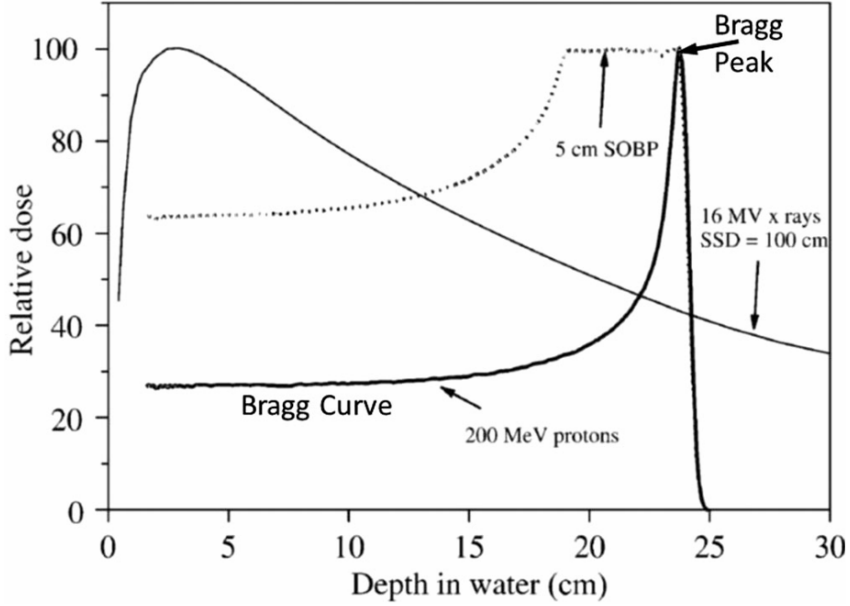


Figure 1.4: The dose delivered as a function of depth traveled in water for two types of beams are depicted – 200 MeV protons and 16 MV x-rays. Taken from Figure 1 in Mohan [4].

by empirical measurements of the [stopping range of ions in matter \(SRIM\)](#) [31] and can be combined with other techniques to achieve a depth-dose curve that not only peaks at different depths, but also has a [spread-out Bragg peak \(SOBP\)](#) that expands the region where the highest dose is delivered. The most modern form of proton therapy is called [intensity modulated proton therapy \(IMPT\)](#) whose intensities are modulated to optimally balance tumor dose and sparing of normal tissues [4]. The first proton therapy center opened at the Loma Linda University Medical Center in California in 1990, but today there are more than 100 centers around the world (with more in the planning or construction stage) [4].

Here in Columbus, [The Ohio State Comprehensive Cancer Center \(OSUCCC\)](#), in collaboration with Nationwide Children's Hospital, opened a 55,000 square foot proton therapy center in December of 2023 [32] that uses [IMPT](#). Despite all the aforementioned benefits of proton therapy, the initial cost is tremendous – [OSUCCC](#) was a 100 million dollar investment. The significant cost demonstrates the value this could bring to Central Ohio. The facility is even outfitted with the capability to perform [FLASH](#) therapy which is a newer, experimental form of proton therapy. Compared to conventional methods, [FLASH](#) uses much higher dose-rates (i.e. amount of dose per second) with much shorter exposure times (seconds) for the same total dose. The higher dose-rates have been shown to reduce

radiation-induced toxicity in healthy tissues in pre-clinical trials [33] and is currently under clinical trials [32].

The conventional cyclotron accelerators used at OSUCCC are extremely large and expensive which limits their availability to select locations globally. In recent years, it has been proposed that laser-based particle accelerators could be used to generate high energy protons. Just like FLASH therapy, laser-based sources are capable of delivering high dose-rates in extremely short exposure times. Also, laser facilities could in principle be smaller and less costly. On the other hand, the technology is not adequately matured to be considered in the near future [34]. Laser-based sources are typically only able to generate protons in the 10s of MeV reliably (as opposed to the 100s of MeV required for clinical operation), possess orders of magnitude smaller numbers of protons, and poor reproducibility of the laser pulse output. In addition, the conventional accelerators have already made significant strides in terms of reducing cost, increasing beam quality, and reducing size in recent years [34] which is something laser-based sources will need to keep up with in the future. However, the potential of developing a smaller, lower cost, higher dose rate proton accelerator remains an important motivating factor for many laser-plasma physicists in the coming years.

1.2.2 Proton Radiography and Laser Fusion

All of us are familiar with the use of visible light to image things³. Other frequencies of light not visible to the naked eye are used all the time to image things as well. High frequency sources like x-rays are used at the dentist due to their ability to probe matter within your body. Radio waves reflect well off of electrically conductive materials like the metals in vehicles which make them ideal for military applications. In a similar way, particles can be used to image objects by analyzing how they interact. Electron microscopes have been used extensively in the past century to image materials at a much higher resolution than an ordinary visible light microscope. From Figure 1.4, we know that protons interact with matter in a different⁴ way than electromagnetic radiation like x-rays. These differences can be exploited to image things that cannot be done well with other types of radiation [35].

One example of proton radiography using laser-accelerated protons is through the National Ignition Facility - Advanced Radiographic Capability (NIF-ARC). As its name implies, NIF-ARC is typically used as light source to collect radiograph images of laser fusion experiments at NIF. These fusion experiments involve using a high powered lasers to compress a millimeter sized frozen pellet of hydrogen fuel (specifically, heavier isotopes of hydrogen called deuterium and tritium) to such high temperatures and pressures that the atomic nuclei fuse together into helium. The sun is an example of a high temperature and pressure environment that is able to sustain fusion as its vast source of energy, but we must

³Cameras send out a flash of light and the reflected light off an object forms an image on the camera

⁴Protons interact differently because they are charged and have mass unlike electromagnetic radiation

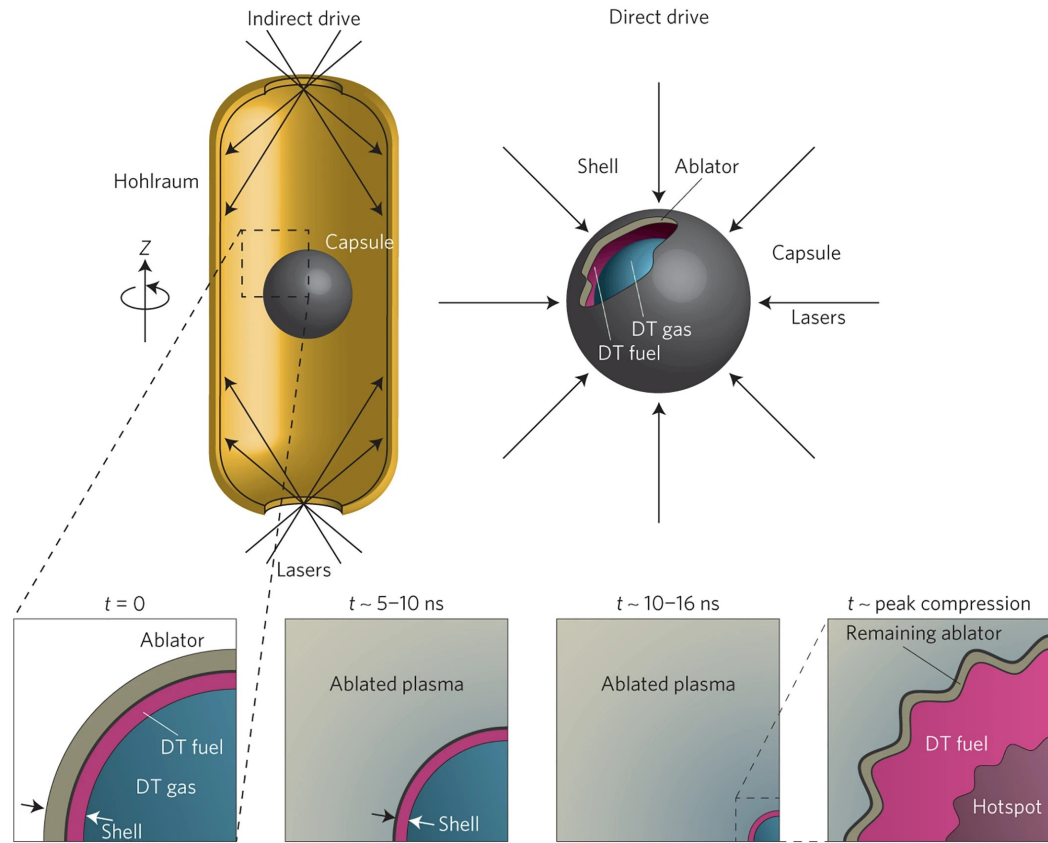


Figure 1.5: Visualization of two different approaches to laser fusion are depicted at the top. Lasers can irradiate the inside of a hollow gold can (called a hohlraum) to indirectly heat a fusion capsule or instead directly heat it. At the bottom, multiple stages of the fusion process are depicted including capsule ablation, compression, and burn. Taken from Figure 1 of Betti et al. [5].

be a little bit more clever on Earth to obtain conditions similar to the core of our sun. A similar capability to NIF-ARC exists at the [Laboratory for Laser Energetics \(LLE\)](#)'s [OMEGA Extended Performance System \(OMEGA-EP\)](#). The [OMEGA-EP](#) provides diagnostics for the main OMEGA laser which performs fusion experiments by directly irradiating a fusion pellet. This is in contrast to the [NIF](#) which indirectly compresses a fusion pellet by first irradiating a gold can that surrounds the pellet. These approaches are aptly called indirect and direct drive fusion and are depicted in [Figure 1.5](#). Proton radiography has been demonstrated successfully at the [NIF](#) through [NIF-ARC](#) [36] and at OMEGA through [OMEGA-EP](#) [37] through [TNSA](#) proton beams produced from laser-irradiated metallic foils.

Conventional sources of protons for radiography purposes are from linear accelerators like the pRad at [Los Alamos National Laboratory \(LANL\)](#). [LANL](#) uses [radio frequency \(RF\)](#) waves of around 200 MHz to accelerate particles up to 800 MeV [38]. The limitation of conventional [RF](#) accelerators is the relatively low frequency. If we take the reciprocal of 200 MHz, we find that the separation between individual waves (the period) is around 5 nanoseconds⁵. If one wanted to take proton radiographs of some experiment happening on a picosecond timescale, the conventional accelerator would not work. On the other hand, lasers typically used for laser-plasma experiments are in the infrared and have wavelengths of around 1 micron. A quick calculation tells us that the period is only around 3 femtoseconds. Since the lasers are pulsed at 3 femtoseconds, the emitted protons would also be pulsed at 3 femtoseconds which would theoretically allow us to capture 1 proton radiograph every 3 femtoseconds. Another advantage of these laser-accelerated proton beams is that they are emitted from a very small spot, on the order of microns, which is beneficial for obtaining a higher quality image [35].

1.2.3 Materials Characterization

While protons can generate images through radiography, they can also more generally tell us information about materials as a whole through a process called [ion beam analysis \(IBA\)](#). [IBA](#) allows scientists to probe material composition and surface structures with MeV ion beams which are appealing partly due to their non-destructive nature (comparatively to sources like x-rays) [39]. [IBA](#) is currently implemented through old Van de Graaf and Tandem accelerator technology, but Passoni [39] argues that [TNSA](#) proton beams can achieve the same result in a more compact, portable, and cheaper setup.

As a proof of principle, Boivin [6] used TNSA beams from the [Advanced Laser Light Source \(ALLS\)](#) laser facility in Canada to determine the elemental mass concentrations of three different metal alloys: stainless steel, bronze, and brass using [x-ray and particle-induced fluorescence \(XPIF\)](#). This is compared to a method called [energy dispersive x-ray](#)

⁵This may seem like a short time, but on the scale of femtosecond and picosecond ultra-intense pulses, this is a thousand or a million times longer!

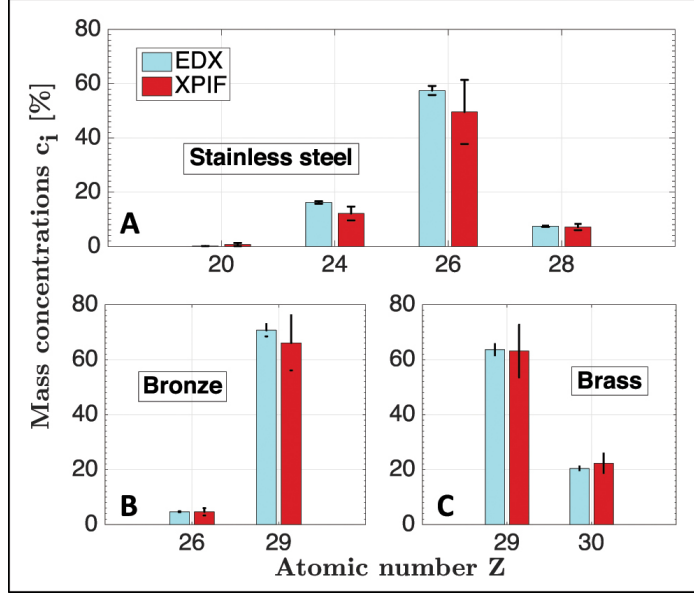


Figure 1.6: Mass concentrations of three metal alloys are shown using two different techniques: Energy Dispersive x-ray Fluorescence (EDX) and X-ray and Particle-Induced Fluorescence. Taken from Figure 4 of Boivin et al. [6].

fluorescence (EDX) used in conjunction a conventional mono-energetic electron beam and shown in Figure 1.6. Although XPIF has larger error bars than EDX, both methods find good agreement with each other.

As a final point, TNSA beams can be accompanied by other radiation sources like electrons, x-rays, and neutrons. Different materials characterization process could, in principle, be used in conjunction with each other. While TNSA beams are not the most common way to characterize materials today, they may emerge as an important tool for their ability to be pulsed at a high repetition rate and generated from a relatively compact system.

1.3 Outline

In the last decade, machine learning has emerged as an increasingly important tool⁶ for understanding the vast volume of data present in this world. Scientists have already been using machine learning in other fields to make new discoveries, but the field of laser-driven proton acceleration has only started to make use of it. This is because machine learning requires an immense amount of data to provide a true benefit [40] and most modern laser systems only produce around one pulse per second (or less). Before my time, our group produced TNSA proton beams in 2018 [22] from a laser system that sends 1000 pulses a second. With this many pulses, collecting large amounts of data now becomes a reality.

⁶This is especially clear from the past few years of generative AI with tools like Chat-GPT.

However, to realize applications, the [TNSA](#) proton beams need to be optimized for specific use cases.

This work is a continuation of prior efforts in the group to computationally study [TNSA](#) proton beams from Gregory Ngirmang, Joseph Smith, Nashad Rahman and others. In [chapter 2](#) and [chapter 3](#), I give the physics and computational background needed to understand the main body of the dissertation. The bulk of my PhD work is summarized in [chapter 5](#) which involved the construction of a synthetic proton acceleration dataset. This data was used as a testbed for assessing the feasibility of applying machine learning to possible future proton acceleration datasets. In [chapter 4](#), I detail the simulations I ran to corroborate the experimental findings of enhanced proton acceleration from the use of a split pulse. A future laser facility could possibly use the split pulse scheme as one of many optimizations to achieve a proton beam with desired properties. In [chapter 6](#), I detail my involvement in programming a machine learning feedback loop to automatically optimize accelerated electrons and protons from collected data. Finally, in [chapter 7](#), I conclude and give suggestions for future work.

Chapter 2

PHYSICS BACKGROUND

At the most basic level, a plasma is a state of matter that largely consists of charged particles (rather than neutral particles). Typically, this is achieved by heating a solid, liquid, or gas so much that the constituent atoms achieve a sufficient level of ionization. Francis Chen, author of a prominent plasma physics textbook [41], describes a plasma as

a *quasineutral* gas of charged and neutral particles which exhibits *collective behavior*

In this chapter, laser fields and the physics of charged particles oscillating in them will be overviewed to better understand the plasmas produced from laser-matter interactions. Plasma properties and their relation to quasineutrality and collective behavior will be discussed. Then, ion-acceleration will be explained in the context of laser-plasma interactions.

2.1 Electric Fields

2.1.1 Gaussian Laser

In order to heat up a material with a laser efficiently, the energy would ideally be concentrated to a small point. Lasers are a coherent source of light that can be focused to narrow beams. The intended output of many lasers is the fundamental transverse electromagnetic mode [42] (TEM_{00}) described by the following electric field

$$E(r, x) = E_0 \hat{y} \frac{w_0}{w(x)} \exp\left(-\frac{r^2}{w(x)^2}\right) \cos\left(kx - \arctan\left(\frac{x}{x_R}\right) + \frac{kr^2}{2R(x)}\right) \quad (2.1)$$

where \hat{x} is the propagation direction, \hat{y} is the polarization direction, and $r = \sqrt{y^2 + z^2}$ is the radial distance away from the laser axis. The radius of curvature $R(x)$ is inversely related to how strongly the wavefronts are curved and is infinity at $x = 0$ and minimum at $x = x_R$. The guoy phase $\arctan(x/x_R)$ is an observed phase of π that is continuously picked up as the beam propagates from $x = -\infty \rightarrow x = +\infty$. Additionally, the beam radius w is expressed as

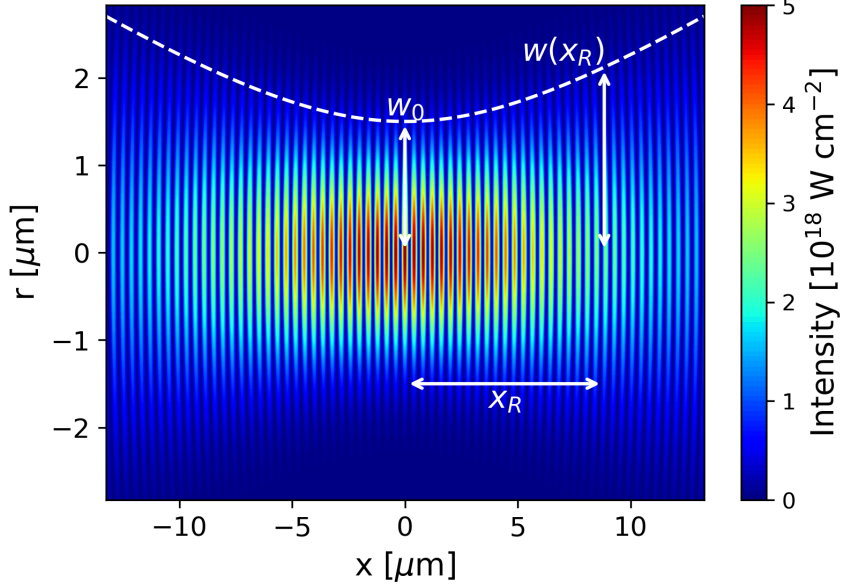


Figure 2.1: The intensity profile of a gaussian beam with laser parameters seen in the Extreme Light Laboratory at Wright-Patterson Air Force Base ($\lambda = 0.8\mu\text{m}$, $I_0 = 5 \times 10^{18} \text{ W cm}^{-2}$, $w_0 = 1.5 \mu\text{m}$, $\tau_{\text{FWHM}} = 40\text{fs}$). The beam radii w_0 and $w(x_R)$ are displayed in addition to the rayleigh range x_R .

$$w(z) = w_0 \sqrt{1 + (x/x_R)^2} \quad (2.2)$$

and has a minimum value at the *beam waist* $w(0) \equiv w_0$ at the focal position of the laser. The length scale over which the beam can propagate without diverging significantly is the *Rayleigh range* $x_R \equiv \frac{\pi w_0^2}{\lambda}$. A beam with these properties is usually referred to as a gaussian beam⁷ and is depicted in Figure 2.1.

The peak intensity is related to the electric field by $I_0 = \frac{1}{2}\epsilon_0 c E_0^2$ and eq. (2.1) shows that the intensity decays as $I(x, r) = I_0(w_0/w(x))^2 \exp(-2r^2/w(x)^2)$ with increasing r and x . If we integrate this intensity distribution over the entire $y - z$ plane (at $x = 0$), we obtain the peak power $P_0 = \frac{\pi w_0^2}{2} I_0$. Furthermore, we can integrate the power over the pulse duration pulse has a $\sin^2(t)$ envelope⁸ to obtain the total energy in the pulse

$$E = \frac{\pi w_0^2}{2} I_0 \tau_{\text{FWHM}} \quad (2.3)$$

⁷I've googled (actually bing'd unfortunately) more times than I can count "gaussian beam wikipedia" over the course of my studies. I don't know why I didn't bookmark that page.

⁸As with most things in physics, when there's an oscillating or pulsed quantity, it typically follows a sinusoidal distribution. The pulse envelope is related to the intensity which is proportional to the square of the electric field. It is possible for the pulse shape to be slightly different (like a gaussian function), but the expressions for energy and pulse **full width at half maximum (FWHM)** do not change significantly.

where τ_{fwhm} is the full-width half-max (half the pulse duration for a $\sin^2(t)$ pulse envelope).

2.1.2 Single Particle Motions

Electrostatics is governed by the Maxwell's equations which describe the allowed wave-like solutions for electric and magnetic fields in both matter and vacuum. The most relevant equation in this section is Gauss' Law or Poisson's Equation which can be expressed as

$$-\nabla^2 \phi = \nabla \cdot \vec{E} \equiv \frac{\rho}{\epsilon_0} \quad (2.4)$$

which relates the electrostatic potential ϕ or electric field E to the charge density ρ . This equation highlights how electric fields are directed radially outward from positive charges and inward towards negative charges. The motion of an electron in the influence of an electric field E or magnetic field B is given by the *Lorentz force* F_L

$$F_L \equiv -e(\vec{E} + \vec{v} \times \vec{B}) \quad (2.5)$$

Quiver Energy

To gain intuition about some quantities of interest for laser-matter interactions, let's consider the simple problem of an electron of charge $-e$ governed by eq. (2.5) with a negligible magnetic field B . Additionally, only consider 1D motion in the oscillating field $E = E_0 \cos(\omega t)$ for a laser field of frequency ω . Then, the equation of motion is

$$\frac{dv}{dt} = -\frac{eE_0}{m} \cos(\omega t) \quad (2.6)$$

We can integrate this equation to obtain the velocity and position as a function of time (assuming $x_0 = v_0 = 0$)

$$v(t) = -v_{\text{osc}} \sin(\omega t) \quad (2.7)$$

$$x(t) = \frac{v_{\text{osc}}}{\omega} [\cos(\omega t) - 1] \quad (2.8)$$

where $v_{\text{osc}} \equiv (eE_0)/(m\omega)$ is defined as the *quiver velocity*. From Equation 2.7, we can calculate the kinetic energy gained by an electron as $U_p \equiv \frac{1}{2}m\langle v^2 \rangle = \frac{1}{4}mv_{\text{osc}}^2$ which is known as the *ponderomotive potential (energy)*. This energy represents the cycle-averaged quiver energy of an electron in an electromagnetic field. A more commonly used term is the dimensionless *normalized vector potential* a_0 which is closely related to the quiver velocity

$$a_0 \equiv v_{\text{osc}}/c = \frac{eE_0}{m\omega c} \quad (2.9)$$

Ultra-intense laser-matter interactions involve relativistic electrons which are produced when $a_0 \gtrsim 1$. In terms of the field, $a_0 \sim 1$ corresponds to a peak electric field $E_0 = \frac{2\pi mc^2}{e\lambda} \simeq 4 \text{ TV m}^{-1}$ (for a $\lambda \approx 1 \mu\text{m}$ wavelength). For this electric field, the peak intensity is $I_0 = \frac{1}{2}c\epsilon_0 E_0^2 \simeq 2 \times 10^{18} \text{ W cm}^{-2}$ for this electric field. Consequently, the threshold for relativistic interactions is commonly understood as $I_0 \gtrsim 1 \times 10^{18} \text{ W cm}^{-2}$ for typical micron wavelength lasers.

Ponderomotive Force

The above approach yields some important scales for laser-matter interactions, but only describes the interaction of a plane wave that is spatially homogeneous. A real laser field would be spatially inhomogeneous and we can express $E(x) \approx E_0 + xE'_0(x)$ to first order. This modifies the equation of motion as

$$\frac{dv}{dt} = -\frac{eE_0}{m} \cos(\omega t) - \frac{eE'_0}{m} \cos(\omega t) \left[\frac{v_{\text{osc}}}{\omega} (\cos(\omega t) - 1) \right] \quad (2.10)$$

where we've inserted the expression for x from eq. (2.8) which should be approximately true for small x . This equation can be simplified and separated into oscillating and non-oscillating components as

$$\frac{dv}{dt} = -\frac{eE_0}{m} \left[\cos(\omega t) \left(1 - \frac{E'_0 v_{\text{osc}}}{e_0 \omega} \right) + \frac{E'_0 v_{\text{osc}}}{2\omega E_0} \cos(2\omega t) \right] - \frac{eE'_0 v_{\text{osc}}}{2m\omega} \quad (2.11)$$

Over many cycles, the oscillating components will average out to zero and the remaining term is given by $\langle F_p \rangle = m \frac{dv}{dt} = -\frac{eE'_0 v_{\text{osc}}}{2m\omega}$ and is called the *ponderomotive force*. We can generalize this to 3D and express this time-averaged force in several different, equivalent ways

$$\langle F_p \rangle = -\frac{e^2}{2m\omega^2} |E_0| \nabla E_0 = -\frac{mc^2}{4} \nabla (a_0^2) = -\nabla U_p \quad (2.12)$$

where

$$U_p = \frac{e^2 E_0^2}{4m\omega^2} = \frac{1}{4} m v_{\text{osc}}^2 \quad (2.13)$$

is the ponderomotive potential energy introduced earlier. The ponderomotive force is an important mechanism in the absorption of laser energy by electrons which will be expanded upon in section 2.3.

2.2 Plasma Physics

The quasi-neutrality condition reflects the fact that a plasma is charge neutral throughout its volume in a similar way to an ideal conductor: mobile electrons will reorganize themselves in the presence of an external electric field to maintain zero field (or constant potential). The

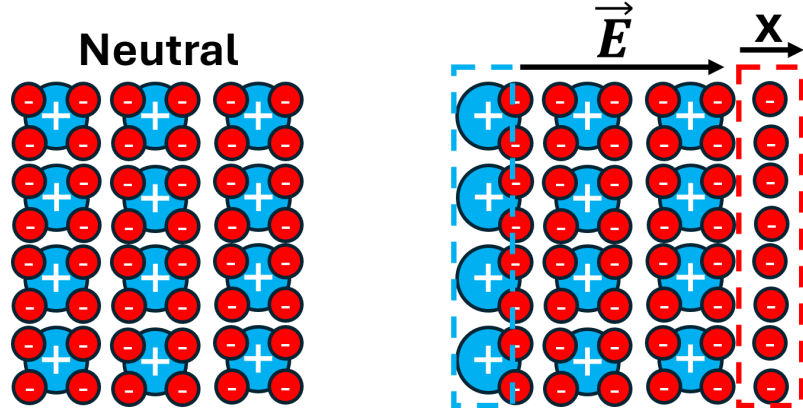


Figure 2.2: An initially charge-neutral plasma is depicted on the left. On the right, the electrons are displaced by a distance x creating a charge separation and electric field akin to a parallel-plate capacitor directed towards the right. Adapted from Smith [7].

simplest plasma description will assume the ions are immobile (due to being much heavier than the electrons) and can be treated as a constant neutralizing background density n_i for the electrons of density $n_{e,0} = Zn_i$ (for a plasma with atomic number Z).

2.2.1 Plasma Electron Oscillations

A simple example can be illustrated by fig. 2.2 which shows a sheet of negative charge density $-\sigma = -en_ex$ displaced to the right a small distance x . The region in the bulk of the plasma will experience a force from the parallel plate “capacitor” fields directed to the left.

$$F = m \frac{d^2x}{dt^2} = -e \frac{en_ex}{\epsilon_0} \quad (2.14)$$

which has the form of a restoring force that brings the charge imbalance back to the center of the plasma. This oscillatory motion has an associated frequency

$$\omega_{p,e} = \sqrt{\frac{n_e e^2}{m_e \epsilon_0}} \quad (2.15)$$

that gives the timescale for electron motion in the plasma. This characteristic frequency shows why plasmas support collective motion (in opposition to a neutral gas in which collisions between individual particles only happen). To get a feeling for this timescale, let’s assume a somewhat typical electron density $1 \times 10^{29} \text{ m}^{-3}$ in laser-plasma interactions to yield a timescale of $\omega_{p,e}^{-1} \simeq 0.1 \text{ fs}$.

Naturally (without externally imposed forces), these fluctuations in charge would be

caused by thermal motions of electrons with a characteristic speed v_{th}

$$v_{th} = \sqrt{\frac{k_B T_e}{m}} \quad (2.16)$$

Due to the strong restoring force from the charge separation, the electrons can only move a short distance λ_D , called the Debye length, out of equilibrium in this timescale. We can estimate this length by equating $v_{th} = \lambda_D/t \simeq \lambda_D \omega_{p,e}$ and solve for λ_D .

$$\lambda_D = \frac{v_{th}}{\omega_{p,e}} = \sqrt{\frac{\epsilon_0 k_B T_e}{n_e e^2}} \quad (2.17)$$

Physically, λ_D gives a length scale over which the electrostatic force persists in a plasma. Within a distance λ_D from some perturbation, charges will feel a force, and outside this distance, the charges will be completely shielded like that of an ideal conductor.

2.2.2 Fluid Model

This description of a plasma as a sea of electrons with collective motion that allows wave-like motions naturally lends itself toward a fluid model. The first component of this model stems from eq. (2.5) whose explicit time and space dependence can be expressed through

$$\frac{dp}{dt} = m\left(\frac{\partial v}{\partial x} \frac{\partial x}{\partial t} + \frac{\partial v}{\partial t}\right) = m\left(\frac{\partial v}{\partial t} + v \frac{\partial v}{\partial x}\right) \quad (2.18)$$

which just considers one spatial dimension for simplicity. The second component of this model is the pressure gradient from thermal motions. Particles will tend to migrate from areas of higher pressure to lower pressure, where the thermal pressure is given by the ideal gas law equation of state $p = n_e k_B T_e$. Consequently, the equation of motion should have a term that is opposite to the pressure gradient direction (i.e. $-\nabla p$). Combining these two components together in a generalized 3D equation results in

$$mn_e\left(\frac{\partial \vec{u}}{\partial t} + (\vec{u} \cdot \nabla)\vec{u}\right) = -en_e(\vec{E} + \vec{u} \times \vec{B}) - \nabla p \quad (2.19)$$

where we've changed the single particle velocity \vec{v} to the fluid velocity \vec{u} and multiplied by the electron density n_e to ensure correct units with the pressure gradient term. Then, let's look for a simple radially symmetric solution where the fluid velocity $u = 0$, magnetic field B is negligible, and the temperature is constant (isothermal).

$$n_e e E = -k_B T_e \frac{\partial n_e}{\partial r} \quad (2.20)$$

and by relating the electric field to the potential $E = -\frac{dV}{dx}$, this equation can be integrated from $n_{e,0} \rightarrow n_e$ and $0 \rightarrow \phi$ to obtain

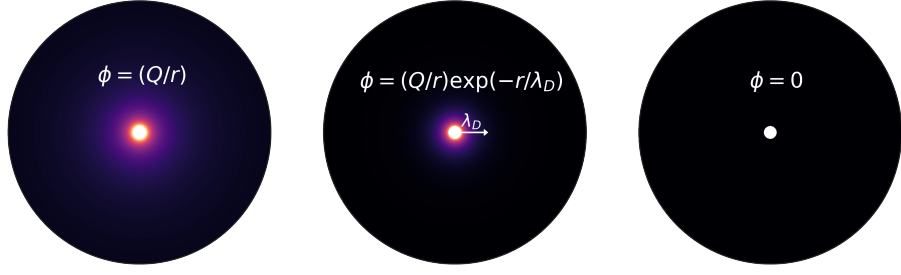


Figure 2.3: Visualization of the electric potential as a function of radial distance away from a positive point charge at the origin in three scenarios: vacuum (left), plasma (center), ideal conductor (right). Brighter colors show a higher value of ϕ . In the center panel, the Debye length λ_D is shown.

$$n_e = n_{e,0} \exp\left(\frac{e\phi}{k_B T_e}\right) \quad (2.21)$$

which is referred to as the *Boltzmann relation* for electrons [41]. We can get an approximate solution to this equation when the potential ϕ is only slightly larger than the equilibrium $\phi = 0$, which can be found when $e\phi \ll k_B T_e$. We can Taylor expand the density to obtain

$$n_e \approx n_{e,0} \left(1 + \frac{e\phi}{k_B T_e}\right) \quad (2.22)$$

and if we assume a fully ionized plasma with immobile ions of charge Z , the density of ions satisfies $n_{e,0} = Zn_i$ and eq. (2.4) becomes

$$\epsilon_0 \nabla^2 \phi = -en_{e,0} + en_e = en_{e,0} \left[1 + \frac{e\phi}{k_B T_e} - 1\right] = \frac{e^2 n_{e,0} \phi}{k_B T_e} \quad (2.23)$$

This equation admits solutions of an exponentially decaying potential

$$\phi(r) = \frac{Q}{r} \exp\left(-\frac{r}{\lambda_D}\right) \quad (2.24)$$

where $\lambda_D = \sqrt{\frac{\epsilon_0 k_B T_e}{n_{e,0} e^2}}$ is the Debye length from eq. (2.17). A visualization of the decaying potential from eq. (2.24) is shown in fig. 2.3. Looking at the center panel, we can see the potential drop off much more quickly than the left panel's potential. The exponentially decaying potential is a feature of plasmas and highlights the ability of plasma electrons to shield fields in a distance λ_D .

2.2.3 Plasma Conditions

Putting all this together, we can define several conditions that are characteristic of plasmas [41]. Quasi-neutrality means that the bulk of the plasma is overall charge neutral, with non-neutral regions generally falling within λ_D of some charge imbalance. Notable exceptions to quasi-neutrality are charged particle beams in ultraintense laser experiments which typically exist on a timescale shorter than the time it takes for the coulomb repulsion to blow the plasma apart. If L is the length scale of the system in which the plasma resides, we require that $\lambda_D \ll L$. However, this condition is not sufficient because an ideal conductor has $\lambda_D = 0$ but is not a plasma due to the absence of collective behavior. Collective behavior can be accounted for by requiring enough electrons N_D within a spherical volume of radius λ_D . The corresponding equation is $N_D = n_e(\frac{4}{3}\pi\lambda_D^3) \gg 1$. The final condition is that electrostatic interactions should dominate over collisions because the collective behavior (e.g. plasma oscillations) originates from the electrostatic forces. This means that the period of oscillations ($\omega_{p,e}^{-1}$) should be less than the mean time between collisions.

2.3 Absorption of Energy

In order for a laser to couple energy to the plasma electrons, some absorption mechanism needs to take place. The most obvious way that electrons can gain energy is through collisions with other energetic electrons and ions. However, the collision frequency is known to get smaller as the temperature goes up [12], so much so that plasmas can usually be treated as collisionless for ultra-intense laser experiments. Below, some of the most common known absorption (heating) mechanisms are summarized.

2.3.1 Critical Density

First, we will look at how the electric field from an oscillating electric field penetrates a plasma. Using eqs. (3.2) and (3.4) combined with the vector identity $\nabla \times (\nabla \times \vec{E}) = \nabla(\nabla \cdot \vec{E}) - \nabla^2 \vec{E}$ [42], we can solve for the vector wave equation in terms of only \vec{E} .

$$(\nabla^2 - \frac{1}{c^2} \frac{\partial^2}{\partial t^2}) \vec{E} = \mu_0 \frac{\partial J}{\partial t} + \nabla(\nabla \cdot \vec{E}) \quad (2.25)$$

We can look for solutions of $\vec{E} = E(x) \cos(\omega t) \hat{x}$ that vary spatially only in the x direction. We assume $E(0)$ is the amplitude of the electric field at the boundary between vacuum $x < 0$ and matter $x > 0$ and wish to understand the form of $E(x)$ when $x > 0$. To proceed, the current density can be related to the drift velocity [43] by $J = -n_e e u$ where u is the electron fluid velocity that satisfies eq. (2.19). Ignoring B and thermal pressure, this relationship becomes

$$\frac{\partial \vec{J}}{\partial t} = \frac{n_e e^2}{m} \vec{E} = \omega_p^2 \epsilon_0 \vec{E} \quad (2.26)$$

using eq. (2.15) which can be combined with eq. (2.25) to obtain a differential equation for the electric field

$$[\nabla^2 + \frac{\omega^2}{c^2} (1 - \frac{\omega_p^2}{\omega^2})] \vec{E} = 0 \quad (2.27)$$

By just focusing on the x-dependence, we can simplify this equation to

$$\frac{d^2 E}{dx^2} = \frac{1}{l_s^2} E \quad (2.28)$$

where $l_s^2 \equiv \frac{c^2}{\omega^2 - \omega_p^2}$ defines the *skin depth* l_s . In the case where $\omega < \omega_p$, l_s^2 is negative and the solution has a sinusoidal dependence

$$E(x) = E(0) \cos(x/l_s) \quad (2.29)$$

On the other hand, when $\omega > \omega_p$, l_s^2 is positive and the solution has an exponential dependence

$$E(x) = E(0) \exp(-x/l_s) \quad (2.30)$$

This “evanescent” behavior when $\omega > \omega_p$ occurs because the electrons cannot respond fast enough to the higher frequency ω . Since the field cannot propagate effectively for $x > 0$, the plasma ends up reflecting a significant portion of the light. The critical density n_c is defined as the electron density where $\omega = \omega_p$. Using eq. (2.15), this can be expressed as

$$n_c \equiv \frac{m \epsilon_0}{e^2} \omega^2 \quad (2.31)$$

When $n_e > n_c$, the plasma is said to be *overdense* and most of the laser light gets reflected. When $n_e < n_c$, the plasma is said to be *underdense*, and the laser light can propagate through the plasma.

2.3.2 Absorption Mechanisms

A typical Ti:Sapphire laser has a wavelength of 0.8 μm which corresponds to a critical density of $n_c \simeq 1.7 \times 10^{27} \text{ m}^{-3}$. In this work, two materials are of interest: gold and ethylene glycol which have densities of 19.3 g cm^{-3} and 1.11 g cm^{-3} respectively. These mass densities correspond to a number density of electrons $5.9 \times 10^{28} \text{ m}^{-3}$ and $1.1 \times 10^{28} \text{ m}^{-3}$ assuming a singly ionized plasma. If the plasmas were multiply ionized, these densities would be even higher. Even though these plasmas are clearly overdense, experiments show energy gets efficiently coupled to the electrons. Consequently, there must exist mechanisms of

absorption consistent with the fact that most of the laser energy can only be deposited in a small depth l_s into the plasma.

Resonance Absorption

The discussion in subsection 2.3.1 applied to an electric field directed in the x -direction. For gaussian laser beams, the electric field is always perpendicular to the direction of propagation. So, if the laser beam is to be directed toward a target at $x = 0$, normal incidence would imply that the electric field $E_x = 0$. Additionally, an s-polarized beam would have an electric field only in the z direction. As a result, the typical model of a laser beam depositing energy into a plasma involves a p-polarized laser beam traveling obliquely in the $x - y$ plane with some angle of incidence θ_i measured with respect to the normal direction of the target. Physically, plasma oscillations occur through fluctuations in density which are going to be the strongest in the x direction due to the interface between vacuum and matter.

Kruer [44] argues that the reflection of light at oblique incidence occurs at a density $n_e = n_c \cos^2(\theta_i)$ by enforcing momentum conservation of the electric field component in the y direction. Even though we've discussed density profile as an abrupt step (from 0 to n_e from crossing $x = 0$), an actual experiment would see some pre-heating of the target before the target becomes ionized and behaves as a mirror at the critical density. This can be characterized by some scale length $L_p \equiv n_e (\frac{\partial n_e}{\partial x})^{-1}$ which is smaller for steeper density profiles. As a result, at higher incidence angles, the evanescent portion of the electric field has to travel further into the underdense region of the target to reach the critical density.

When the frequency of the laser $\omega \simeq \omega_p$, the laser light is in resonance with the plasma oscillations and the energy can be most efficiently absorbed. To maximize the amount of energy reaching the critical density surface in resonance, we would want θ_i to be large so that the electric field has a significant component in the x direction, but also small enough so that the field doesn't diminish too much by traveling in the evanescent underdense region. Denisov [45] and others [46–48] address this question and develop a model for this so-called *resonance absorption*. An approximate version of this formula is given by Kruer [44]

$$\phi(\tau) \simeq 2.3\tau \exp(-2\tau^3/3) \quad (2.32)$$

where $\tau \equiv (kL_p)^{1/3} \sin(\theta_i)$ takes into account both the scale length and incidence angle. fig. 2.4 shows the fractional absorption $\phi(\tau)^2/2$ of the incident light from this model as a function of θ_i for various scale lengths. There is an optimal angle $\theta_{max} \approx \arcsin(0.8(kL_p)^{-1/3})$ that maximizes the absorption fraction (although Kruer notes that his simple model overestimates the peak absorption – the fraction should peak at around 0.5 [44]).

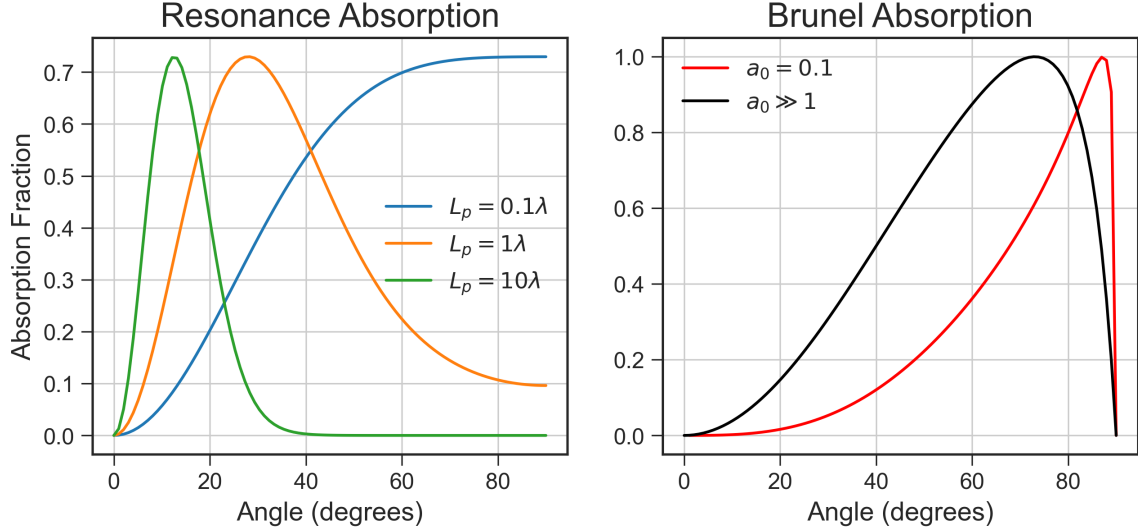


Figure 2.4: Absorption fraction as a function of incidence angle θ_i . For resonance absorption, the density scale length L_p is varied in terms of the laser wavelength $\lambda = 0.8 \mu\text{m}$. For the Brunel mechanism, fractions are plotted for two regimes $a_0 \ll 1$ (where a value of $a_0 = 0.1$ was chosen) and for $a_0 \gg 1$ (which has no dependence on a_0).

Brunel Heating

Resonance absorption only makes sense when the amplitude of the plasma oscillations $x_{\text{osc}} = v_{\text{osc}}/\omega = \frac{a_0\lambda}{2\pi}$ is less than the scale length L_p [12]. Otherwise there is not enough available space for the oscillations to take place. For $\lambda = 0.8 \mu\text{m}$ and $a_0 = 1$, $x_{\text{osc}} = 127 \text{ nm}$. However, for extremely small scale-lengths, efficient electron heating can still be observed [49]. Consequently, a different type of heating mechanism is responsible in this case (somewhat confusingly) called “not so resonant, resonant absorption” [11]. This model, developed by Brunel, is also known as *vacuum heating* and will be explained below.

Before explaining the Brunel mechanism, it is instructive to explain Corkum’s 3-step model for [high-harmonic generation \(HHG\)](#) [50] should be reviewed⁹. This model involves a strong oscillating electric field $E(x) = E_0 \cos(\omega t)$ incident on an atom that ionizes an electron at $t = t^*$. Under the influence of the oscillating field, the (initially stationary) electron will gain and lose energy by moving away from the atom and returning back toward the atom. When $t^* \neq n\pi$ for integer n , it is actually possible for the electron to return back to the atom with non-zero energy. In fact, when $\omega t^* \approx 17^\circ + n(180^\circ)$, the electron returns with an energy peaking at $3.17U_p$ where U_p is the ponderomotive potential given by eq. (2.13). Furthermore, modeling the ionization rate through quantum-mechanical

⁹Readers may find this model more familiar due to the recent 2023 Nobel Physics Prize won by Ohio State’s Pierre Agostini [51] which utilized the ideas of this model to produce attosecond pulses

tunneling of an electron through a Coulomb potential warped by the oscillating laser field, we also determine that the most probable energy for an electron is strongly peaked at the $3.17U_p$ cutoff. In short, this model shows how a laser field can produce electrons with energy on the scale of the ponderomotive potential with high probability at a frequency of twice per optical cycle.

The Brunel mechanism [11] considers a laser field incident on a planar target at $x > 0$ and vacuum at $x < 0$. In order for the electrons to escape the target, there needs to be some component of the electric field in the x direction. Thus, we need to consider oblique incidence and p-polarization just like with resonance absorption. When the plasma scale length is small, the electrons will be able to travel far enough in the $x < 0$ region to escape the plasma entirely and gain energy on the order of U_p in a similar fashion to Corkum's model [50]. Electrons returning to the target at just the right time will penetrate deeper than the skin depth $l_s \approx c/\omega_p$ and be inaccessible to the laser field [12]. These *hot electrons*, generated primarily on the front surface of the target, will provide the energy to heat the remainder of the overdense target region that the laser field cannot directly access.

The optimal angle would appear to be for grazing incidence ($\theta_i = 90^\circ$), but Gibbon notes that accounting for imperfect reflection of the laser field and relativistic energies of the electrons, the efficiency no longer diverges at $\theta = 90^\circ$ [12]. In fig. 2.4, some estimates for the absorption efficiency are plotted according to a simplified model developed by Gibbon [12] based on Brunel [11].

Other Mechanisms

When the laser field penetrates a distance $l_s \approx c/\omega_p$ into the overdense region of the target, the electrons heat up through collisions at an absorption rate $\eta \propto \frac{\nu_{ei}}{\omega_{p,i}}$ [12] where ν_{ei} is the electron-ion collision frequency. This type of absorption is called the *skin effect*. In this case, we see Fresnel-like reflection and absorption [52] that is effective for large incidence angles. Even when the collision frequency is low, we can still get efficient absorption as long as the thermal electron motions are large compared to the skin depth (i.e. $v_{th}/\omega > l_s$) [12]. This phenomena is called the *anomalous skin effect* that is also most effective at large incidence angles.

All of the mentioned phenomena work best at oblique incidence in p-polarization. But, for relativistic intensities, additional heating mechanisms arise. When $a_0 \gtrsim 1$, the magnetic portion of eq. (2.5) becomes significant. At normal incidence, the electric and magnetic field components both fall in the $y - z$ plane. The electric fields move the electrons strongly causing a current \vec{J} which in turn will interact with the laser magnetic field \vec{B} in the direction perpendicular to both. As a result, this type of heating is known as $\vec{J} \times \vec{B}$ heating [12, 53]. Because $\vec{J} \times \vec{B}$ is in the direction of propagation, this effect is most pronounced at normal incidence.

At even higher intensities, the laser can directly impart energy to the electrons through radiation pressure [54] because photons themselves carry momentum. These mechanisms are explored further in section 2.4. In reality, all experiments involve a combination of several different electron heating mechanisms. Consequently, many experiments and simulations have been devoted to parametric studies that show how parameters (L_p , θ_i , polarization, a_0 , etc.) affect electron absorption [55].

2.4 Ion Acceleration

The previous section gave an overview of the laser-plasma interactions and how they can efficiently couple energy into hot electrons. Regardless of heating mechanism, one theme is common to all – the energy gained by an electron’s quiver motion in an oscillatory field, known as the ponderomotive potential (eq. (2.13)) sets the scale for the hot electron temperature T_h . That equation was only valid for non-relativistic electrons, so we must replace $U_p = \frac{1}{4}mv_{\text{osc}}^2$ with the relativistic energy $U_p \equiv (\gamma - 1)mc^2$ where $\gamma = 1/\sqrt{1 - \frac{v_{\text{osc}}^2}{c^2}}$ defines the lorentz factor. We can combine this with the relativistic momentum $p = \gamma mv_{\text{osc}}$ and eq. (2.9) to determine an approximate expression of γ in terms of a_0

$$\gamma \approx \sqrt{1 + a_0^2} = \sqrt{1 + \frac{I_{18}\lambda_{\mu m}^2}{1.37}} \quad (2.33)$$

where I_{18} is the peak intensity of the laser pulse in $1 \times 10^{18} \text{ W cm}^{-2}$ and $\lambda_{\mu m}$ is the wavelength in μm . In 1992, Wilks [8] conducted simulations to show that T_h is on the order of U_p .

$$k_B T_h \approx mc^2(\gamma - 1) \quad (2.34)$$

In fig. 2.5, we can see that the *Wilks scaling* (pink) closely matches ultra-intense laser experiments. The other scalings in the figure are similarly validated by computational simulations and are all proportional to $(I\lambda^2)^\alpha$, where $0 < \alpha \leq 1$. As a result, the product $I\lambda^2$ is an important quantity in laser-plasma experiments and is called the *irradiance*. Wilks also outlines a way to measure the hot electron temperature in his simulations [8] by taking the slope of $\frac{dN_e}{dE}$ in the *MeV* regime¹⁰.

Since protons are 1836 times as massive as electrons, they are much harder to accelerate and (on the scale of femtosecond pulse interactions) are essentially immobile. Despite this, ultra-intense laser experiments have demonstrated proton acceleration is possible. This section will explain the **TNSA** mechanism for accelerating protons and light ions which is heavily dependent on T_h . Then, we will discuss alternative acceleration mechanisms. Finally, we’ll overview some important applications.

¹⁰For example, the slopes in Figure 4.9(b) yield a T_h between 2 and 3 MeV

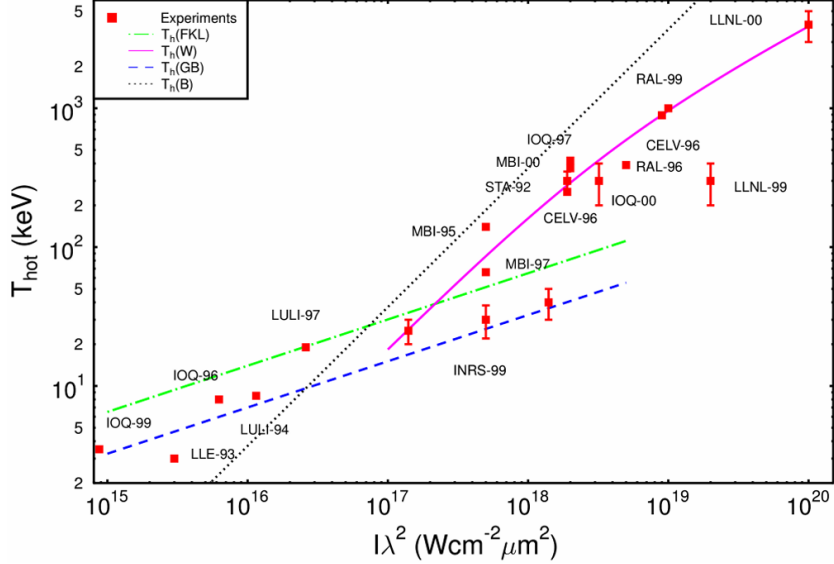


Figure 2.5: Experimentally recorded hot electron temperatures as a function of irradiance $I\lambda^2$ are plotted as red squares. The empirical scaling models are given by Wilks [8](pink, solid), Gibbon and Bell [9](blue, ashed), Forslund et. al. [10](green, dash-dot), and Brunel [11](black, dotted). Figure is taken from Gibbon [12]

2.4.1 Target Normal Sheath Acceleration

The observation of energetic protons off the rear side of thin plastic and gold targets has been documented throughout a variety of experiments since the 80s [56]. It might sound unintuitive that we would even see protons in the first place; after all, when shooting a target like aluminum, one would expect aluminum ions. It turns out that there is always an important and measurable surface contamination layer, primarily composed of hydrogen and light hydrocarbons [57]. Allen [58] showed that when removing the surface contaminant from the backside, we see a strong suppression in ion acceleration. This points to the contaminant layer being the crux of what is accelerated.

TNSA Models

Expansion models have been long known since the 70s and 80s [59, 60] that describe the acceleration of protons with experiments (e.g. Tan [56]) as well. However, CPA [26] allowed the laser peak intensities to reach relativistic levels ($a_0 > 1$) with sub-ps pulse duration as explained in section 1.1.

The first TNSA experiment occurred in 2000 with a group at Michigan [61]. They found 1.6 MeV protons from a thin aluminum foil with a $3 \times 10^{18} \text{ W cm}^{-2}$ class laser at normal incidence. Then, Rutherford Appleton Laboratory (RAL) found 30 MeV protons [62] from

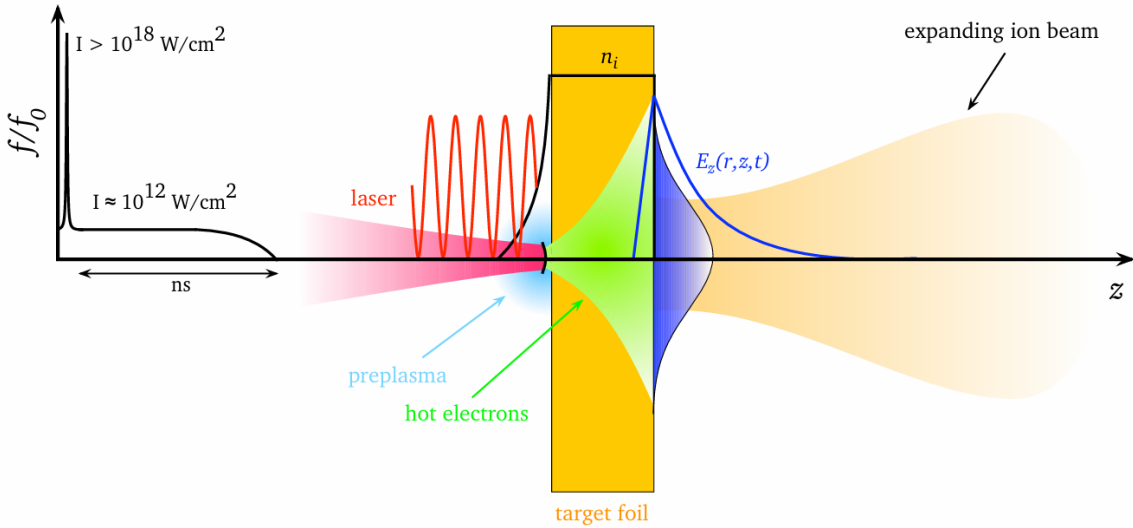


Figure 2.6: The target normal sheath acceleration process is depicted. First, an intense laser pulse irradiates the front side of a target foil of few μm thickness. This generates hot electrons that stream through the foil and re-emerge in a cloud on the rear side. The charge separation of the hot electrons and positively charged target creates intense longitudinal fields ($\sim \text{TV/m}$) that accelerate light ions in the mostly target normal direction. This figure was taken from Roth [13]

a $5 \times 10^{19} \text{ W cm}^{-2}$ class laser incident on a lead target at 45° incidence. Shortly after, Lawrence Livermore National Laboratory (LLNL) found energies up to 58 MeV [63] from a $3 \times 10^{20} \text{ W cm}^{-2}$ class laser on a gold target at 45° incidence.

With efficient MeV proton acceleration demonstrated through multiple studies, a more comprehensive picture of the process emerged. In 2001, Wilks [64] summarized much of the existing literature including the isothermal expansion model [59], existence of a maximum cutoff energy [60], and dependence on hot temperature [8]. Then, he described the TNSA process in the following way [64]

... the prepulse creates large plasma in front of a solid target. Once the main pulse hits the target, a cloud of energetic electrons (1-10 MeV in effective temperature) is generated, which extends past the ions on both the front and back of the target. Since the protons on the back are in a sharp, flat density gradient, they are accelerated quickly (in the first few μm off the target) to high energies in the forward direction ... On the front, the outermost ions are in a sphere, in a long scale length plasma (due to prepulse) and therefore are accelerated to lower energies, and are spread out into 2π steradians.

A visual of the TNSA process can be seen in fig. 2.6. Although Wilks [64] provided a physical picture of the TNSA process, existing models didn't always match up to experi-

ments. For this reason, the ensuing decade saw much progress in the development of models to describe the spectrum of TNSA accelerated protons. Perego [65] gives a good review of some of the leading models developed and tested against experiments in the 2000s and these models will be summarized below.

First, are the isothermal expansion (fluid) models which include Mora’s “Plasma Expansion into a Vacuum” [20] (2003) that combine eqs. (2.4) and (2.21) with fluid eqs. (5.6a) and (5.6b). This model underlies the work done in chapter 5, where it is explained in more detail, and has the issue of predicting proton energies that can go up to arbitrarily high values. As a remedy, Mora [66] addresses this in a different way (2005) by instead assuming an adiabatic model and limiting the target to be a thin foil (instead of a semi-infinite target).

Alternatively, Passoni and Lontano [67] introduces an upper limit to the integration range of the electric potential instead of using the fluid equations. In this approach, the electric fields determined from the potential are considered static, and the ensuing ion dynamics is determined by placing a test ion in the field. Further iterations incorporate some distribution of speeds for the electrons (non-relativistic Maxwell-Boltzmann [68] or relativistic Maxwell-Juttner [69]) and use an empirically determined scaling for the peak energy of electrons (as a function of laser energy) that do not escape the system [70].

Furthermore, some hybrid models include elements of both fluid and quasistatic models like Robinson [71] and Albright [72].

Optimization of TNSA process

Since the TNSA process is intimately related to hot electron generation at the front of the target and a flat density gradient at the back, many efforts have been taken to design targets that optimize ion acceleration. Patel [73] used spherically shaped targets to act as a lens that focus the proton beam. MacKinnon [74] showed lower target thickness leads to higher proton energy due to a higher mean density of hot electrons at the surface. More recent experiments have even used nanowires [75] and microtubes [76]. Many experiments generally find that there is an optimal level of pre-expansion of the target that enhances hot electron generation and ion acceleration (e.g. McKenna [77]).

Another way to increase the peak proton energy of the emitted spectrum is to use two spatially aligned pulses. If one pulse has a delay with respect to the other, the first pulse could pre-expand the target to provide an optimal electron density at the front surface [78]. If the pulses are also temporally aligned, the constructive interfere at the target front surface may prove beneficial [18]. The second approach is called **enhanced target normal sheath acceleration (eTNSA)** and chapter 4 is devoted to this phenomenon.

See the review article by Roth [13] for a more comprehensive list of the different approaches to enhance TNSA.

2.4.2 Other Acceleration Mechanisms

[TNSA](#) is not the only method in which protons can be accelerated. For intensities of greater than $10^{21} \text{ W cm}^{-2}$, laser-induced ion shocks can start to play a significant role [79]. For even higher intensities $\sim 10^{23} \text{ W cm}^{-2}$, the radiation pressure of electromagnetic waves can efficiently transfer momentum to ions [79]. See Macchi [54] for a more in depth discussion on these topics. One way to differentiate the [TNSA](#) regime from other regimes is through the following equation relating a_0 to various properties of the laser and target

$$a_0 = n_e \lambda r_e l_0 = 224 \left(\frac{n_e}{1 \times 10^{29} \text{ m}^{-3}} \right) \left(\frac{l_0}{1 \mu\text{m}} \right) \quad (2.35)$$

Lezhnin [14] uses this equation as a dividing line to differentiate [TNSA](#) from two other mechanisms: [radiation pressure acceleration \(RPA\)](#) and Coulomb Explosions; this can be seen in fig. 2.7. If the laser intensity is sufficiently high and density is low enough to be transparent, the laser can quickly sweep away most electrons to leave behind a strongly positive target. The repelling coulomb force will cause the protons to expand outwards in all directions.

When the radiation pressure $P_{\text{rad}} \approx 2I_0/c$ is significant enough to overcome the thermal expanding pressure $n_e k_B T_e$, ions can accelerate directly through the transfer of momentum. [54]. In this regime, laser absorption into hot electrons by traditional mechanisms would be detrimental. By shooting the laser at normal incidence with circular polarization, resonance absorption and $\vec{J} \times \vec{B}$ heating can be minimized as seen in section 2.3.

For thick targets, this immense pressure can impart a parabolic deformation that allows the laser to penetrate further. This is the regime of *hole boring*. Targets thin enough where the hole boring process reaches the target rear in a time less than the pulse duration are in the *light sail* regime. [54].

Wakefield Acceleration

All the aformentioned acceleration processes only make sense for overdense targets whose electron density is greater than the critical density ($n_e > n_c$). This is because the critical density surface is the primary area where the laser deposits energy into hot electrons. If the target plasma has $n_e < n_c$, the target is said to be underdense and there is no critical density surface where the laser interacts with. Tajima and Dawson [80] first proposed the idea of a “Laser Electron Accelerator” in 1979 that is capable of accelerating electrons to high energies through the non-linear ponderomotive force. If the conditions are just right, the electrons can “surf” a plasma wave in the wake of the pulse and pull along positive ions in a process now known as [laser wakefield acceleration \(LWFA\)](#). A comprehensive review of the subject can be found here [81].

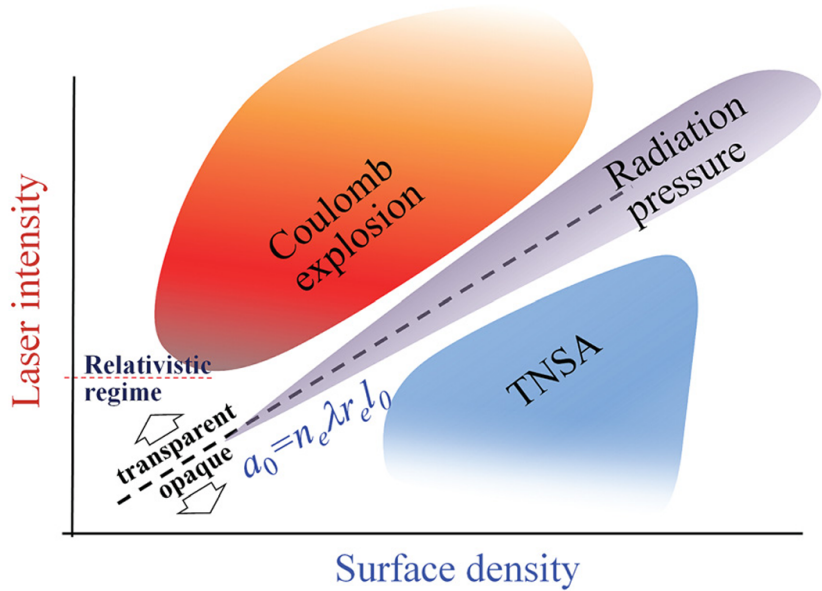


Figure 2.7: The regimes of three different acceleration mechanisms are displayed in terms of eq. (2.35). This figure was taken from Roth [14]

Chapter 3

COMPUTATIONAL METHODS

In this chapter, I will explain some relevant background between two of the computational techniques I've used in this work: the particle-in-cell method and machine learning.

3.1 The Particle-In-Cell Method

The [particle-in-cell \(PIC\)](#) method involves solving Maxwell's Equations on a grid

$$\nabla \cdot \vec{E} = \frac{\rho}{\epsilon_0} \quad (3.1)$$

$$\nabla \times \vec{E} = -\frac{\partial \vec{B}}{\partial t} \quad (3.2)$$

$$\nabla \cdot \vec{B} = 0 \quad (3.3)$$

$$\nabla \times \vec{B} = \mu_0(\vec{J} + \epsilon_0 \frac{\partial \vec{E}}{\partial t}) \quad (3.4)$$

This is combined with the lorentz force

$$\vec{F} = q(\vec{E} + \vec{v} \times \vec{B}) \quad (3.5)$$

which determines the motions (i.e. \vec{r} and \vec{v}) of charged particles by integration. It is impossible to keep track of the true numbers of particles in this type of simulation which would be roughly on the order of Avogadro's number $\sim 10^{23}$. Instead, we lump many particles together into what is called a *macro particle*. For example, one "macro electron" could contain 1 trillion "real electrons". Also, we cannot hope to have infinite precision in calculating quantities of interest. Spatially, we must separate the simulation volume into a grid where each cell has length Δx , Δy , and Δz in the x, y, and z direction respectively. Temporally, we introduce a time step Δt which allows us to propagate Maxwell's Equations forward in time by Δt for every iteration.

For simplicity, non-relativistic equations will be introduced in this section, but they

can easily be generalized to the relativistic versions which are implemented in modern PIC codes. Additionally, some of the equations will assume a 2D grid, but a 3D grid is similarly straightforward to generalize.

3.1.1 Densities and Shape Factors

When a simulation is initialized, all the particles will have a defined position and velocity. The charge density $\rho_{i,j}$ (for the cell at the i^{th} and j^{th} grid point in the x and y directions) is easy to compute – it is simply the sum of all the charges q_α closest to grid point (i,j) divided by the cell area: $\rho_{i,j} \equiv \frac{\sum_\alpha q_\alpha}{\Delta x \Delta y}$ ¹¹. The current density $\vec{J}_{i,j}$ can be obtained similarly – $\vec{J}_{i,j} \equiv \frac{\sum_\alpha q_\alpha \vec{v}_\alpha}{\Delta x \Delta y}$. Assigning the densities to the nearest grid point in this manner is sensibly called **nearest grid point (NGP)** by Birdsall and Langdon [82].

Since the PIC approach contains many real particles for each macro particle, it is desired to smooth the macro particle densities throughout adjacent cells. We can modify the individual density contributions of particles by a shape factor $S(\vec{r}_\alpha - \vec{r})$ that depends on a particle's location \vec{r}_α in relation to a grid point located at \vec{r} . This shape factor is normalized so that integrating it over the area of the simulation yields 1 to ensure the particle number is properly being conserved. The simplest improvement over NGP would be the *top hat* shape factor (also called Cloud in Cell [82]) which assigns density contributions proportional to proximity of the nearest cells within $(\Delta x, \Delta y)$. This has the shape of a uniform distribution and thus looks like a “top hat” in 1D. It is a 0th order shape factor and can be represented by the following equation

$$S_0(x) \equiv \begin{cases} 1 & \text{if } |x| \leq 0.5\Delta x \\ 0 & \text{otherwise} \end{cases} \quad (3.6)$$

A further improvement will weight the particles closer to a particular grid point higher than a particle further away. If this weighting is linear over an area $(2\Delta x, 2\Delta y)$, it is called the *triangle* shape factor and represented by the following equation in 1D

$$S_1(x) \equiv \begin{cases} 1 - \frac{|x|}{\Delta x} & \text{if } |x| \leq \Delta x \\ 0 & \text{otherwise} \end{cases} \quad (3.7)$$

It turns out that the higher order shape factors $S_n(x)$ can be represented by convolutions of $S_0(x)$

$$S_n(x) \equiv \int_{-\infty}^{\infty} S_{n-1}(x') S_0(x - x') dx' \quad (3.8)$$

¹¹This is for a 2D geometry where we implicitly divide by 1 m to get the units right. In 3D, the denominator would have Δz as well

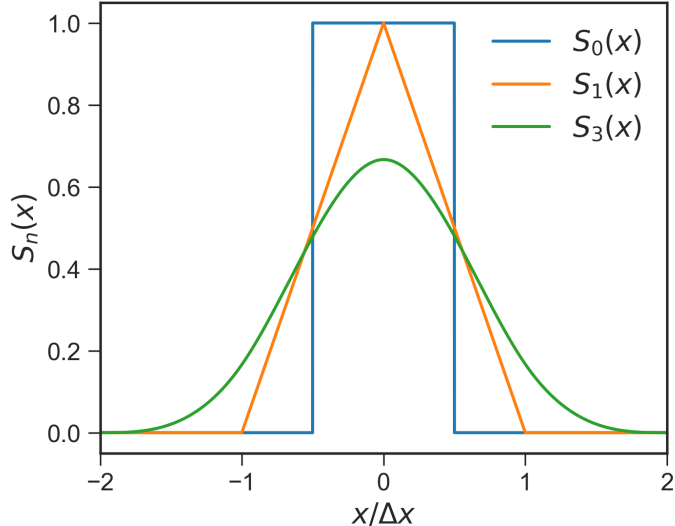


Figure 3.1: The top hat ($S_0(x)$), triangle ($S_1(x)$) and 3rd order spline ($S_3(x)$) are plotted in 1D.

and the shape factors for $n \geq 2$ are commonly called n-splines. The third order spline is used in this work and weights particles over an area $(4\Delta x, 4\Delta y)$ and is represented in 1D by

$$b_3(x) = \begin{cases} \frac{1}{6}(8 - 12|\tilde{x}| + 6\tilde{x}^2 - \tilde{x}^3) & \text{if } 1 \leq |\tilde{x}| \leq 2 \\ \frac{1}{6}(4 - 6\tilde{x}^2 + 3\tilde{x}^3) & \text{if } |\tilde{x}| \leq 1 \\ 0 & \text{otherwise} \end{cases} \quad (3.9)$$

where $\tilde{x} \equiv x/\Delta x$ normalizes the position x . See fig. 3.1 for a comparison of the three shape factors. These shape factors not only apply to the calculation of densities, but also to the electric and magnetic fields. In this way, the fields used to update particle positions and velocities are averaged over neighboring cells.

3.1.2 Field Solver and Particle Push

The PIC method is able to make efficient use of the second order accurate central difference approximation to compute derivatives. A simpler method like Euler integration is only first order accurate and will suffer in terms of accuracy. Higher order methods like 4th order Runge-Kutta have much higher computational costs in terms of operations per time step and memory consumption. The central difference scheme is accomplished by alternately calculating electric and magnetic fields, staggered by half a time step, in an approach called *leapfrog integration* [82]. This can be seen in the right half of fig. 3.2 where the calculations

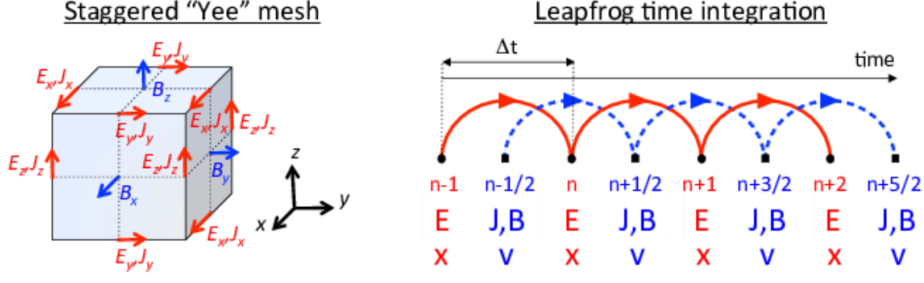


Figure 3.2: The “Yee” grid is depicted (left) where the electric and magnetic field components are staggered by half a cell. The fields, currents, position, and velocity make use of the staggered grid by leapfrog time integration (right). This picture was taken from the WarpX documentation [15] (which is another PIC code).

of E and J, B alternate in a “leapfrog” fashion. It turns out that this staggering also comes with some nice properties like automatically satisfying eq. (3.3). By rearranging eq. (3.2), we can update the electric and magnetic fields through the following equations [83]

$$\vec{E}^{n+1} = \vec{E}^n + \Delta t(c^2 \nabla \times \vec{B}^{n+\frac{1}{2}} - \frac{1}{\epsilon_0} \vec{J}^{n+\frac{1}{2}}) \quad (3.10)$$

$$\vec{B}^{n+\frac{1}{2}} = \vec{B}^{n-\frac{1}{2}} - \Delta t(\nabla \times \vec{E}^n) \quad (3.11)$$

where $\vec{J}^{n+\frac{1}{2}} \equiv \frac{\sum_{\alpha} q_{\alpha} \vec{v}_{\alpha}^{n+\frac{1}{2}}}{\Delta x \Delta y}$ depends on the velocity. The updated velocity for each particle is calculated through the force from eq. (3.5).

$$\frac{v_{\alpha}^{n+\frac{1}{2}} - v_{\alpha}^{n-\frac{1}{2}}}{\Delta t} = \frac{q}{m} [\vec{E}_{\alpha}^n + \frac{v_{\alpha}^{n+\frac{1}{2}} + v_{\alpha}^{n-\frac{1}{2}}}{2} \times \vec{B}_{\alpha}^n] \quad (3.12)$$

The α subscript indicates the quantities are calculated for each particle; thus, the fields are smoothed out by the shape factor (e.g. $E_{\alpha}^n \equiv \int E^n S_3(x - x_{\alpha}, y - y_{\alpha}, z - z_{\alpha}) dx dy dz$). In practice, eqs. (3.10) and (3.11) are broken up into half-steps so that the electric and magnetic field are known for all half-steps. At first glance, eq. (3.12) does not appear to have an explicit solution for $v^{n+\frac{1}{2}}$. There are implicit methods that can solve this equation like Large Scale Plasma: An implicit particle-in-cell code (LSP) [84]. It turns out that there is an explicit solution given by the *Boris Rotation Algorithm*. If we define

$$v^{n+\frac{1}{2}} = v^+ + \frac{q E^n}{2m} \Delta t \quad (3.13)$$

$$v^{n-\frac{1}{2}} = v^- - \frac{q E^n}{2m} \Delta t \quad (3.14)$$

we can separate out the electric field dependence to get

$$\frac{v^+ - v^-}{\Delta t} = \frac{q}{m} \left[\frac{v^+ + v^-}{2} \times B \right] \quad (3.15)$$

which can conveniently be calculated through a rotation [82] through the following steps:

1. Compute v^- from eq. (3.14).
2. Compute $\vec{t} \equiv \frac{q\Delta t}{2m} \vec{B}^n$ (equivalent in magnitude to $\tan(\theta/2)$ where θ is the rotation angle)
3. Compute $\vec{s} = \frac{2\vec{t}}{1+t^2}$ (equivalent in magnitude to $\sin(\theta/2)$)
4. Compute $\vec{v}' = \vec{v}^- + \vec{v}^- \times \vec{t}$.
5. Compute $\vec{v}^{n+\frac{1}{2}}$ from eq. (3.13).

Now, the particles can be advanced or “pushed” from

$$x^{n+1} = x^n + v^{n+\frac{1}{2}} \Delta t \quad (3.16)$$

For completeness, the velocity initially needs to be pushed backwards from $v^0 \rightarrow v^{-\frac{1}{2}}$. This is not done in a time-centered way, but is only needed at the start of the simulation.

3.2 Machine Learning

What is [machine learning \(ML\)](#)? According to the computer scientist Arthur Samuel who popularized the term in 1959 [85], it is the

... field of study that gives computers the ability to learn without being explicitly programmed.

The book *Hands-On Machine Learning with Scikit-Learn* by Aurelien Geron [85] gives a simple example of how a [ML](#) model differs from a more traditional computer program in the form of an email spam filter. A traditional filter would implement user specified rules that mark emails as spam based on e-mail address and subject line keywords for example. A [ML](#) approach would determine what keywords and e-mail addresses to look for based on prior emails that have been flagged as spam.

The key difference in the two approaches is predictive power. The traditional filter removes spam from messages that fit a pattern explicitly given by the user. The [ML](#) filter learns a generalized model that predicts possibly unforeseen types of spam. Since the [ML](#) model is much more general, it is more susceptible to incorrect predictions. In this section, we'll overview how to handle data for [ML](#) algorithms, compare model training for different methods, and explain how these models can be used in practice. The information below is largely from the book by Geron [85] unless specified otherwise.

3.2.1 Pre-processing

ML can be either supervised or unsupervised based on whether the data is labeled with a particular output. In the ML context, model outputs are often referred to as labels and model inputs are often referred to as features. For the e-mail classification example, a supervised model would have training data that is already labeled as spam (or not spam) and an unsupervised model would have to infer if the data is spam by other means (e.g. clustering similar emails together). We will not be considering unsupervised learning in this work because we are ultimately interested in labeled data (which would be electron or proton energy spectra). To train an ML model effectively, there are various things that need to be taken into account:

- Data Quantity: We need a sufficient amount of data in order to learn relevant trends and patterns. For example, a good spam classifier would have many e-mails (thousands to millions) to train on.
- Representative Data: The data should be representative of all data points. A spam classifier trained only on data prior to 2010 will not accurately predict modern spam emails.
- Poor-Quality: The data should not have significant errors, outliers, and noise.
- Irrelevant Features: The input data (features) to the model should all be relevant. For example, taking into account the exact time that a spam e-mail is received may not be the most relevant as spam emails are often sent out at random times.

Failure to take the preceding steps into account can oftentimes lead to one of two things

- Overfitting: This can happen when the data is too complex in relation to the data. An example would be using a polynomial to fit a set of points that fall on a straight line. To fix this, we can constrain the model to make it more simple, gather more training data, or reduce noise in the training set.
- Underfitting: This is when the model is too simple in relation to the data. This can be fixed by selecting a more complex model, using better features, and reducing any constraints on the model.

To improve the quality of the existing data, we can perform *pre-processing* which is the set of actions that transform raw data into data ready to be fed into a ML model. In chapter 6, significant pre-processing was needed which included removing missing values, combining data sources, applying a median-based filter, compressing the spectra into two metrics, and more. One particularly effective method of pre-processing that is specific to ML is data

normalization which makes sure that all the features and labels are approximately on the same scale. The two most common ways to approach this are summarized below:

- Standard Scaling: A particular feature can be transformed through the following: $x_i \rightarrow \frac{x_i - \mu}{\sigma}$ where μ is the mean of all the data points x_i and σ is the standard deviation. This normalizes the data to be centered at 0 and have a standard deviation of 1.
- Min Max Scaling: A particular feature can be transformed by setting the minimum value to 0, the maximum value to 1, and all values in between would be linearly proportional.

The Min Max Scaling is useful when the data is known to be uniformly distributed with a fixed minimum and maximum. The Standard Scaling is more general and works best if the data is normally distributed.

3.2.2 Model Selection

Given a pre-processed dataset, some additional steps are needed before deploying a [ML](#) model. There are many different types of models one can select and even a particular model can have different so-called *hyperparameters* that characterize it. For example, a hyperparameter of the polynomial regression model is the degree. A standard approach to model selection is through *cross-validation* which breaks up a dataset into different partitions and varies which ones are used for training and which are used for model evaluation. If a model has good performance with one partition but not with another, then the model would not generalize well to make good predictions. In the *cross-validation* process we only want to use data from a specified training set and not from a different testing set that we want to make useful predictions on. A typical training-testing split is 80-20% (which is what was used in [chapter 5](#)).

To implement cross-validation, we pick a number of partition arrangements for the training set and evaluate the model performance for each partition for a number of hyperparameter combinations. For the polynomial regression example, we could evaluate the average error between 5 partition arrangements for polynomial degree ranging from 2 to 7 and pick the model that has the lowest amount of error. In python, we use the `GridSearchCV` module of scikit-learn [86] package to handle cross-validation for a “grid” of hyperparameter combinations.

To evaluate model performance, one needs to choose an error (or accuracy) metric. Two common error metrics are the [mean squared error \(MSE\)](#) and the [mean absolute percentage error \(MAPE\)](#) which are defined as follows:

$$\text{MSE} \equiv \frac{1}{N} \sum_{i=1}^N (y_i - \hat{y}_i)^2 \quad (3.17)$$

$$\text{MAPE} \equiv \frac{1}{N} \sum i = 1^N \left| \frac{y_i - \hat{y}_i}{y_i} \right| \quad (3.18)$$

where y_i is a particular output value, \hat{y}_i is the [ML](#) model prediction, and N is the number of points in the dataset. By defining these error metrics, the model with the lowest cross-validation error should be the best model.

3.2.3 Model Types

A polynomial model is one simple model that involves minimizing the [MSE](#) between data values and model predictions of the following formula:

$$\hat{y} = \beta_{0,0} + \beta_{1,0}x_1 + \beta_{0,1}x_2 + \beta_{1,1}x_1x_2 + \dots \quad (3.19)$$

where $\beta_{i,j}$ are the polynomial coefficients. This equation incorporated two inputs x_1 and x_2 but can be generalized for any number of inputs. These coefficients can be found by a least-squares minimization algorithm [85].

In principle, any dataset can be fit by a polynomial model of a sufficiently high degree. However, such a model would be prone to overfitting – a good model with predictive power should be able to predict data not yet seen. Wolpert [87] famously showed in his 1996 paper that if we don't make any assumptions about the data at hand, then there is no reason to prefer a particular [ML](#) model over another. This is sometimes referred to as the *no free lunch* theorem. Therefore, it is always instructive to experiment with a variety of models to see which one works best.

Instead of a polynomial, more sophisticated regression models can be used like the ridge regression which uses a regularization hyperparameter to avoid overfitting. In a similar vein, [support vector regression \(SVR\)](#) (which falls in the class of support vector machines) uses a regularization parameter that tries to maximize the number of data points that are close to the prediction within some margin. A big advantage of the [SVR](#) is that it can take advantage of the so-called “kernel trick” which allows the model to use higher dimensional features (like the polynomial model), but without explicitly calculating all the higher order components. Importantly, this has both time and memory saving implications. A common “kernel” is the [radial basis function \(RBF\)](#) which calculates a similarity measure between two data points involving a dot product and is easy to compute.

Another regression method that can make use of the kernel trick is the Gaussian Process – a method that doesn't just construct one function to fit the data, but rather a distribution of functions that all fit the data. The functions can effectively be averaged to create a

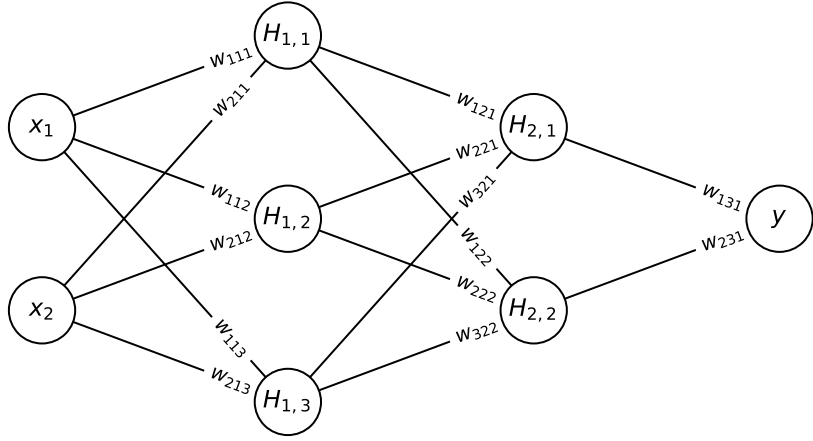


Figure 3.3: A neural network architecture with labeled weights between the nodes in adjacent layers. This network has 2 inputs, 1 output, and 2 hidden layers (which have 3 or 2 nodes in each).

[gaussian process regression \(GPR\)](#) or an uncertainty can be quantified by taking a standard deviation of the distributions at a particular point. These are particularly useful in the context of [bayesian optimization \(BO\)](#) where the uncertainty information can inform new parameters to explore when data is expensive or difficult to obtain.

A more general purpose model capable of learning functions of high complexity is the [neural network model \(NN\)](#). This model, just like a linear regression, fits an intercept and coefficients to each input variable. However, the [NN](#) chains many of these linear regressions together – that is the output of one linear regression becomes the input of the next linear regression. The intermediary outputs are computed in the *hidden layers*. Since a sequence of linear regressions will only produce another linear regression, *activation functions* are needed to introduce non-linearity between the layers. The simplest activation function is the [Rectified Linear Unit \(ReLU\)](#) which is defined as

$$\text{ReLU}(x) = \begin{cases} x & \text{if } x > 0 \\ 0 & \text{otherwise} \end{cases} \quad (3.20)$$

To illustrate how this model works, one can look at [Figure 3.3](#). This network shows nodes that are connected by weights w_{ijk} where i is the vertical position of the node in the previous layer, and j is the numbered hidden layer, and k is the vertical position of the node in the current layer. To calculate $H_{1,1}$ for example, one would take a sum of the inputs multiplied by corresponding weights with an additional bias term (and then apply an activation function)

$$H_{1,1} = \text{ReLU}(b_{11} + w_{111}x_1 + w_{211}x_2) \quad (3.21)$$

or more generally $H_{1,k} = b_{1k} + \sum_i w_{i1k}x_i$. To calculate $H_{2,1}$ one would need to add up the contributions from $H_{1,1}$, $H_{1,2}$, and $H_{1,3}$

$$H_{2,1} = \text{ReLU}(w_{121}H_{1,1} + w_{221}H_{1,2} + w_{321}H_{1,3}) \quad (3.22)$$

In this way, the intermediary hidden layers provide a number of free parameters equal to the number of weights w_{ijk} (the number of edges) added to the number of bias terms b_{ijk} (the total number of nodes excluding the input layer). Due to the interconnected nature of the model, the output will depend on every edge weight that is along the path from an input node to the specified output node. To train the **NN**, one can employ the method of *gradient descent*. This involves calculating the gradient of a designated error metric (like the **MSE**) with respect to the model parameters (weights and biases). These gradients inform how the model should be updated to minimize the **MSE**. If θ is a model parameter, this update is given as

$$\theta_{\text{new}} = \theta_{\text{old}} - \eta \nabla_{\theta} \text{MSE}(\theta) \quad (3.23)$$

Here, η is called the *learning rate* and is a scale factor that controls the magnitude of the update. This is an iterative procedure where at each step, the model output is calculated and the weight updates are computed from the gradients¹². Each of these iterations is called an *epoch* which can furthermore be divided by training the data in multiple batches (instead of all the data with one pass). The training process can terminate after a specified number of epochs or a stopping criteria can be established when the **MSE** reaches a certain value.

In general, the more nodes and hidden layers a model has, the more free parameters can be trained. The **NN** model used in [section 5.3](#) uses an architecture with 12 hidden layers and 64 neurons per layer for a total of 2,929,155 free parameters and can be visualized in [Figure 3.4](#).

¹²The model output calculation is sometimes called the “forward pass” and gradient update is sometimes called the “backward pass” or “back-propagation”.

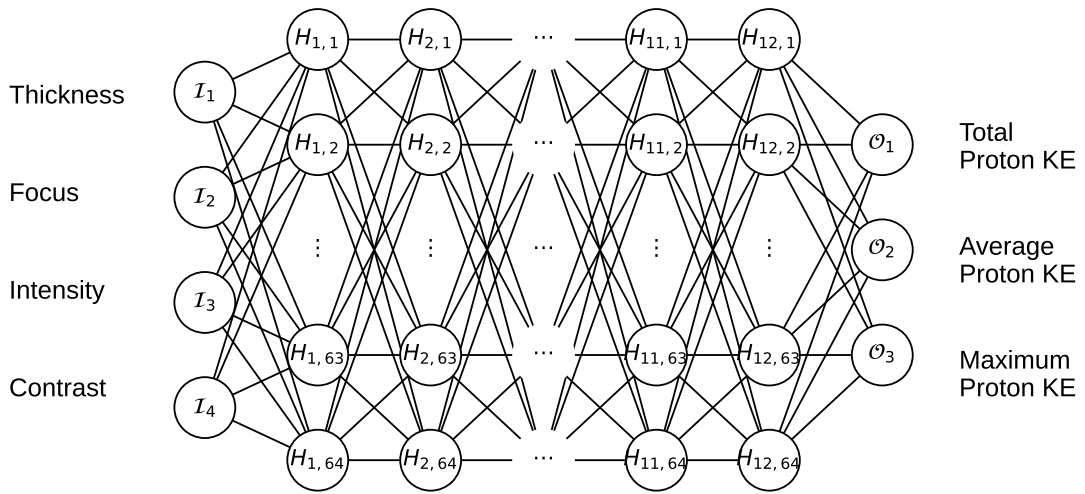


Figure 3.4: The neural network architecture used in section 5.3. This network has 4 inputs, 3 outputs, 12 hidden layers, and 64 neurons per hidden layer.

Chapter 4

PARTICLE-IN-CELL SIMULATIONS OF ENHANCED TARGET NORMAL SHEATH ACCELERATION

This chapter details the [PIC](#) simulations I conducted to better understand the [eTNSA](#) experiments at [LLNL](#) by Nathaniel Tamminga, Joseph Snyder, and John Morrison in March of 2024. They worked at Titan (which is housed in the [Jupiter Laser Facility \(JLF\)](#)) for 6 weeks using their earned LaserNetUS *shot time*. I will mostly focus on the simulation aspect of the project, but include some relevant comparisons to the experiment as needed.

4.1 Background

4.1.1 Spatially Aligned Pulses

As explained in section 2.4.1, there is generally an optimal level of pre-expansion of the target to maximize the [TNSA](#) proton energies [77, 88]. While the pre-expansion could be due to a low contrast pulse, it could also be due to an artificially injected pre-pulse whose intensity and temporal delay are tunable. Robinson et. al. [89] first addresses the idea of using multiple high intensity 40 fs laser pulses with the first being one-tenth to one-quarter of the intensity of the second. They termed this novel two-stage process *multiple pulse sheath acceleration*. This study found a reduction in peak proton energy through numerical simulations, but did find the existence of spectral peaks – spikes in the energy spectrum at specific energies. A few years later, Markey et. al. [16] examined a similar setup experimentally, varying the temporal separation by 0.75-2.5 ps. Interestingly, they found an enhancement in the peak proton energy with a 0.75 ps separation and energy ratio of 0.4:1 between the two pulses. They conducted 1D PIC simulations shown in fig. 4.1 that verify this as well.

In 2018, Ferri et. al. [78] re-examines the same question, but uses the same intensity for both pulses. He finds that ultimately, little to no delay is optimal and as the delay gets

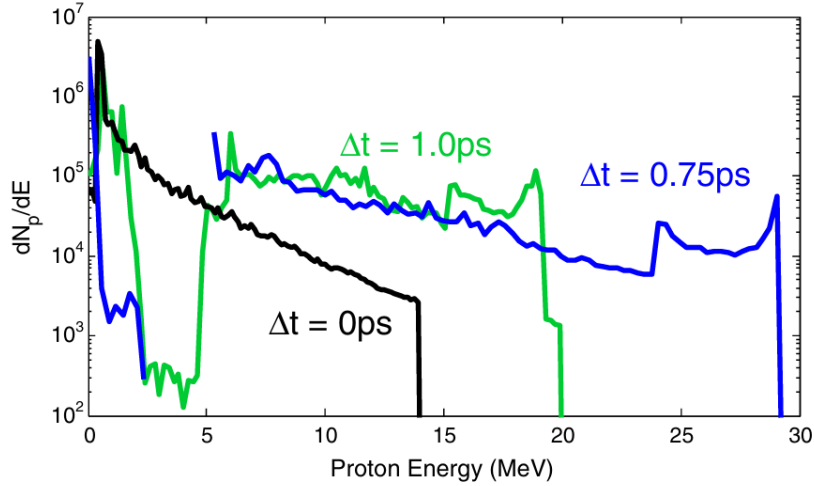


Figure 4.1: Proton energy spectrum from 1D particle-in-cell simulations depicted for three different temporal delays (including $\Delta t = 0$) from FIG. 3 in Markey et. al. [16].

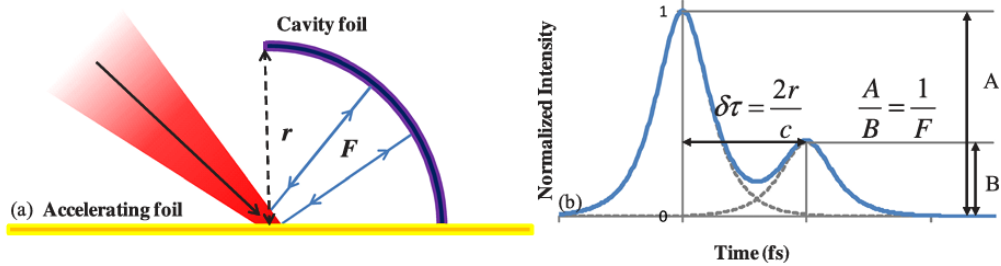


Figure 4.2: Schematic of the incident laser on the half-cavity target (left) in Scott et. al. [17]. The radius of the cavity foil determines the delay ($\tau = 2r/c$) between the main pulse and the post-pulse (reflected laser light of $\sim 40\%$ energy of the main pulse).

larger, the enhancement reduces to the single pulse result. He finds the acceleration process can be affected by the second pulse for time delays as long as 0.6 ps for $3 \mu\text{m}$ targets and 1 ps for $6 \mu\text{m}$ targets.

In a different approach Scott et. al. [17] realized that much of the laser light that is reflected is wasted, so a mechanism to re-direct this light back into the target would be desired. They designed a target with a half-cavity foil as seen in fig. 4.2 that will take light reflected off the accelerating foil and re-reflect it back towards the accelerating foil. They find that this can increase the laser to proton energy efficiency by up to $\sim 55\%$.

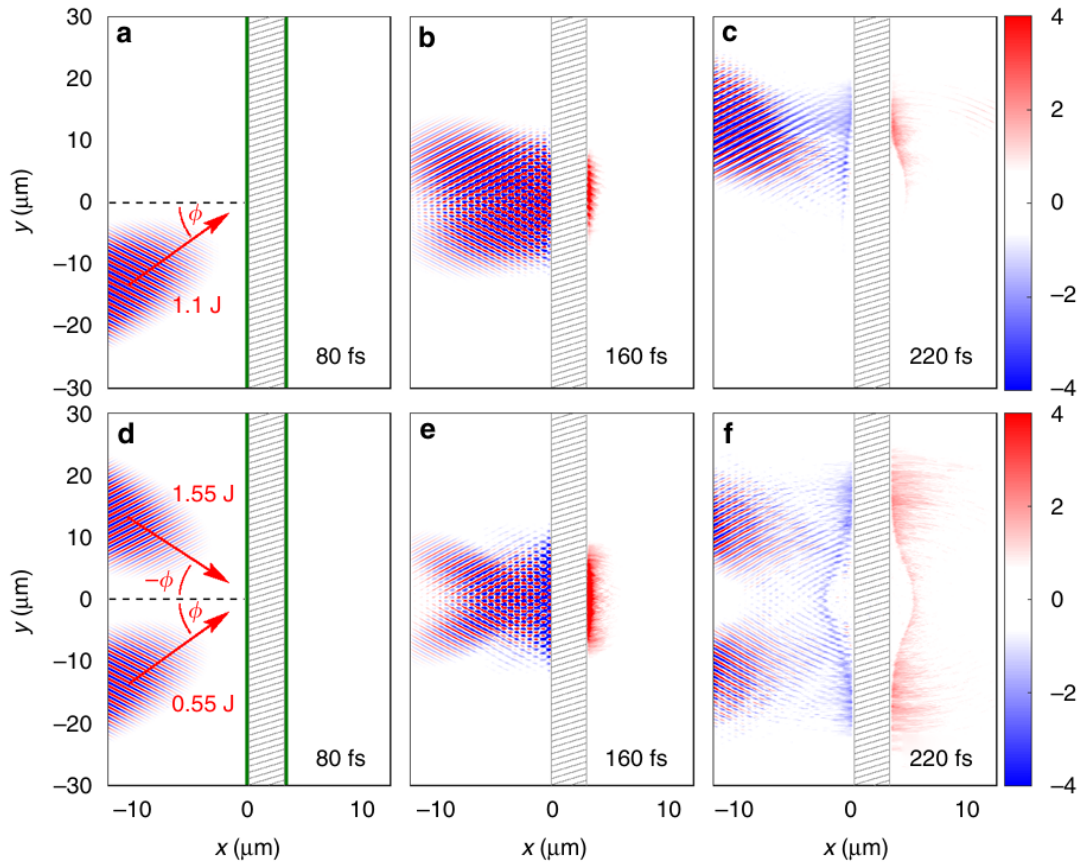


Figure 4.3: Geometry of the two pulse scheme as shown in Figure 1 of Ferri et. al. (2019) [18]. The single pulse has a total energy of 1.1J at an incidence angle of $\phi = 45^\circ$ and is shown through several time snapshots (a-c). In (d-f), the double pulse is shown through those same time snapshots with energies of 0.55 J in each pulse (the 1.55 J is a typo from the original figure). Other parameters include $\tau_{\text{fwhm}} = 38 \text{ fs}$, thickness = 3 μm , material = aluminum, $w_{0,\text{fwhm}} = 5 \mu\text{m}$, $I_0 = 7 \times 10^{19} \text{ W cm}^{-2}$.

4.1.2 Enhanced TNSA from Ferri et. al.

Given the results of the previous section [16, 17, 78] that use short-delay pre or post pulses, Ferri, Siminos and Fulop decided to study how spatially *and* temporally aligned pulses can enhance proton acceleration. They showed that the double pulse setup can result in an almost doubling of the proton energy and five-fold enhancement in the number of protons [18] through PIC simulations. This phenomena, referred to as eTNSA, is depicted in fig. 4.3 which shows the constructive interference of the fields at the front of the target in the center panel (e) and enhanced TNSA fields at the target rear (f).

The constructive interference of the electric fields can be understood by considering the electric field of two p-polarized plane waves coming in at angles of incidence ϕ and $-\phi$

$$E_{x,1} = -E_0 \sin(\phi) \sin(ky \sin(\phi) - \omega t + kx \cos(\phi)) \quad (4.1)$$

$$E_{x,2} = -E_0 \sin(\phi) \sin(ky \sin(\phi) - \omega t - kx \cos(\phi)) \quad (4.2)$$

Adding these two fields together results in

$$E_{\text{double}} = -2E_0 \sin(\phi) \sin(ky \sin(\phi) - \omega t) \cos(kx \cos(\phi)) \quad (4.3)$$

which has an amplitude of $|E_{\text{double}}| = 2E_0 \sin(\phi)$. In contrast, a single pulse with twice the energy (intensity) would only have a $\sqrt{2}$ larger electric field ($|E_{\text{single}}| = \sqrt{2}E_0 \sin(\phi)$) which explains the enhanced electric fields seen in the bottom row of fig. 4.3. In an ideal situation where 100% of the laser pulse is reflected, the angles of the two pulses do not need to be equal and opposite – we will get a standing wave pattern from the constructive interference of the incident wave with its reflection and the same $\sqrt{2}$ field enhancement.

Unlike the methods described in section 4.1.1 (which see enhanced proton acceleration from a pre-expanded target), eTNSA relies on the presence of an undisturbed target from the vacuum heating mechanism [11] explained in section 2.3. Vacuum heating relies on the dominance of the electron's quiver motion in the oscillatory electric field in the x-direction, but the magnetic field (which is relevant when $a_0 \gtrsim 1$) may impart a $\vec{v} \times \vec{B}$ Lorentz force (eq. (2.5)) that negatively affects the electron acceleration in the x-direction. Brunel even assumes in his original 1987 paper [11] that we can ignore $\vec{v} \times \vec{B}$ interactions if the laser is split into two equal and opposite angle pulses. Ferri confirms [18], through simulations, that the magnetic field is indeed suppressed in the double pulse case which results in hot electrons accelerated to higher energies.

Furthermore, Ferri ran some simulations exploring different preplasma scale lengths L at a fixed energy, and changing the total laser energy for the flat target [18] which can be seen in fig. 4.4. He finds that a higher preplasma scale length generally increases the max proton energy up to a certain scale length of around $L = 0.6 \mu\text{m}$. The enhancement is seen for all scale lengths, but the gap between single and double pulse diminishes for larger scale lengths. In the double pulse case, a more favorable scaling with laser energy is seen for both the hot electron temperature and maximum proton energy ($E_{0,\text{tot}}$ as opposed to $\sqrt{E_{0,\text{tot}}}$) when comparing double pulse against single. In addition, Ferri comments that, for pulses with total energy greater than 10 J, the proton layer on the rear side starts to entirely disconnect from the bulk of the target during the acceleration, causing proton energies to saturate and become lower than the expected linear scaling.

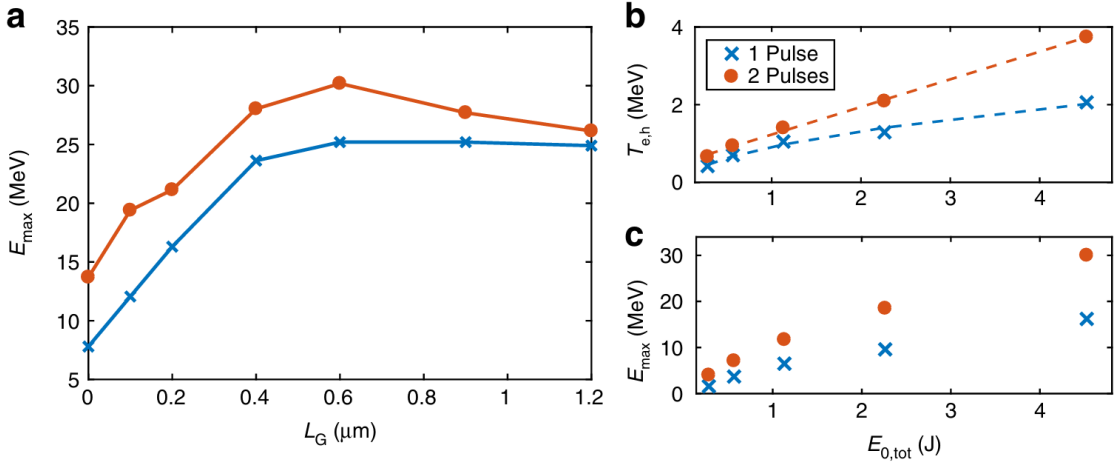


Figure 4.4: Double pulse effectiveness in terms of changing preplasma scale length (a) and total laser energy (b,c) from Ferri et. al. (2019) [18].

4.1.3 Other eTNSA Simulations

In 2021, eTNSA was again demonstrated through simulations in Rahman et. al. [90] for a mJ class laser (around 2 orders of magnitude lower energy than the setup in Ferri's work). This mJ class laser is based on the experimental facility at the Wright Patterson Air Force Base (see chapter 6 for more details) which utilizes a thinner target of $\sim 0.5 \mu\text{m}$. Despite the major difference in laser and target parameters, the findings are similar – increased hot electron temperature and proton energies with double pulse compared to single pulse. However, Rahman finds that the presence of a preplasma actually *reduces* the maximum proton energy. But, like Ferri et. al., the gap between single and double pulse becomes smaller in the presence of a preplasma.

In 2024, Khan and Saxena [91] revisit the double pulse scheme but with an applied longitudinal kilo-Tesla level magnetic field. The purpose of the magnetic field is to reduce the divergence of the hot electron beam. This guides the electrons and enhances the TNSA process to see a higher maximum cutoff energy in the proton spectrum [92]. In this study, the laser was based off of the experimental set-up at RAL with a peak intensity of $5.5 \times 10^{20} \text{ W cm}^{-2}$ incident on a $7 \mu\text{m}$ polyethelene target.

4.1.4 Recent Experiments

Due to multiple studies demonstrating eTNSA [18, 90, 91], experiments are needed to validate the PIC simulations. Morace et al. [93] showed that splitting a 270 J beam ($2.5 \times 10^{18} \text{ W cm}^{-2}$ peak intensity) into multiple “beamlets” on Al foil targets enhances

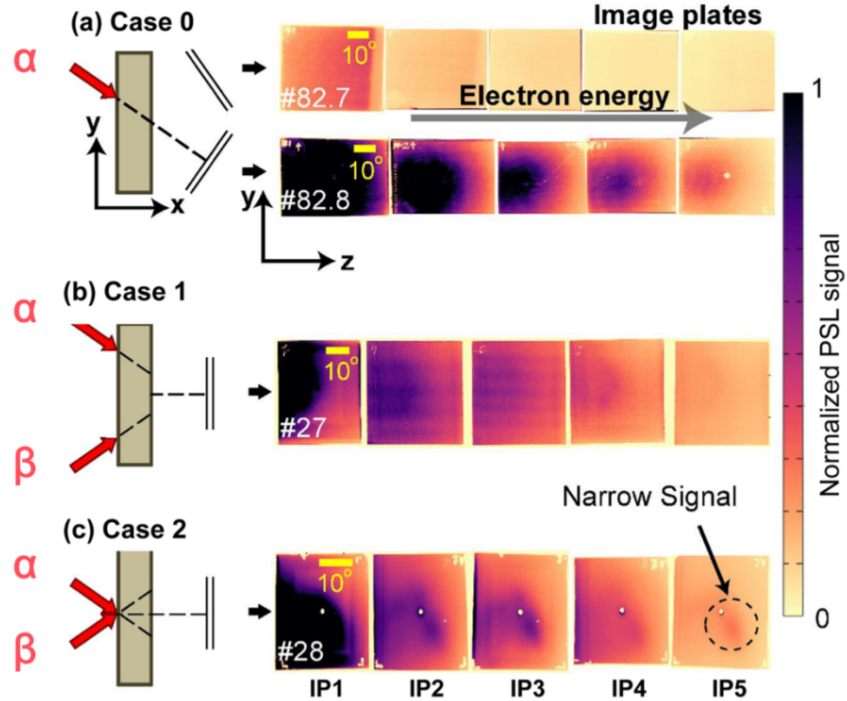


Figure 4.5: FIG. 2 from Yao et al. [19]. Case 0 shows electron signals from a single pulse. Case 1 shows electron signals from a double pulse with spatial separation $120 \mu\text{m}$. Case 2 shows electron signals from a double pulse with no spatial separation.

the proton energy spectrum. These beamlets (dependent on the incidence angle) induced critical surface density modulations that strongly improved absorption into hot electrons.

Yao et al. [19] investigated the double pulse effect by changing the transverse spatial separation between two temporally aligned pulses as shown in Figure 4.5. This figure shows two possible beams α and β which come in at equal and opposite incidence angles with α angled in the $-\hat{y}$ direction. Comparing¹³ (b) and (c) shows an enhancement of the double pulse electron energy when the pulses are spatially overlapped. In terms of the protons, case 2 (spatially aligned double pulses) shows a more collimated central small beam which is absent in case 1 (spatially offset double pulses).

4.2 Titan Experiment

The experimental setup involved one (two) 50 J (25 J) $\sim 10^{19} \text{ W cm}^{-2}$ pulse(s) arriving at a $15 \mu\text{m}$ thick gold target. The Titan laser produces $\tau_{\text{FWHM}} = 2 \text{ ps}$ pulses of wavelength

¹³Note that in Figure 4.5(a), the electron energy is recorded along the laser beam axis unlike (b) and (c) which are in the target normal direction. This does not allow us to compare (a) to (b) or (c) directly, but shows that most electrons are getting accelerated along the laser axis.

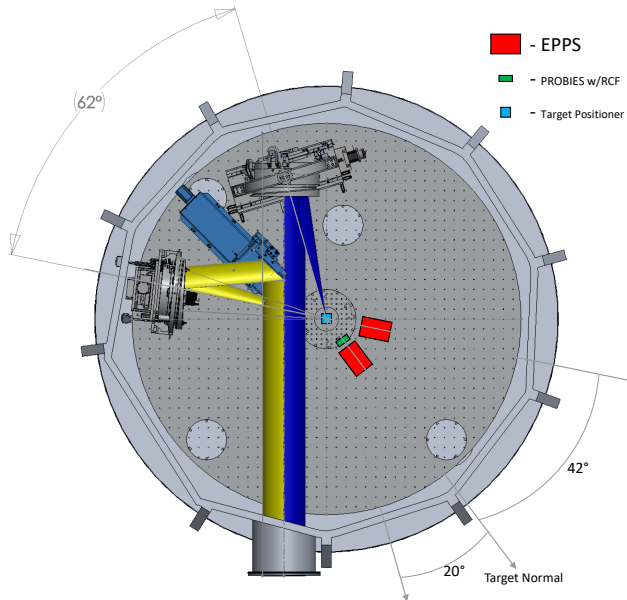


Figure 4.6: Target chamber schematic showing the split beam configuration at the LaserNet Titan experiment conducted in March of 2024. Two independent off-axis paraboloid mirrors focus each beam onto a $15\text{ }\mu\text{m}$ Au target which record proton spectra from multiple electron positron proton spectrometers.

$1.053\text{ }\mu\text{m}$. The beam coming from [off-axis paraboloid mirror \(OAP\)1 \(OAP2\)](#) has an incidence angle of 20° (42°) which can be seen in [Figure 4.6](#) (the blue beam is from OAP1 and the yellow beam is from OAP2). The beam spot size was around $15\text{ }\mu\text{m}$ (in the plane of [Figure 4.6](#)) and $8\text{ }\mu\text{m}$ (normal to the plane of [Figure 4.6](#)) for each beam. The proton beams are recorded by three [Electron Positron Proton Spectrometer \(EPPS\)](#)s which are located along each beam axis and in the target normal direction.

4.2.1 Gold Simulations

To model this setup, we used 2D(3v) simulations using the EPOCH [PIC](#) code (version 4.19.0). For simplicity, both pulses had a fixed spot size of $w_{\text{FWHM}} = 12\text{ }\mu\text{m}$ to enable better comparison between the individual pulses. Using a $2 \times 10^{19}\text{ W cm}^{-2}$ peak intensity, the single pulse would have around 65 J of energy for a sine-squared temporal profile. Accordingly, the double pulse has half the energy and intensity per pulse. We timed the pulses to arrive at the target front around 100 fs into the simulation. Even though the total pulse duration is around $2\tau_{\text{FWHM}} = 4\text{ ps}$, we only run the simulations to 2.2 ps which is more than sufficient to see the highest energy protons produced. Note that there are two single pulse cases, but the figures below choose [OAP2](#) (41°) due to higher sheath fields, electron energies, and proton energies observed throughout the simulations as can be seen

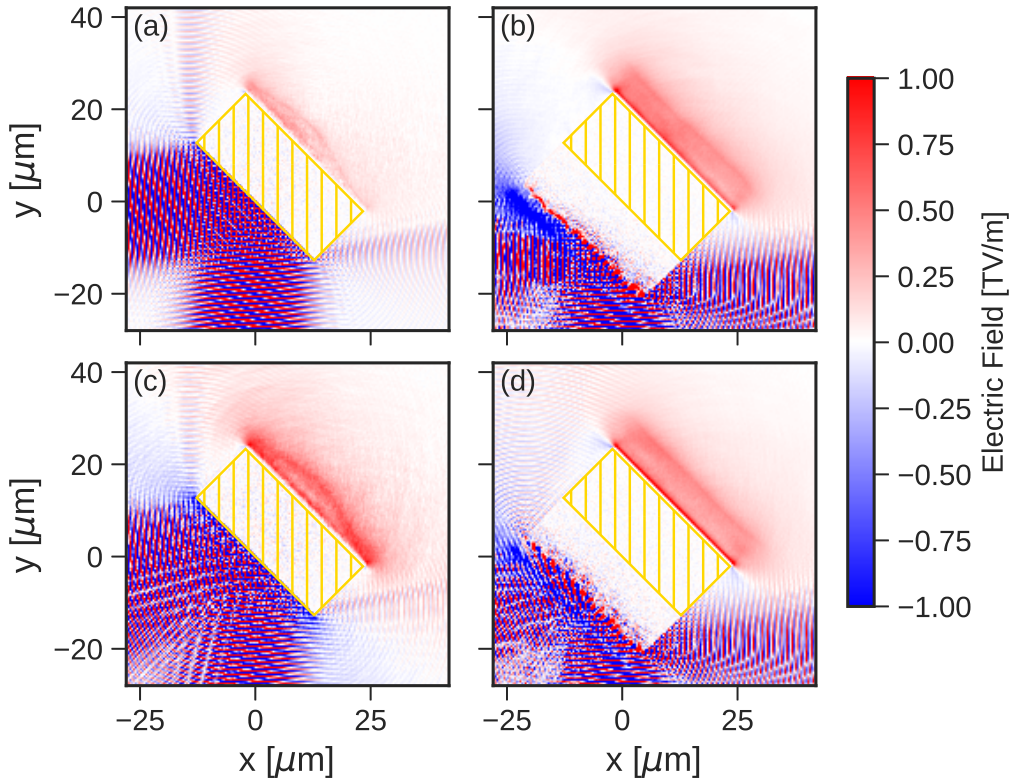


Figure 4.7: Electric field in the target normal direction at simulation time of 800 fs for the (a) flat single 41° pulse, (b) expanded single 41° pulse, (c) flat double pulse, (d) expanded double pulse (on gold 65 J). The hatched gold rectangle is overlaid for a visual of the size of the initial, unperturbed target.

in [Table 4.1](#).

The 15 μm thick target had a length of 36 μm which can be seen in [Figure 4.7](#) rotated at a 45° angle. The gold target had an initial number density $n_0 = 5.9 \times 10^{28} \text{ m}^{-3}$ with a 0.5 μm layer of protons (of the same density) added to the rear side to enhance the [TNSA](#) effect. The gold was initially neutral and allowed to freely ionize through EPOCH's field ionization routine (typically reaching $Z^* = 20$ or $Z^* = 30$ after 1 to 2 ps respectively). No recombination model was used. We employed a (-28 μm , 42 μm) square simulation box with $\Delta x = 13.33 \text{ nm}$ cells and 25 (125) [particles per cell \(PPC\)](#) for gold (protons).

From the results of Ferri et al. [18], we would expect the constructive interference of the pulses in front of the target to enhance the electric fields on the back side of the target. This is exactly what we see in [Figure 4.7\(a, c\)](#) which is an electric field snapshot 800 fs into the simulation when sheath fields are clearly developed. Furthermore, the proton energy enhancement can be seen in [Figure 4.8\(a, c\)](#) in both the maximum energy and total amount of high energy (i.e. > 1 MeV) protons. This plot bins the protons by both angle (determined

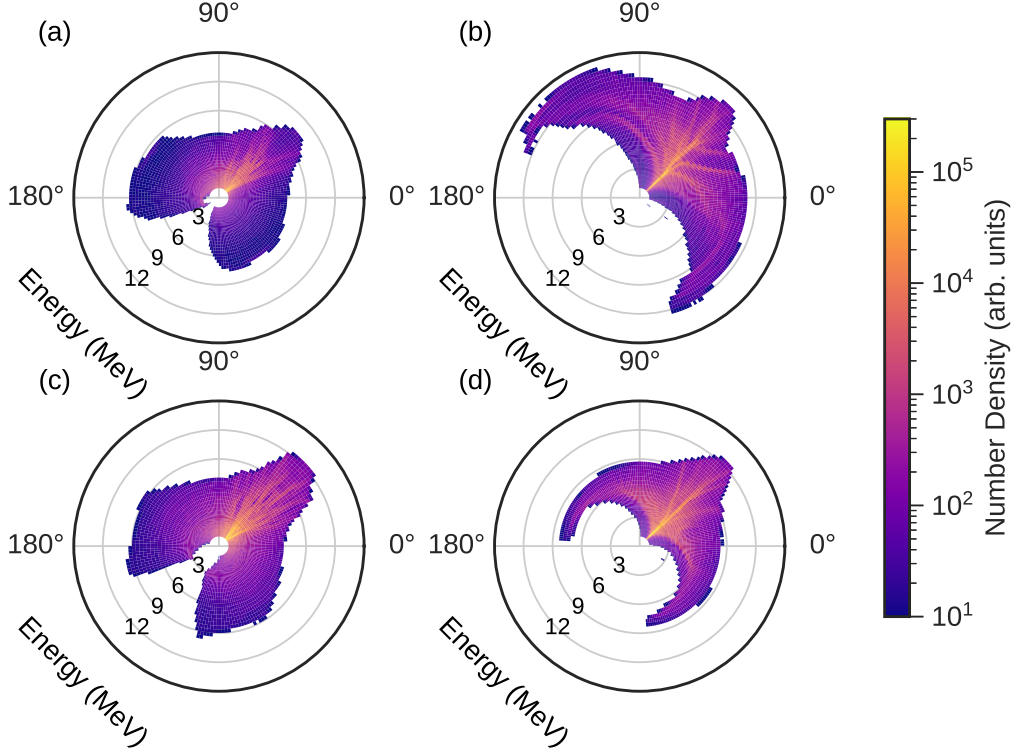


Figure 4.8: Proton distribution as a function of angle $\phi = \tan^{-1}(p_y, p_x)$ and energy at simulation time of 2100 fs for the (a) flat single 41° pulse, (b) expanded single 41° pulse, (c) flat double pulse, (d) expanded double pulse. Only protons with energy greater than 1 MeV are plotted.

from the protons' x and y momentum components) and energy.

Since the presence of a pre-plasma is known to greatly affect the proton energy spectrum, we performed two additional simulations where an exponential scale $L_s = 2 \mu\text{m}$ pre-plasma was placed in front of the target of the form:

$$n(r) = n_0^* \exp(-r/L_s) \quad (4.4)$$

where $n_0^* = 5.2 \times 10^{28} \text{ m}^{-3}$ is chosen to be lower than n_0 to preserve the same number of particles. The pre-plasma extends from $r_0 = 0$ (the target front) to $r_{\text{cut}} = 15.7 \mu\text{m}$ in front of the target. r_{cut} corresponds to the location where the gold density would be $n_c/50$ ¹⁴. Here, $n_c \approx 10^{27} \text{ m}^{-3}$ is the critical density (from [Equation 2.31](#)). This pre-plasma will form the critical density surface around $r = 8 \mu\text{m}$ in front of the target which can be seen in the

¹⁴This is an arbitrary cutoff which is chosen significantly below the critical density to ensure the laser travels for a significant distance through the pre-plasma. This cutoff was chosen as $n_c/18$ in Rahman et al. [90] and $n_c/100$ in Ferri et al. [18].

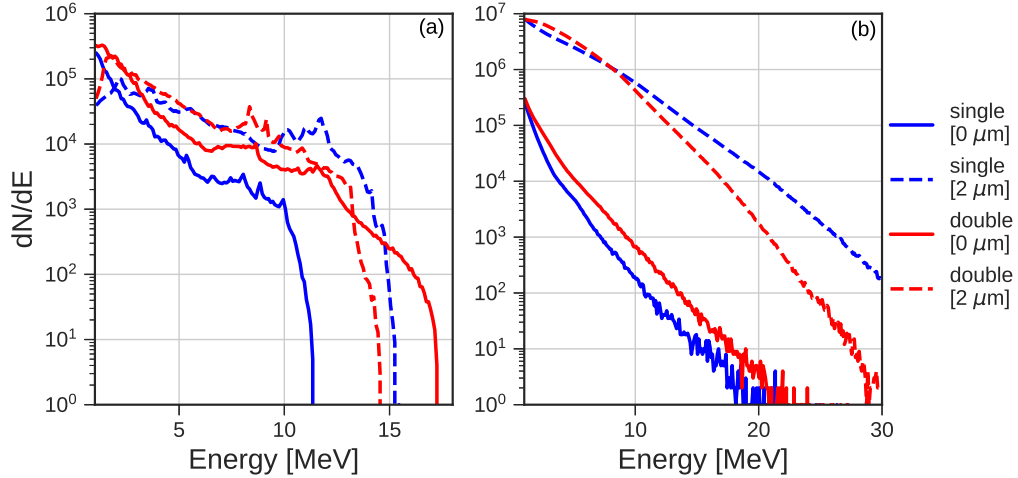


Figure 4.9: Spectrum at 2100 fs for (a) protons and (b) electrons. Particles that have left the simulation before 2100 fs are included in the spectrum from their energy at the time of crossing the boundary.

electric fields of Figure 4.7(b, d). From this figure, the electric field enhancement on the rear side of the target is not clear, but the proton energy distributions from Figure 4.8(b, d) show that the double pulse focuses the proton beam to a narrower angular spread and reduces filamentation¹⁵. Additionally, the number of protons along the target normal direction is higher in the double pulse case as can be seen from the brighter color.

To make these trends clear, the proton energy spectra at 2.1 ps were plotted in Figure 4.9 for each of the single and double pulses with and without the 2 μm pre-plasma. We can see (a) that the proton energy spectrum is enhanced for the double pulse without pre-plasma, but this is not so clear for the case with pre-plasma. Furthermore, the electron energy spectra (b) shows a clear enhancement in electron energy in the presence of pre-plasma.

Another useful metric is the overall conversion efficiency of laser energy into high energy ($> 1 \text{ MeV}$) electrons or protons which is shown in Figure 4.10. This is computed by dividing the energy in high energy protons or electrons by the total laser energy that entered the simulation at that point in time. Here, both the proton and electron energy enhancement can be seen, although, it bears mentioning that the enhancement is much smaller in the presence of a pre-plasma.

We also conducted some simulations with either half (32.5 J) or a quarter (16.3 J) of the total laser energy used previously. These maximum kinetic energy and conversion efficiency results for these simulations are also shown in Table 4.1 which exhibit similar trends to the higher energy simulations.

¹⁵ According to dictionary.com a filament is defined as *a very fine thread or threadlike structure*. So, filamentation refers to the threadlike nature of the proton beam (which is not desired).

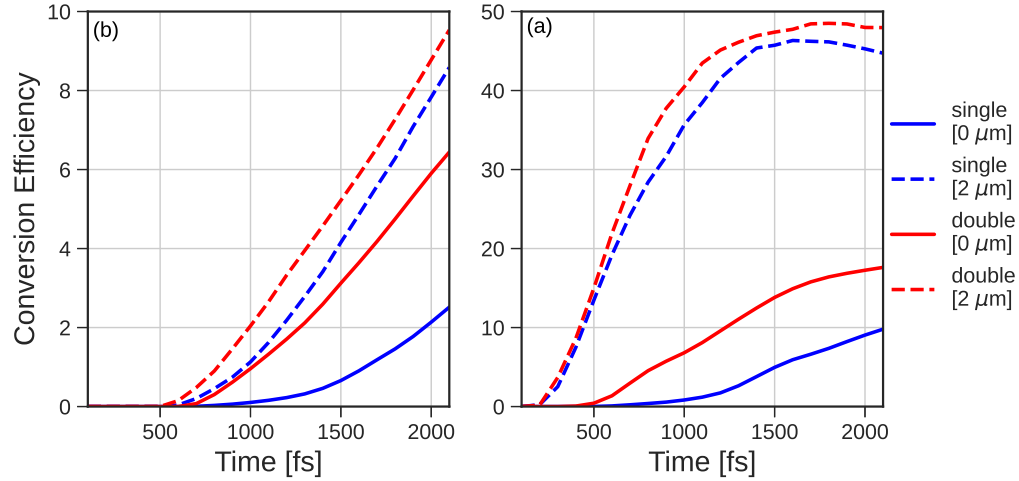


Figure 4.10: Conversion efficiency of laser energy into greater than 1 MeV (a) protons and (b) electrons.

Pulse	θ_i	I_0 [$\frac{W}{cm^2}$]	E_{laser} [J]	L_p [μm]	$KE_{p,max}$ [MeV]	η_p [%]	$KE_{e,max}$ [MeV]	η_e [%]
Single	20°	2×10^{19}	65	0	8.5	0.5	29.8	2.0
Single	41°	2×10^{19}	65	0	11.35	2.5	33.48	9.8
Double	$20^\circ, 41^\circ$	1×10^{19}	65	0	17.2	6.4	27.2	17.6
Single	41°	2×10^{19}	65	2	15.4	8.6	37.6	44.7
Double	$20^\circ, 41^\circ$	1×10^{19}	65	2	14.6	9.5	31.4	48.0
Single	41°	1×10^{19}	32.5	0	9.0	1.5	14.6	5.3
Double	$20^\circ, 41^\circ$	5×10^{18}	32.5	0	13.9	4.4	21.3	11.4
Single	41°	5×10^{18}	16.3	0	6.4	0.6	9.7	2.0
Double	$20^\circ, 41^\circ$	2.5×10^{18}	16.3	0	10.6	2.5	10.1	6.0

Table 4.1: Summary of Titan Simulations that varied the number of pulses, incidence angle (θ_i), intensity at peak focus (I_0), total laser energy (E_{laser}), and pre-plasma scale length (L_p). The maximum kinetic energy KE_{max} and conversion efficiency η are shown for both electrons (e) and protons (p). The top half of the table includes simulations with $E_{laser} = 65$ J which are used in the figures in this section. The bottom half of the table includes simulations with (otherwise identical) lower laser energy.

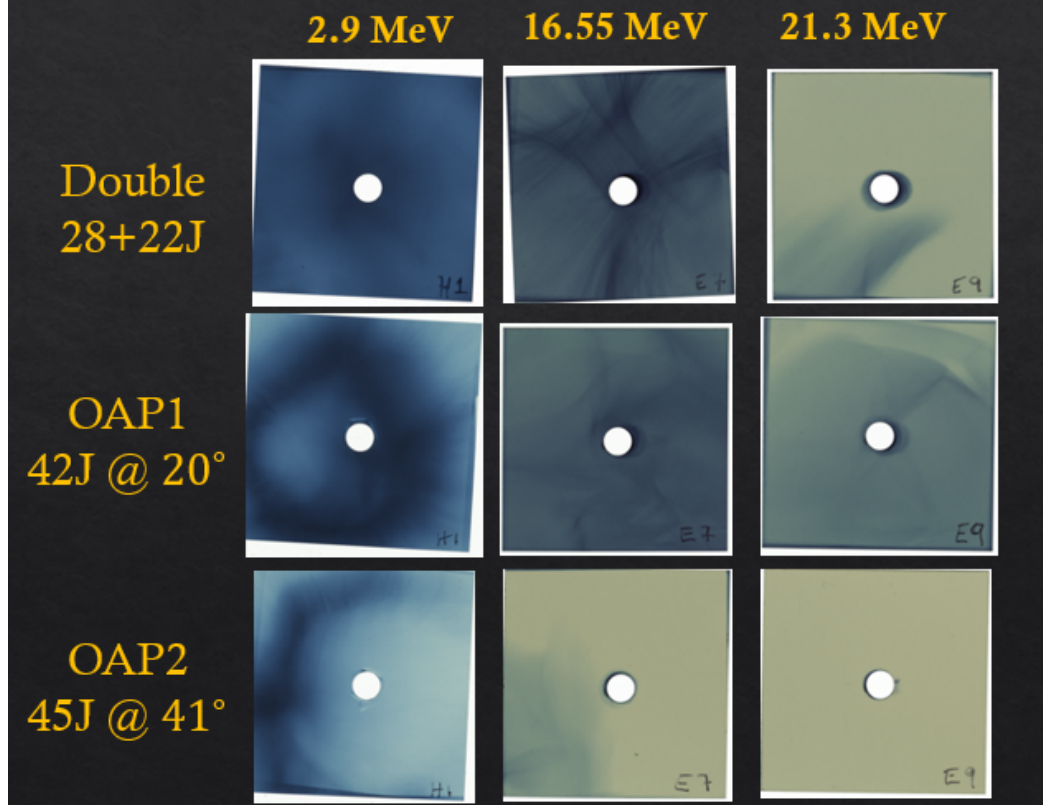


Figure 4.11: Three slices of radio-chromic film stacks that measure proton doses at 2.9, 16.55, and 21.3 MeV for 3 different pulse arrangements. A darker blue color indicates a higher proton dose at a given spatial location. For reference the stacks are 2×2 inch squares that are placed 18.6 cm behind the target.

4.2.2 Comparison to Experiment

The spatial distribution of the protons was recorded with [radio-chromic film \(RCF\)](#) which change color when exposed to certain types of radiation. By stacking the [RCF](#), the films can record a proton dose calibrated to higher energies for films further along in the stack. We can see these results in [Figure 4.11](#) which show spatial proton distributions for a selection of energies. Each row is a different shot with total energy at or slightly below 50 J. These images show that both the 20° and 41° single pulses have a proton distribution that is not centered in the target normal direction (which lies along the hole in the center). The 20° pulse records higher doses on the right side because that is where the laser axis of OAP1 points (similar for the 41°). The double pulse see protons that have a more even distribution throughout the entire [RCF](#) square that appears to have its highest dose right in the center.

In [Figure 4.11](#), I've focused on only three shots and three energies, but all of the shots for which the pulses had a nominal 50 J of energy is plotted in [Figure 4.12](#). The total dose

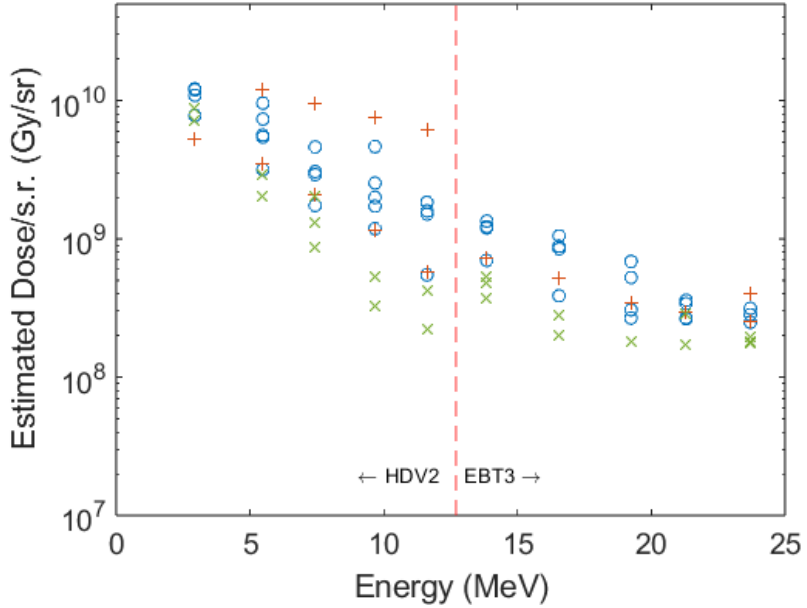


Figure 4.12: The radio-chromic film total estimated dose for all 50J shots. The blue circles indicate when both beams were used, while the orange + and green x markers indicate when beams 1 and 2 were used, respectively. These results are not calibrated, they are estimated from a calibration in Chris Willis' dissertation. This is why the y axis is estimated in units of Gy/sr. The implementation of sr allows for comparison of different size RCF stacks.

is plotted on the y-axis for each shot and for each energy that the RCF stacks are calibrated to. These show that the double pulse arrangement (blue circles) yields a higher dose in the higher energy stacks.

4.3 Discussion

In section 4.1, I reviewed the theoretical and experimental background behind the double pulse enhanced target normal sheath acceleration mechanism. This enhancement is largely due to two factors. First, the constructive interference of both pulses is capable of producing $\sqrt{2}$ times higher peak fields at the front of the target using the same total laser energy. The higher electric fields at the target front is directly related to both the hot electron generation and the maximum proton energy. Second, the symmetry of using two pulses at opposite incidence can help mitigate unwanted magnetic field deflections that help reduce filamentation and keep proton beams centered along the target normal direction.

Then, in section 4.2, I showed results of particle-in-cell simulations that show a clear enhancement in both the maximum proton energy and conversion efficiency of laser energy into high energy protons. When adding an exponential scale pre-plasma to the front of the tar-

get, these enhancements diminished. However, the double pulse simulations demonstrated a more focused proton beam along the target normal direction with reduced filamentation. On the experimental side, the double pulse showed a slightly higher total proton dose and comparable or slightly lower maximum proton energy than the single pulse case which is in agreement with the simulation results in the presence of a pre-plasma.

In conjunction, the results of experiment and simulations suggest that picosecond length lasers like Titan can demonstrate double pulse enhanced proton acceleration by both accelerating more protons and collimating the protons in the target normal direction. The maximum proton energy enhancement seems to be most pronounced for an undisturbed target with a sharp density profile which is supported by prior work from this group [90]. The experimental results most likely matched the simulation results with a pre-plasma due to an imperfect temporal pulse alignment. In the experiments when looking at results with different temporal timing¹⁶, the maximum proton energies were seen at both 0 and -2 picosecond delays. Since the experiment was only able to temporally resolve the timing of the pulses down to 2 picoseconds, this means that the temporal alignment may have been off on the order of a picosecond. As mentioned in section 4.1, this delay would cause pre-mature expansion of the target that may disturb the flat density profile needed for optimal target normal sheath acceleration.

While it may be difficult to time both pulses to arrive at the target within femtosecond resolution, the double pulse setup is still capable of increasing proton counts and reducing a proton beam's angular divergence. The double pulse setup can be extended to multiple pulses (like [93]) for a potentially even greater effect. The symmetry benefits of using multiple pulses at different angles has already been known for a long time as evidenced by the laser-fusion experiments at the National Ignition Facility and OMEGA. Since there is a significant amount of time and money that goes into upgrading existing laser facilities, the double (or multiple) pulse approach is a great tool for scientists to see enhanced proton/ion generation when constrained to a certain amount of laser energy from current technology.

¹⁶Not shown in this work ...

Chapter 5

MACHINE LEARNING METHODS APPLIED TO SYNTHETIC ION ACCELERATION DATA

In recent years, the application of [ML](#) methods to [HEDS](#) has exploded due to two main reasons. First, ultra-intense laser systems are now capable of firing many shots per second and collecting data at a similar rate. This allows scientists to collect a lot of data, which cannot reasonably be handled in real-time by a human. Second, machine learning frameworks like PyTorch [94] are easily accessible and powerful so that scientists who are not machine learning researchers are capable of using them.

One approach to applying machine learning with a limited amount of data is [BO](#). [BO](#), based on prior collected data points, attempts to find another suitable data point that is different than the prior data and expected to yield a more optimized output (according to some chosen criteria). Using [BO](#), Jalas et al. [95] optimizes the quality of a laser-accelerated electron beam and Dolier et al. [96] optimizes the maximum proton energy using [PIC](#) simulations. Another notable effort is Loughran et al. [97] who used this approach to demonstrate higher maximum cutoff proton energies from an experiment using a 1 Hz laser. While this approach is commendable, it does not scale well to laser repetition rates of 100 or more Hz.

Quite a few works have explored using neural networks to analyze and extract information from large datasets generated from [PIC](#) simulations. Djordevic et al. [98] used these simulations to find an empirical estimate for the effective acceleration time by using a [NN](#) model (which informs our choice of 1.3 in [Equation 5.20](#)). Schmitz et al. [99] also trained [NNs](#) on [PIC](#) simulation data to better understand optimal laser and target parameter combinations for their system at TU Darmstadt. One thing these studies have in common is that they only use data from [PIC](#) simulations which don't necessarily reflect real experiments (especially so because they are 1D and 2D simulations with reduced dimensionality).

The [Extreme Light Laboratory at the Wright-Patterson Air Force Base \(WP-ELL\)](#) has

a (1 kHz, $\tau_{\text{FWHM}} = 40$ fs, $\lambda = 0.8 \mu\text{m}$, $w_0 = 1.5 \mu\text{m}$) mJ class laser that can currently collect ion spectrometer data at a maximum rate of 100 Hz [24]. The laser irradiates a liquid target, formed from the intersection of two flowing liquid streams, that can be sustained for around 45 minutes before needing to be refilled. This acquisition rate and time could theoretically result in 270,000 unique data points during one collection. Laser systems like this are still new and the stability of the liquid target often interferes with the goal of collecting quality data. As a result, we first focused our energy into doing a [ML](#) analysis on data produced from a well-known model by Fuchs [79] based on parameters at [WP-ELL](#). The goal of this analysis is not to make recommendations on what input parameters should be used in experiment, but to provide a general framework that can be extended to real data and also to help others incorporate [ML](#) in their work by sharing our code (see Zenodo [100, 101] for the python code and datasets). By providing these files we hope to encourage others to compare other [ML](#) models against our results as a benchmark. This chapter details the work I did developing this synthetic dataset, comparing different [ML](#) algorithms, and evaluating their potential effectiveness in a real experiment.

5.1 Modified Fuchs et. al. Model

In this section, I will describe the model from which we generated the synthetic datasets [21, 23]. First, the expansion of a plasma into a vacuum [20] is used to determine the maximum proton energy and the number of accelerated protons per unit energy $\frac{dN}{dE}$. Following Fuchs [79], we define the acceleration time in proportion to the pulse duration of the laser and adopt a scaling (e.g. [Equation 2.34](#)) to relate hot electron temperature to the ponderomotive potential. This, in combination with other empirical estimates, allows calculating a proton energy spectrum from up to 7 parameters: main pulse intensity, contrast, wavelength, pulse duration, target thickness, target focal position, and laser spot size.

5.1.1 Plasma Expansion into a Vacuum

This model was developed by Mora [20] in 2003 who built off of earlier efforts [59, 60] in examining an isothermal expansion model. The model begins with the assumption that ions are contained in the semi-infinite interval $n_i = n_{i0}$ for $x < 0$ and no ions are initially in the vacuum region for $x > 0$. The electrons are distributed according to the boltzmann relation given by [Equation 2.21](#) where $n_{e0} = n_e(x = -\infty)$ is the electron density in the unperturbed plasma. Through this relation, $\phi(-\infty) = 0$. The initial electron density is related to the ion density $n_{e0} = Zn_{i0}$ where Z is the ion charge number for a fully ionized plasma. The potential also satisfies the Poisson equation [Equation 2.4](#) where $\rho/m = -e(n_e - Zn_i)$. The solution of [Equation 2.4](#) at $t = 0$ is found by integration [59] (where $E \equiv -\frac{d\phi}{dx}$) as

$$\frac{1}{2}\epsilon_0 E^2 = n_{e0} k_B T_e \begin{cases} \exp\left(\frac{e\phi}{k_B T_e} - 1 - \frac{e\phi}{k_B T_e}\right) & \text{if } x < 0 \\ \exp\left(\frac{e\phi}{k_B T_e}\right) & \text{if } x > 0 \end{cases} \quad (5.1)$$

From enforcing continuity of [Equation 5.1](#) at $x = 0$ (the location of the ion front initially) we determine $\phi = -k_B T_e / e$ to arrive at

$$E_{front,0} = \sqrt{\frac{2}{\exp(1)}} E_0 \quad (5.2)$$

where $E_0 \equiv \sqrt{n_{e0} k_B T_e / \epsilon_0}$. To get an estimate of the electric field at the ion front when $t > 0$ we need to consider what the characteristic time scale for ion motion is: the plasma ion frequency $\omega_{p,i}$

$$\omega_{p,i} \equiv \sqrt{\frac{Z n_{e0} e^2}{m_i \epsilon_0}} \quad (5.3)$$

which is analogous to [Equation 2.15](#). In relation to the time-scale of plasma ion oscillations, a long time would refer to $\omega_{p,i} t \gg 1$. The ion fluid sound speed c_s is given by

$$c_s = \sqrt{\frac{Z k_B T_e}{m_i}} \quad (5.4)$$

which is very similar to [Equation 2.16](#). Using the definition of the Debye length ([Equation 2.17](#)) and sound speed c_s we can re-express eq. (5.3) as

$$\omega_{p,i} t = \sqrt{\frac{Z k_B T_e}{m_i}} \sqrt{\frac{n_{e0} e^2}{\epsilon_0 k_B T_e}} t = (c_s t) (\lambda_{D0}) \quad (5.5)$$

where λ_{D0} is the initial Debye length and c_s is the ion sound speed. As we know from [chapter 2](#), when λ_D is smaller than the characteristic length scale of a system, the quasi-neutrality condition for a plasma is satisfied. In this case, the length scale would be $c_s t$ and we can show that asserting the condition $\omega_{p,i} t > 1$ is equivalent to $\lambda_D < c_s t$. We can continue by incorporating equations of continuity and the Lorentz force ([Equation 2.5](#)) which can be expressed as

$$\frac{\partial n_i}{\partial t} + v_i \frac{\partial n_i}{\partial x} = -n_i \frac{\partial v_i}{\partial x} \quad (5.6a)$$

$$\frac{\partial v_i}{\partial t} + v_i \frac{\partial v_i}{\partial x} = -\frac{Ze}{m_i} \frac{\partial V}{\partial x} \quad (5.6b)$$

This set of fluid equations can be solved numerically with the initial conditions for n_i , E , and $v_i = 0$, but it is more instructive to consider a *self-similar solution* that describes the

ions moving with speed

$$v_i = c_s + x/t \quad (5.7)$$

for $x + c_s t > 0$. It is self-similar in the sense that the specific length and time scales are not important, only their ratio x/t . In this self-similar region, quasi-neutrality is maintained and the expanding electron density can be expressed as

$$n_e = Zn_i = n_{e0} \exp\left(-\frac{x}{c_s t} - 1\right) \quad (5.8)$$

By combining eqs. (5.6a), (5.6b), (5.7) and (5.8), we can arrive at a solution for the self-similar electric field in this quasi-neutral region

$$E_{SS} = \frac{m_i c_s}{Zet} = \frac{k_B T_e}{ec_s t} = \frac{E_0}{\omega_{p,i} t} \quad (5.9)$$

Physically, we can interpret this as a sheet of positive charge $\sigma = \epsilon_0 E_{SS}$ at $x = -c_s t$ and a sheet of negative charge $-\sigma$ at the plasma edge. The location of this plasma edge (i.e. the location of the ion front) can be roughly obtained by equating the local Debye length $\lambda_D = \lambda_{D0} \sqrt{n_{e0}/n_e}$ to the scale length $c_s t$.

$$x_{i,front} = c_s t [2 \ln(\omega_{p,i} t) - 1] \quad (5.10)$$

and the ion velocity at the front can also be obtained

$$v_{i,front} = 2c_s \ln(\omega_{p,i} t) \quad (5.11)$$

The ion velocity can be plug back into [Equation 5.6b](#) to find out that $E_{front,SS} = 2E_{SS}$. Mora found an approximate solution to E_{front} that matches $E_{front,0}$ and $E_{front,SS}$ in their respective cases ($t = 0$ and $\omega_{p,i} t \gg 1$) as

$$E_{front} \simeq \frac{2E_0}{\sqrt{2 \exp(1) + (\omega_{p,i} t)^2}} \quad (5.12)$$

This formula not only reaches the correct values in the limiting cases, but also effectively interpolates in the intermediary regions (i.e. $\omega_{p,i} t \sim 1$) when compared to a numerical code that solves eqs. (5.6a) and (5.6b) without assuming a self-similar solution. In [5.1a](#), we see the net charge density at some time $\omega_{p,i} t = 50$ after the start of a 1D plasma expansion simulation. We can identify the -2σ with the fastest expanding electrons and the $+\sigma$ region next to it as the positive ions getting pulled along. In [5.1b](#), we can see the electric field between these two charged regions peaks $\simeq 2E_{ss}$. Then, using this formula with [Equation 5.6b](#), we can determine the ion front velocity as

$$v_{i,front} = 2c_s \ln(\tau + \sqrt{\tau^2 + 1}) \quad (5.13)$$

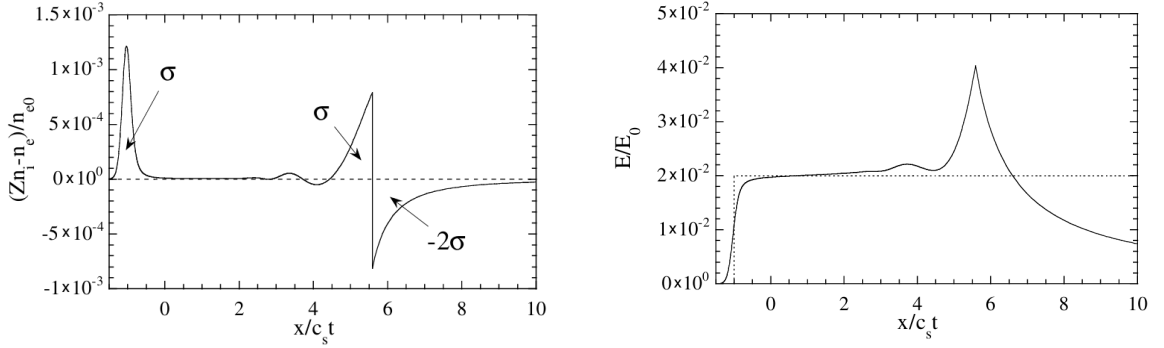


Figure 5.1: The net charge density (left) as a function of position $x/c_s t$ and normalized electric field E/E_0 (right) for $\omega_{pi}t = 50$ taken from Fig 1 and 2 in Mora's Paper [20]. On the right, the self-similar electric field from Equation 5.9 is plotted with a dashed line.

where we've defined a normalized acceleration time $\tau \equiv \omega_{p,i}t/\sqrt{2\exp(1)}$. Additionally, in the limit $\omega_{p,i}t \gg 1$, Equation 5.10 becomes

$$x_{i,front} \simeq c_s t [2 \ln(\omega_{p,i}t) + \ln(2) - 3] \quad (5.14)$$

The per-ion kinetic energy can now be calculated as

$$\begin{aligned} \mathcal{E} &\equiv \frac{1}{2} m_i v_{i,front}^2 = 2m_i c_s^2 \ln(\tau + \sqrt{\tau^2 + 1})^2 \\ &= 2Zk_B T_e \ln(\tau + \sqrt{\tau^2 + 1})^2 \end{aligned} \quad (5.15)$$

Using Equation 5.8, we can determine the number of accelerated ions between $x = -c_s t$ and $x = x$ as

$$N_i \equiv \int_{-c_s t}^x n_i(x') dx' = n_{i0} c_s t [1 - \exp(-\frac{x}{c_s t} - 1)] \quad (5.16)$$

and using Equation 5.7, we can show that this is equivalent to

$$N_i(x) = n_{i0} c_s t [1 - \exp(-\sqrt{\frac{2\mathcal{E}}{\mathcal{E}_0}})] \quad (5.17)$$

where $\mathcal{E}_0 \equiv Zk_B T_e$. Now that the number of ions is expressed in terms of the energy \mathcal{E} , we can determine the number of accelerated ions per unit energy (per unit surface) as

$$\frac{dN}{d\mathcal{E}} = \frac{n_{i0} c_s t}{\sqrt{2\mathcal{E}\mathcal{E}_0}} \exp(-\sqrt{\frac{2\mathcal{E}}{\mathcal{E}_0}}) \quad (5.18)$$

5.1.2 Modified Fuchs Model

When $\tau \rightarrow \infty$, eq. (5.15) diverges to ∞ . This is an inherent limitation of the isothermal fluid model, and different models are able to avoid this issue [66, 102, 103]. However, a simple fix to this model involves assuming that this acceleration time is finite and proportional to the pulse duration. Physically, it makes sense that the protons are only getting accelerated on the timescale of laser-target interactions. This is the approach taken by Fuchs [79] and he expresses Equation 5.15 as

$$E_{\max} = 2k_B T_h [\ln(t_p + \sqrt{t_p^2 + 1})]^2 \quad (5.19)$$

where $t_p \equiv \omega_{p,i} t_{\text{acc}} / \sqrt{2 \exp(1)}$ just like the Mora model. We've also set $Z = 1$ to signify that we are looking for hydrogen ions (i.e. protons). The crucial difference is that we express the acceleration time as

$$t_{\text{acc}} \approx 1.3 \tau_{\text{FWHM}} \quad (5.20)$$

One can assume that the absorption fraction of hot electrons η (with respect to the total laser energy E_L) is given by $\eta_e = 1.2 \times 10^{-15} I^{0.74}$ W cm⁻² with a maximum of 0.5, determined from empirical scalings (e.g. see fig. 3 from Key [104]). Additionally, the average energy of the hot electrons is set by the Wilks scaling (Equation 2.34). Putting this together,

$$N_e = \eta_e \frac{E_L}{T_h} \quad (5.21)$$

would be the total number of hot electrons accelerated into the target. These electrons spread out in a roughly cylindrical volume of area S_{sheath} and length $c\tau_{\text{FWHM}}$ where the circular sheath cross section can be estimated by $S_{\text{sheath}} = \pi(r_0 + d \tan(\theta))^2$. Here, $r_0 = w(x) \frac{\sqrt{2 \ln(2)}}{2}$ is the (spatial) half width at half maximum of the intensity distribution at position x . The effective radius of the sheath has an additional factor of $d \tan(\theta)$ where d is the initial target thickness and θ is the half-angle divergence of the hot electrons within the target (taken as $\theta = 25^\circ$). As a result, the hot electron number density can be expressed as

$$n_{e0} = \frac{N_e}{c\tau_{\text{FWHM}} S_{\text{sheath}}} \quad (5.22)$$

With an estimate of the hot electron density, the proton spectrum can now be computed from eq. (5.18) as

$$\frac{dN}{dE} = N_0 \frac{\exp(-\sqrt{2E/k_B T_h})}{\sqrt{2E k_B T_h}} \quad (5.23)$$

where $N_0 \equiv n_{e0} c_s t_{\text{acc}} S_{\text{sheath}}$ is defined for convenience. Using a dimensionless scale for energy $\varepsilon \equiv \sqrt{2E/k_B T_h}$, we can calculate the number of protons and total energy in protons

through integrating [Equation 5.23](#)

$$N = N_0(\exp(-\varepsilon_{\min}) - \exp(-\varepsilon_{\max})) \quad (5.24)$$

$$E_{\text{tot}} = N_0 \frac{k_B T_h}{2} [\exp(-\varepsilon_{\min})(2 + \varepsilon_{\min}(2 + \varepsilon_{\min})) - \exp(-\varepsilon_{\max})(2 + \varepsilon_{\max}(2 + \varepsilon_{\max}))] \quad (5.25)$$

where $\varepsilon_{\min} = \sqrt{2E_{\min}/k_B T_h}$ defines a minimum energy cutoff (ε_{\max} is analogous and chosen by [Equation 5.19](#)). Furthermore, we can calculate the average proton energy by dividing [Equation 5.24](#) from [Equation 5.25](#)

$$E_{\text{avg}} \equiv \frac{E_{\text{tot}}}{N} \quad (5.26)$$

The combination of Equations 5.19 and 5.23 have been tested across many of the early **TNSA** experiments of the early 2000s for a wide range of laser intensities and pulse durations with good accuracy (see fig. 4 from Fuchs [79]).

5.1.3 Further Model Modifications

When restricted to a particular laser system, the wavelength, pulse duration, and spot size are fixed. Considering the model in [subsection 5.1.2](#), only three adjustable parameters would be of interest – target thickness d , peak intensity I_0 and target focal position x . To introduce complexity into our model, we wanted to consider the effect that a pre-expanded target would have on the proton acceleration. The pre-expansion may enhance the hot electron generation, but expansion on the rear side of the target would reduce the effectiveness of the **TNSA** process. We incorporate this effect by allowing the laser to have a finite contrast κ which relates the intensity of the main laser pulse I_0 to the intensity of a secondary laser pre pulse as $I_{\text{pre}} = \kappa I_0$. This pre-pulse is treated as a spike in intensity that occurs t_0 before the arrival of the main pulse. The pre-expanded target would have a new effective thickness given by

$$d_{\text{eff}} = d + 2c_s t_0 \quad (5.27)$$

where c_s is the ion sound speed from eq. (5.4) in which the target is expanding outwards from both sides. Here T_e is the temperature due to the pre-pulse and can be calculated by assuming that $T_e \propto I$ and that an intensity of $10^{12} \text{ W cm}^{-2}$ produces electron temperatures of $T_{\text{pre},0} = 50 \text{ eV}$. Since n_e decreases as d gets larger and $\omega_{p,i} \propto \sqrt{n_e}$, [Equation 5.19](#) is inversely proportional to the target thickness. So, a larger prepulse with a longer time to expand t_0 will see a higher effective target thickness. Furthermore, when the target is off focus, the effective pre-pulse intensity on target is less which results in less expansion.

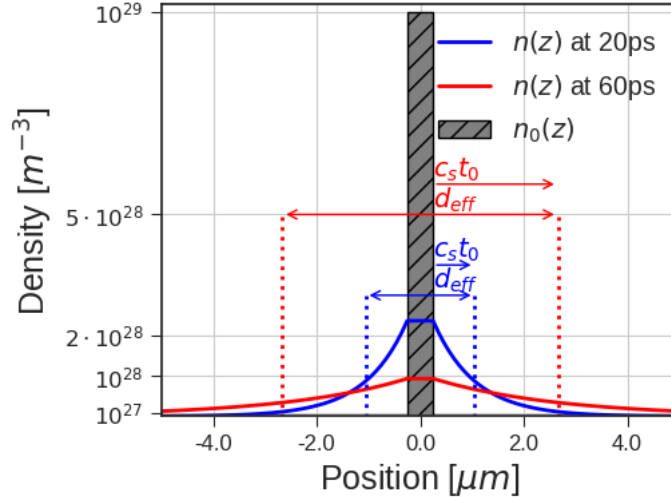


Figure 5.2: The electron density profile of the pre-expanded target is depicted for various times t_0 . In this figure, $n(0) \equiv n_{\max}$. Taken from Desai et al. [21] where z was used as the distance along the laser axis instead of x as done in this work.

In addition, some of the main pulse energy can be depleted by traveling through the underdense region of this new pre-expanded target. These effects will be referred to as *pump depletion* and are inspired by arguments from Decker [105]. Decker describes pump depletion as an *etching* process where traveling through the plasma causes wavefront edge to recede at a speed given by the *etching velocity*

$$v_{\text{etch}} = (\omega_{p,e}/\omega)^2 c \quad (5.28)$$

Note that this speed continuously changes throughout the exponential-scale electron density which falls off like $n \sim \exp(-x/c_s t_0)$ on both sides of the target (see Figure 5.2 for a visual). Due to conservation of particle number, if the target expands, the maximum density n_{\max} will also lower and is given by $n_{\max} = \frac{n_{\max} d}{d_{\text{eff}}}$. We can integrate v_{etch} with respect to time, but it is more convenient in terms of the position since we know the range over which the under-dense plasma exists. The plasma edge x_f is given by Equation 5.14 and we will integrate up to the location of the critical density $x_0 = c_s t_0 (\ln(n_{\max}) - \ln(n_c))$. Utilizing the change of variables $dx = c dt$ (due to the pulse traveling at the speed of light c), the “etching distance” can be calculated as [21]

$$L_{\text{etch}} \equiv \int_{x_0}^{x_f} v_{\text{etch}} \frac{1}{c} dx = \frac{e^2 n_{\max} c_s t_0}{\epsilon_0 m_e \omega^2} \left(\exp\left(-\frac{x_0}{c_s t_0}\right) - \exp\left(-\frac{x_f}{c_s t_0}\right) \right) \quad (5.29)$$

Finally, this etching reduces the effective pulse duration by

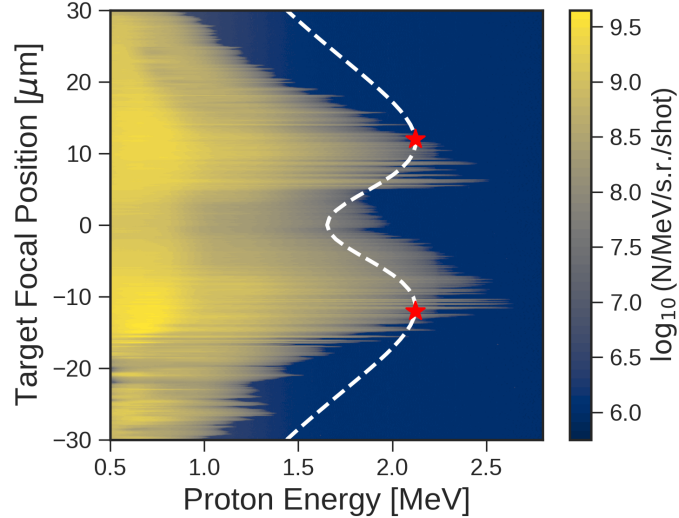


Figure 5.3: The dotted black line shows the maximum proton energy predicted by [Equation 5.19](#) with the pump depletion considerations in [subsection 5.1.3](#) assuming $t_0 = 60$ ps, $I_0 = 10^{19}$ W cm $^{-2}$, $\kappa = 10^{-7}$, $d = 0.5$ μ m. The red stars indicate the predicted positions of maximum proton energy ~ 12 μ m. This plot is overlayed on top of an experimental maximum proton energy distribution from Morrison et. al. [\[22\]](#). This figure is taken from Desai et. al. [\[21\]](#).

$$\tau_{\text{fwhm,eff}} = \tau_{\text{fwhm}} \left(1 - \frac{L_{\text{etch}}}{c\tau_{\text{fwhm}}}\right) \quad (5.30)$$

This model, however, is not without its flaws. First, our calculations assume a critical density of a tenth of the amount of the actual critical density. Second, instead of defining $d_{\text{eff}} = d_0 + 2x_0$ (which would be the true effective density that remains above critical density), we substitute it with [Equation 5.27](#). Third, we modify the multiplier seen in [Equation 5.20](#) from 1.3 to 25 which is a significant departure. Finally, the proportionality $T_e \propto I$ with $T_{\text{pre},0} = 50$ eV is chosen arbitrarily. Despite these drawbacks, we obtain model predictions similar to what is seen in [Figure 5.3](#) to account for the maximum proton energy dip at peak focus. The goal of creating this model modification is to add complexity to the underlying physics for the purposes of evaluating the effectiveness of machine learning models, not to invent new physics.

5.2 First Analysis

In this section, the results from my publication in *Contributions to Plasma Physics* [\[23\]](#) in November of 2024 will be discussed. This project started with the work of Joe Smith and Ricky Oropeza who first coded up the modified Fuchs et al. model in Python. Then,

undergraduate student Tom Zhang did some preliminary work in exploring different [ML](#) frameworks to see what models could fit the data the best with some contributions from another undergraduate student Pedro Gaxiola at [California State University - Channel Islands \(CSUCI\)](#). I initially worked in a complementary fashion to Tom, but finished up the project after Tom graduated from OSU with some help from undergraduate student Jack Felice. Along the way we were supported by coauthors Alona Kryshchenko from [CSUCI](#) in addition to Anil Patnaik and Michael Dexter from [Air Force Institute of Technology \(AFIT\)](#). This work was modeled on the [WP-ELL](#) laser system described in et al. [24] with laser parameters mentioned in the beginning of [chapter 5](#).

5.2.1 Methods

In this work, we explored a 25,000 point dataset based on the model described in [subsection 5.1.2](#) which had three output quantities: E_{\max} , E_{tot} , E_{avg} ([Equations 5.19, 5.25 5.26](#)). We modified the acceleration time (in [Equation 5.20](#)) from 1.3 to 4 to better match the points in our dataset which is still within the range that Djordevic et al. [98] recommended. Three input quantities were varied: peak laser intensity I_0 (from 10^{18}W cm^{-2} to 10^{19}W cm^{-2}), target thickness d (from $0.5\mu\text{m}$ to $10\mu\text{m}$), and distance from peak focus to the target x (from $-30\mu\text{m}$ to $30\mu\text{m}$). The input quantities were randomly chosen (uniformly within their intervals) with the Fuchs et al. model evaluations yielding the three outputs. To make the problem non-trivial, noise was added to the outputs sampled from a log-normal distribution with a mean of the output value and standard deviation between 0 and 30% of the output value. Varying the noise, which would be present in an experimental dataset, will show how well a model can handle noise. Since we define the standard deviation as proportional to the mean (rather than some constant), the raw amount of noise becomes larger as the predictions get larger.

As a pre-processing step, we first applied a logarithm to both the intensity and three outputs of the model. This was necessary due to our choice of sampling the intensity uniformly with respect to the exponent (i.e. 18-19) and the output energies are directly proportional to the intensity. Additionally, we applied z-score normalization to both the inputs and outputs which is standard in machine learning algorithms to keep all data points on the same order of magnitude. From the 25,000 total points, we used 20,000 for training and reserved a hold-out set of 5,000 for testing. We determined the scalings from the training set only to ensure there is no leakage of information into the testing set. Furthermore, we multiplied the unscaled outputs by a correction factor equal to the mean of the training outputs divided by the unscaled outputs to reduce and under-predicting bias introduced by the log-scaling of the outputs [106].

We used three different [ML](#) models in our study: [SVR](#), [GPR](#), [NN](#) that were programmed using RAPIDS [107], GPyTorch [108], and Skorch [109] respectively in Python. These pack-

NN	BS = 256, leaky ReLU, $N_h = 3$, $N_l = 64$, Adam, LR = 0.001
SVR	$\epsilon = 0.01$, $C = 2.5$, tolerance = 0.001
GPR	Iterations = 30, LR = 0.001

Table 5.1: Optimal hyperparameters found through grid searches and cross-validation using only the training set for the results in section 5.2.

ages all contain functions to facilitate running **graphics processing unit (GPU)** accelerated scripts and were ran using the Pitzer cluster on the **Ohio Supercomputer Center (OSC)**. All three approaches benefitted from hyperparameter optimization through the `GridSearchCV` module of scikit-learn. These choices are summarized in Table 5.1. For both the **GPR** and **SVR**, an **RBF** kernel was used.

5.2.2 Results

Our first task was to evaluate how well the trained models can fit the underlying dataset as the number of data points is increased. We accomplished this by evaluating the models on a testing set which is proportional to the amount of training points in a 80-20 training-testing split. In Figure 5.4, the **MAPE** is evaluated between the model outputs and the testing data outputs to assess the accuracy of each method for three different noise levels – 0, 15, and 30 %. Since, in this figure, the testing data contains noise, it is impossible to achieve 0 % error. As a result, we've included a black line to show the error between the testing data and the theoretical value predicted by the Fuchs et al. model. We can clearly see that the all the **ML** models don't appear to get better when we increase the number of data points. Additionally, we can see that the **NN** model has the worst accuracy and more variability.

Then, we kept the number of data points fixed at 2,000 and varied the noise level from 0 to 30% to make a similar analysis in Figure 5.5. These plots show how the **NN** model doesn't do well without any added noise. In addition to the noisy test data (solid line), the error on the same data without noise was also plotted as a dashed line. One interesting feature about this plot is that the **NN** model's error does not increase significantly as the noise level increases.

Next, we compared the execution time of the different **ML** models and found that the **SVR** runs the fastest, the **GPR** runs the slowest, and the **NN** runs at a speed somewhere in between. The **GPR** scales roughly as $\mathcal{O}(N^3)$ [110] which can be contrasted with the **NNs** $\mathcal{O}(N)$. In terms of GPU memory utilized, the **GPR** used 14 GB, whereas the **SVR** and **NN** used between 1 and 2 GB. Due to the unfavorable $\mathcal{O}(N^2)$ memory scaling of the **GPR** [110], larger datasets than 40,000 points were practically infeasible with our implementation.

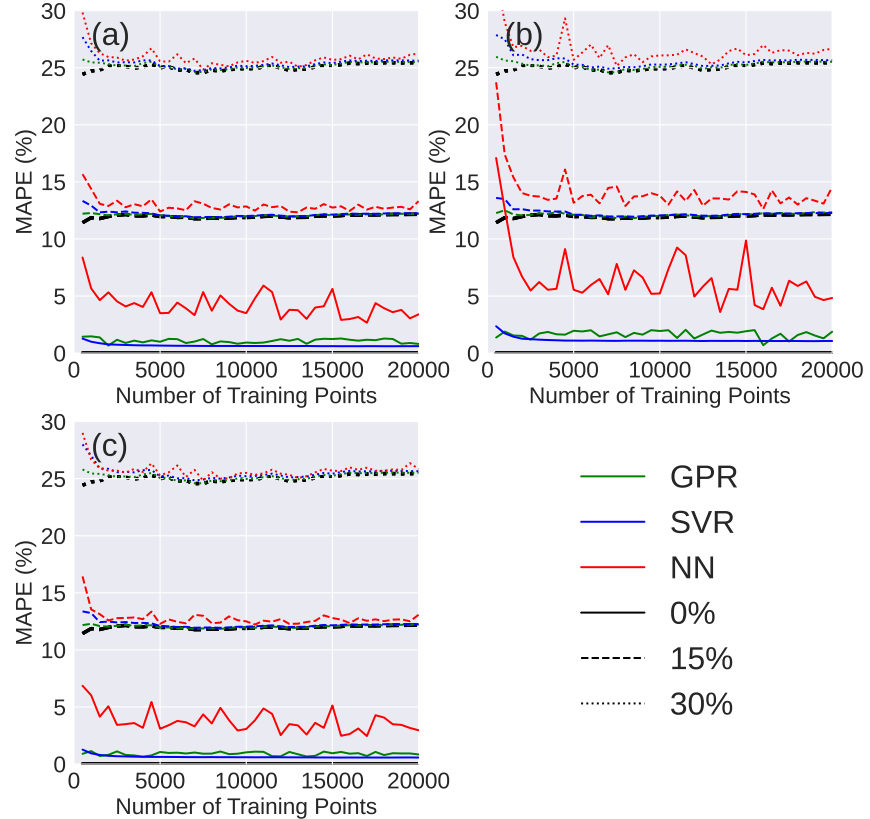


Figure 5.4: MAPE versus number of training points from ML model predictions for (a) max proton energy, (b) total proton energy, (c) average proton energy and noisy testing data. Each panel shows results from (solid) 0%, (dashed) 15% and (dotted) 30% added noise in the data. Black lines with different line types indicate the MAPE between the noisy and noiseless data. Because we only compare ML models to noisy data in this figure, these black lines indicate the best that any ML model could conceivably do. Figure and caption taken from Figure 3 of Desai et al. [23].

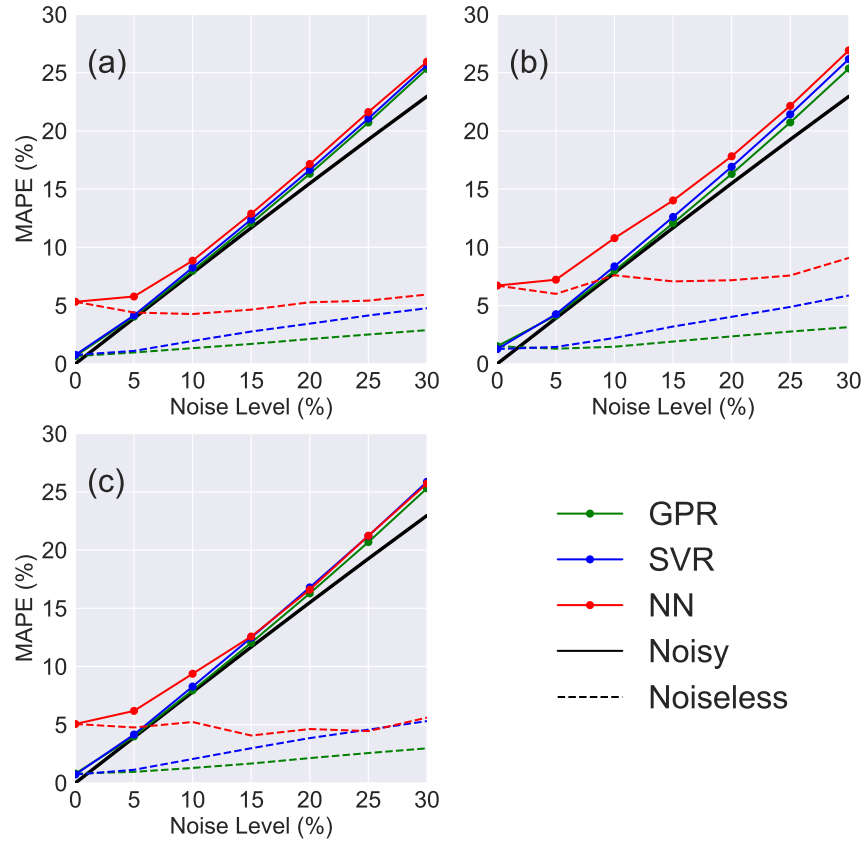


Figure 5.5: Solid lines show the typical MAPE in (a) maximum proton energy, (b) total proton energy, and (c) average proton energy when the models (which were trained on 2000 synthetic data points with noise) are evaluated on data with different levels of noise. Dashed lines show the typical error when those same ML models are evaluated on noiseless test data. Black solid lines indicate the MAPE between the noisy and noiseless data. Figure and caption taken from Figure 4 of Desai et al. [23].

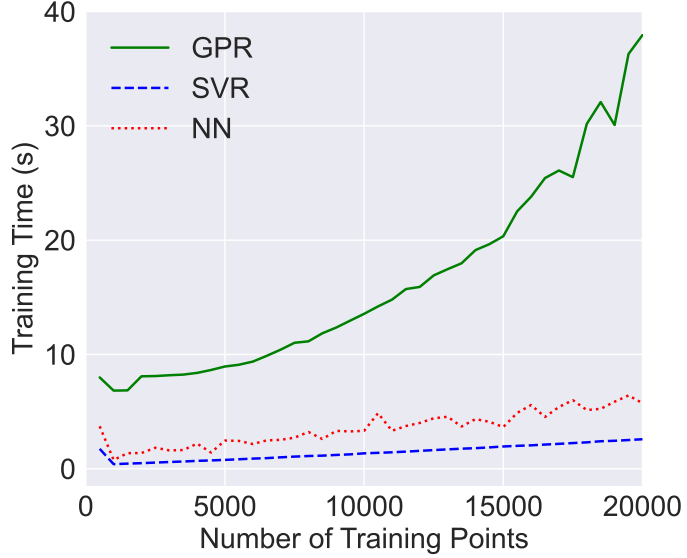


Figure 5.6: The execution time of the different ML models averaged across noise levels in computing the maximum, total, and average proton energies. Figure and caption taken from Figure 5 of Desai et al. [23].

5.2.3 Optimization Task

We highlighted a useful application of these models by determining a set of inputs that would produce a proton energy spectrum up to a specified maximum energy with a relatively high number of protons in that range as well. We characterize the balance of these two quantities, the maximum cutoff energy KE_c (E_{\max}) and the laser to proton conversion efficiency η_p ($E_{\text{tot}}/E_{\text{laser}}$), as

$$f(KE_c, \eta_p) = \frac{|KE_c - KE_{c,\text{goal}}|}{KE_{c,\text{goal}}} + \frac{C}{\eta_p} + g(KE_c, KE_{c,\text{goal}}) \quad (5.31)$$

where C is a parameter that can influence the strength of η_p relative to KE_c . These features can be seen in Figure 5.7 where three different energy cutoffs were chosen to optimize towards: 1, 0.5, and 0.25 MeV. The green region focuses on regions of the parameter space that closely match the given cutoff, while the blue region additionally factors in η_p . For practical reasons, we impose a penalty term $g(KE_c, KE_{c,\text{goal}})$ that prevents choosing points that have KE_c more than 15% away from the specified cutoff. These plots are generated from the Fuchs et al. model with 0 added noise, so they should be regarded as the ideal results that can be compared with the ML models.

We generated the same plots¹⁷ as Figure 5.7 with trained ML models on 2,000 training data points with 30% added noise which can be seen in Figure 5.8. These results show the

¹⁷These plots are colloquially referred to as *banana* plots in my research group due to their shape.

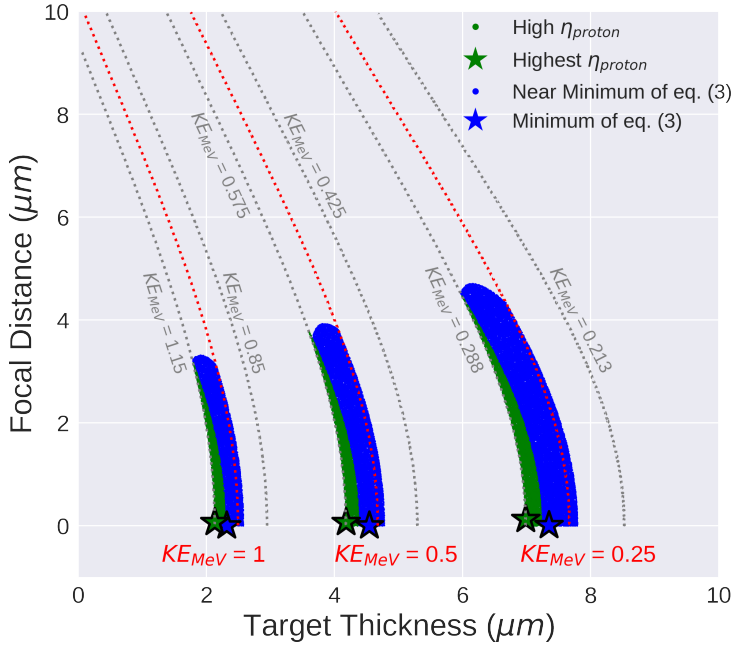


Figure 5.7: Parameters that produce maximum proton energy cutoffs in three different desired ranges: 1.0 MeV, 0.5 MeV and 0.25 MeV. Combinations of thickness and focal distance that produce these energy cutoffs (irrespective of the laser to proton conversion efficiency) are shown with dotted red lines. With each red line we also show with dotted gray lines the thicknesses and focal distances that produce proton energy cutoffs that are +15% or -15% of the cutoff goal. Green shaded areas show regions where the laser to proton conversion efficiency is high (i.e. within 5% of the optimal value). A green star shows the ideal conditions for maximizing the proton conversion efficiency. The blue region corresponds to using all the terms in [Equation 5.31](#) and the blue star indicates the ideal conditions according to that minimization scheme. Figure and caption taken from Figure 6 of Desai et al. [23].

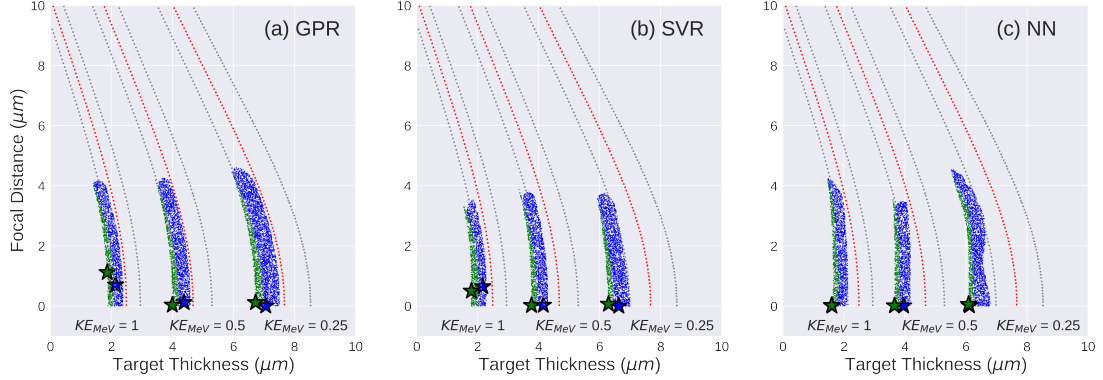


Figure 5.8: Parameters that produce maximum proton energy cutoffs according to three trained ML Models on 2,000 data points with 30% added noise: (a) GPR, (b) SVR, (c) NN compared against the red and gray lines plotted in Figure 5.7. The green and blue shaded regions are scatter plots of a subset of evaluated points that fall within 5% of the model's predicted optimum according to the same criteria in Figure 5.7. Figure and caption taken from Figure 7 of Desai et al. [23].

GPR closely matching Figure 5.7 and the SVR performing similarly well. Meanwhile, the NN's predicted point often fall outside the 15% cutoff boundary, which is not surprising due to its lower accuracy from the preceding analysis in Figure 5.5.

5.3 Second Analysis

In this section, my work from section 5.2 was expanded upon and written into a manuscript that is currently under consideration at *APL Machine Learning*. This work was originally assigned to (then) undergraduate student Jack Felice as a similar, but complementary project to what I primarily worked on. Jack did the bulk of the work in this project and borrowed help from me as needed. When Jack left for graduate school at the University of Maryland, I spent a few months organizing his work, contributing to the text of the paper, and creating polished figures. The co-authors from this work are largely the same as the previous work, but additionally include fellow graduate student Nathaniel Tamminga for his discussion on the constrained data campaign. This work was also modeled on the [WP-ELL](#) laser system.

5.3.1 Methods

In section 5.2, we tried to address training a model on only 20,000 data points. Furthermore, this model was relatively simple – a regression algorithm could fit the model quite accurately with only a few thousand points. Also, we found that the NN model performed poorly due to lack of model complexity and too few data points. A real experimental dataset would be

much more complex and thus require more data to understand its underlying trends. As a result, our second project added complexity in the form of pre-expansion of the target explained in subsection 5.1.3.

From this new modified model, we generated a training dataset of 1,525,000 points by sampling from a uniform grid of points in a 4D parameter space. The three inputs from section 5.2 are the same (except we reduced the maximum of the target thickness to $5\text{ }\mu\text{m}$). This grid included thicknesses in steps of $0.5\text{ }\mu\text{m}$, focal positions in steps of $1\text{ }\mu\text{m}$ and intensities in steps of $1.8 \times 10^{17}\text{ W cm}^{-2}$. The relevant quantity to control the extent of the pre-plasma is the contrast κ which was varied in steps of 1.8×10^{-8} . In Figure 5.2, the effect of the prepulse can be seen modifying the density profile of the target ($t_0 = 60$ ps was used in this work). The 250,000 point testing dataset was generated from the same intervals as the training set, but without noise and on a grid of points (instead of random sampling throughout the interval).

We used the same outputs as before: E_{\max} , E_{tot} , and E_{avg} . Since the new contrast parameter can make the proton energies get arbitrarily low, we set a floor to these outputs energies of 1 keV, 1 nJ, and 1 keV respectively. This was motivated by the finite energy resolution of ion energy detectors and preventing the MAPE metric from getting a division by zero error. Additionally, the acceleration time multiplier (see Equation 5.20) was increased to 25 to balance out the lower predicted proton energies from the new physics model’s larger effective thickness (Equation 5.27). The features of this new model can be seen in Figure 5.2 which highlight the characteristic *dip* in the proton energy at peak focus obtained from Morrison et al. [22].

We used a NN model like the previous work in section 5.2, but modified the other two models. The SVR was not able to handle more than a few hundred thousand data points and for this reason, it was not used. Instead, we used the more elementary polynomial regression (POLY) due to its simplicity which can be used as a baseline model without GPU accelerated computations. The POLY model could fit the data in section 5.2 accurately, but it does not work well with the added complexity in the new model (which will be seen later). Then, we replaced the exact GPR with the stochastic variational gaussian process (SVGP) (see [111]) which assumes a variational distribution over some amount of inducing points, restricting the training data to a representative subset. This allows the SVGP to be trained on data sets of order one million points in mini-batches just like the NN. Like before, we summarize the hyperparameters in Table 5.2 (and the architecture can be visualized in Figure 3.4). Finally, we replaced the standard z-score normalization with min-max scaling – a linear scaling that scales the minimum value of a particular data column to be 0 and the maximum value to be 1. Min-max scaling was chosen to better represent the nature of parameter selection: uniform sampling between some minimum and maximum value.

Model	Parameters	RMSE	Time (min)
POLY	deg=7, $\alpha = 10^{-3}$	0.033	0.883
SVGP	IP=2000, LF=8, LR= 10^{-2}	0.018	34.66
NN	BS= 2^{13} , $\gamma = 0.90$, P=10 LR= 10^{-2} , 12x64	0.013	4.93

Table 5.2: Optimal hyper-parameters including the root mean square error (RMSE) and mean fit time, determined from a grid search of hyperparameters for the NN, POLY, and SVGP. For the NN, the batch size (BS), learning rate decay (γ), patience (P), learning rate (LR), and architectures (layers x neurons per layer) were changed throughout the scans. For the POLY, the regularization parameter (α) and degree (deg) were varied. For the SVGP, the number of inducing points (IP), latent functions (LF), and learning rate (LR) were changed throughout the scans.

5.3.2 Results

In Figure 5.9a, the MAPE is calculated for each of the three ML models with a variable number of training data points from a dataset with 10% added noise. The MAPE is evaluated on the fixed size testing dataset of 250,000 points. With the NN and SVGP models, 20% of the training set was reserved for validation so model training could stop early if the validation error stopped decreasing. Here, we can clearly see that the NN and SVGP have a significantly lower percentage error than the POLY. Additionally, Figure 5.9b shows that the SVGP takes significantly longer than the NN to train which in turn takes significantly longer than the POLY (note the logarithmic scale).

Then, like in section 5.2, we analyzed the effect of changing the noise level in Figure 5.10. We can see that the POLY again has the worst accuracy which does not change with the noise level. While the SVGP and NN are more accurate, the SVGP seems to perform worse at a higher noise level.

5.3.3 Optimization Task

Similar to section 5.2, we came up with an optimization task to demonstrate the effectiveness of the models. This time, we used a slightly different objective function

$$f(KE_c, \eta_p) = \frac{|KE_c - KE_{c,goal}|}{1\text{MeV}}\beta - 100\eta_p(1 - \beta) \quad (5.32)$$

which can be contrasted to Equation 5.31. One notable difference is the subtraction of the conversion efficiency η_p instead of adding $1/\eta_p$. This allows us to control the relative strength of the two terms through a quantity β that varies from 0 to 1. Figure 5.11 shows the distribution of KE_c (i.e. E_{\max}) and η_p (i.e. $E_{\text{tot}}/E_{\text{laser}}$) as a function of target thickness and focal position when fixing the intensity and contrast to the maximum and minimum

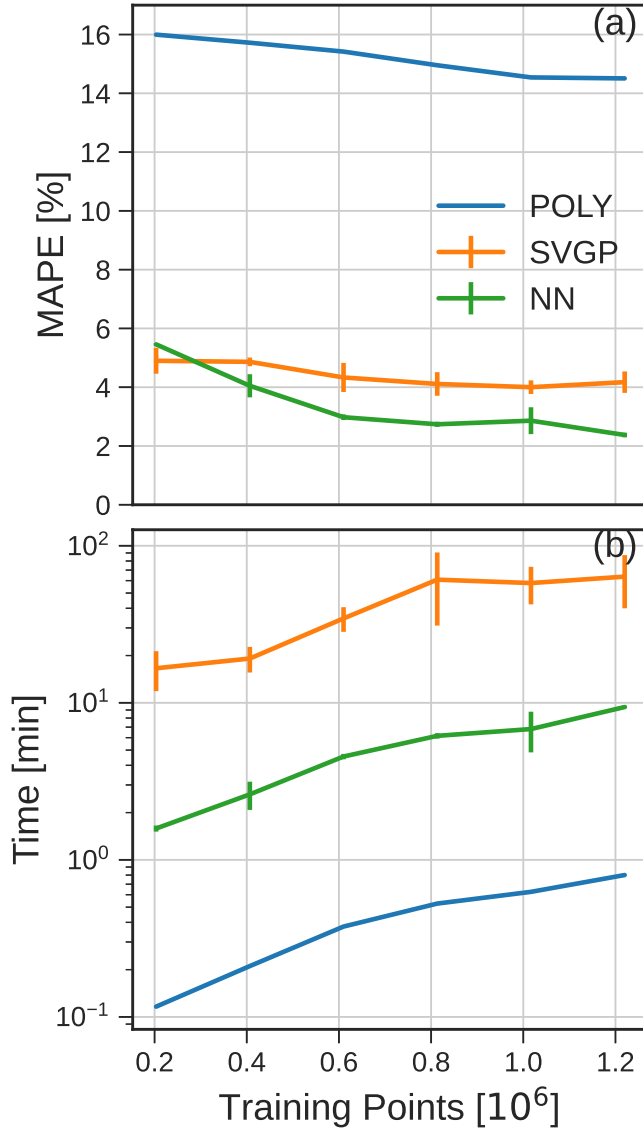


Figure 5.9: Model training results using data with 10% added noise. Testing MAPE (a) is plotted for the three ML models against the number of training points and averaged between results for maximum, average, and total proton energy. The training time (b) of the ML models in minutes is plotted on a logarithmic scale. The vertical bars are standard deviations computed from running the training splits 3 times with different seeds to control the data splitting and random parameter initialization of the NN and SVGP models.

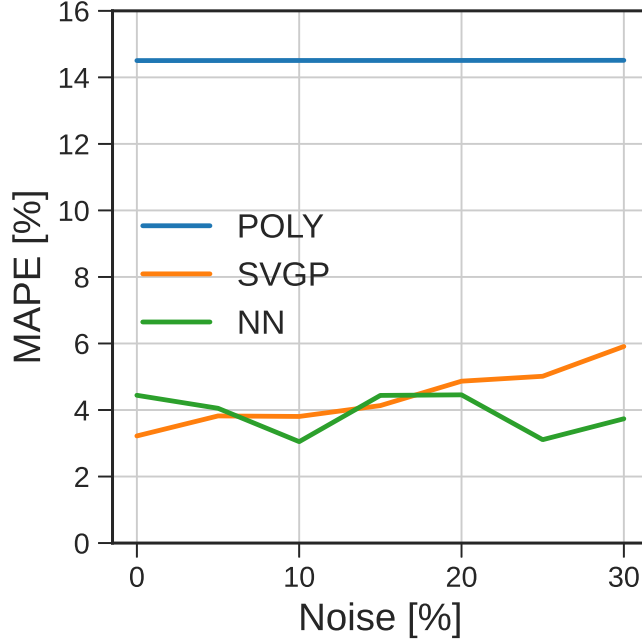


Figure 5.10: Testing MAPE is plotted against different levels of gaussian noise using the full training dataset for the three models with the three output energy results averaged.

within their respective ranges.

For our optimization task, we used the models trained on 30% added noise to sample a set of points which fixes the laser energy at 14.14mJ (by assuming $I_0 = 10^{19}\text{W cm}^{-2}$) and the contrast to $\kappa = 10^{-7}$, but varied the target thickness and focal distance. The thickness and focal distance were stepped in 0.1\AA increments to generate a 2D grid of 13,846 points to evaluate the trained models on. Notably, the step sizes are 5-10 times smaller than what was used in the dataset generation so that the models will be forced to interpolate between points not originally seen by the trained models.

The optimum conditions that minimize Equation 5.32 are indicated with a star in Figure 5.12 for a range of β values. In this analysis, the goal cutoff is fixed at $\text{KE}_{c, \text{goal}} = 1\text{ MeV}$, but this approach can easily be generalized to a different value. The upper panels of Figure 5.12 are the results from the analytic model (noiseless) and should be regarded as the true distribution of Equation 5.32. The optima of these panels are indicated with a white star. The other rows show the estimated distribution according to the three ML models and have predicted optima shown with a cyan star. For comparison, the white star from the analytic model is overlayed on each panel.

In Figure 5.12, one can see that for $\beta = 0.25$, the best (i.e. globally minimum) region is at 0.5 \mu m thickness and 10 \mu m focal position, which correspond to regions with higher η_p .

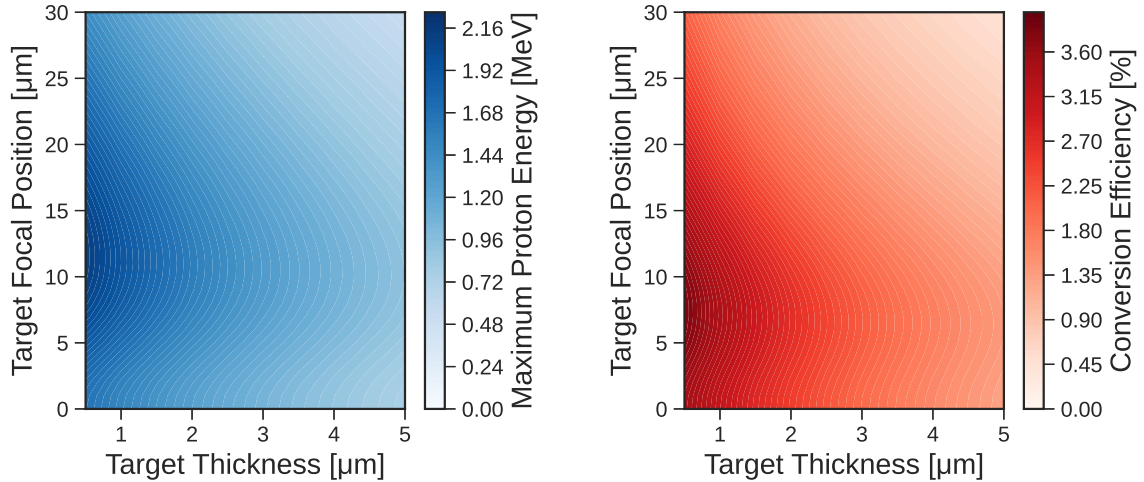


Figure 5.11: Colormaps in the 2D parameter space of target thickness and target focal position that display (left panel) the maximum proton energy (i.e. energy cutoff KE_c) and (right panel) laser to proton energy conversion efficiency η_p as calculated from the modified Fuchs et al model. These plots were generated assuming 14.14 mJ of laser energy and a pre-pulse contrast of 10^{-7} .

The **POLY** and **SVGP** models predict the optimal conditions to be at a focal position of $\sim 15 \mu\text{m}$, in contrast to the **NN** prediction of $\sim 11 \mu\text{m}$. In this case, the **NN** more closely matches the true optimum. For high values of β , the best region is a curve composed of points that closely match KE_c to $KE_{c,\text{goal}}$. Using the highest value of $\beta = 1$, we see that while the **NN** looks much less smooth, it fits the overall shape of the underlying Fuchs model better than the other two methods.

The features of Figure 5.12 are quantified in Table 5.3. We can assess the accuracy of the optimal conditions by taking the Euclidean distance in the focal position - target thickness space between the true optimum conditions and the **ML** predictions. This distance, termed Δ_{opt} , shows that (with the exception of $\beta = 1$), the **NN** predicted optimum is closer to the true model than the **SVGP** or **POLY**. To assess accuracy in the colormap as a whole, we can take the root mean squared error (RMSE) between the analytic model and the ML model's colormap values which clearly show lower error for the **NN** in comparison to the **SVGP** and **POLY**.

5.3.4 Constrained Data Campaign

Earlier, we describe how synthetic data was generated using a uniform grid in multiple dimensions of laser and target parameters. The primary training set data for the ML models discussed in the main body of the paper was obtained with this scheme. From an

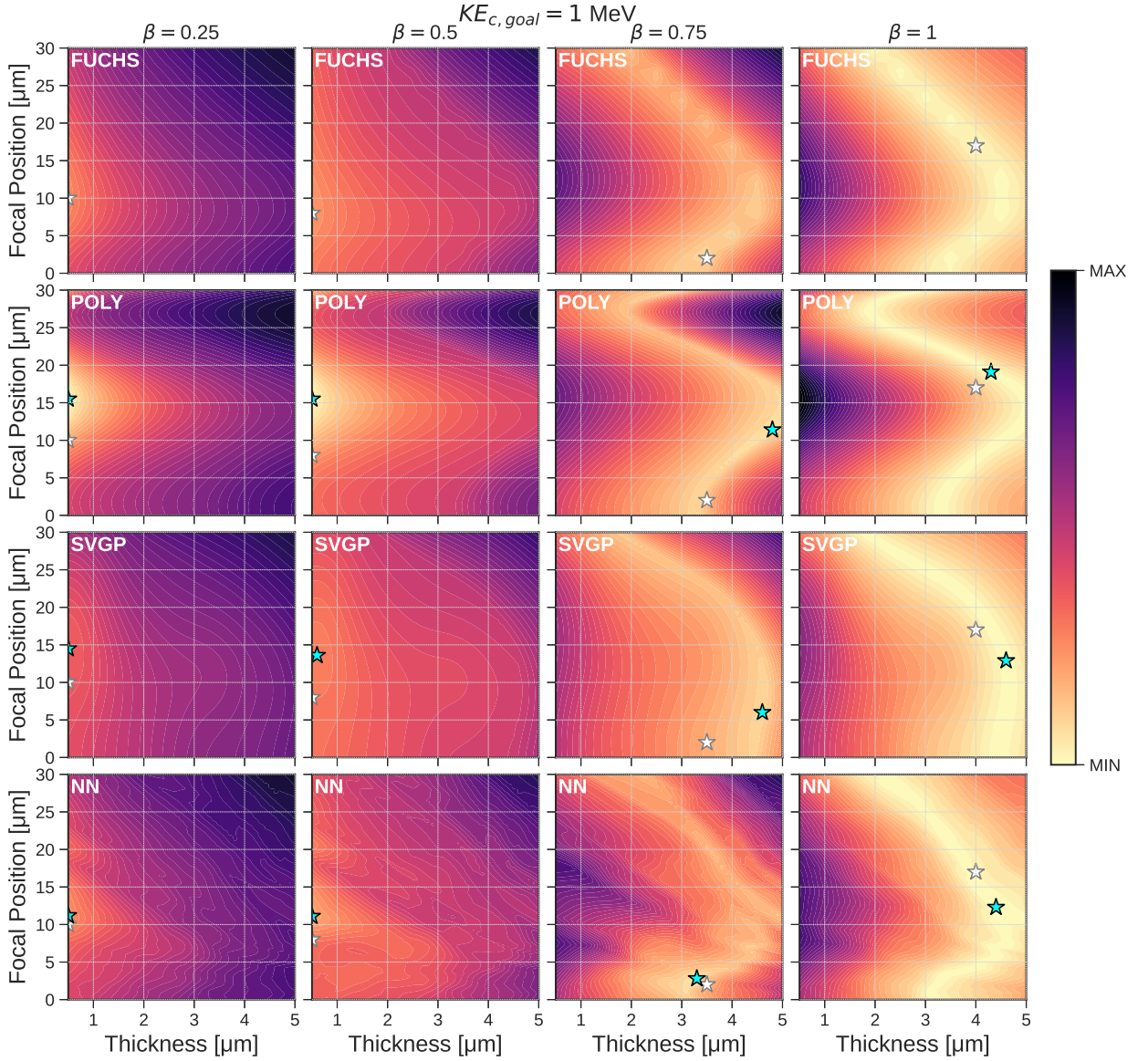


Figure 5.12: Colormaps that show estimates of Equation 5.32 assuming $KE_{c,\text{goal}} = 1 \text{ MeV}$ for the three ML models (NN, POLY and SVGP) and the modified Fuchs et al. model dataset with no added noise (FUCHS). The modified Fuchs et al. model with 30% added noise was used to produce the training data for the ML models. For each β value (i.e. each column), the same color levels are used in order to facilitate comparison between the models. A cyan colored star is placed at the location where each ML model predicts a minimum value for Equation 5.32 which can be compared to the analytic model prediction indicated by a white star.

	β	0	0.25	0.5	0.75	1
RMSE	POLY	0.329	0.223	0.121	0.057	0.124
	SVGP	0.143	0.096	0.062	0.065	0.101
	NN	0.065	0.052	0.042	0.038	0.042
$\Delta_{\text{opt}} [\mu\text{m}]$	POLY	4.5	5.5	7.5	9.489	2.121
	SVGP	3.5	4.5	5.601	4.148	4.144
	NN	0.4	1.2	3.1	0.825	4.717

Table 5.3: Comparison metrics evaluated from Figure 5.12. The RMSE row shows the root mean squared error between the colormap values of the ML models and the analytic model for each value of β . The Δ_{opt} row calculates the Euclidean distance between the predicted optimum and true optimum (i.e. distance in μm between the cyan and white stars in Figure 5.12).

experimental point of view, this approach is not very realistic because a real laser system will scan through the laser and target parameters in a very specific way with specific choices. For example, certain parameters could vary first while keeping other parameters constant, and then the opposite could happen to explore a different parameters. How do these choices affect the accuracy of ML models trained on this data? This is a question that we cannot yet answer conclusively, but we include an investigation into two realistic parameter scans (a.k.a. “campaigns”) that are used to train ML models instead of the uniform grid approach.

As highlighted in Figure 5.13, there were two experimental “campaigns” used to produce synthetic data – one where thickness, focal depth and laser energy were varied, and another where thickness, laser energy and pre-pulse contrast were varied between. All the synthetic data from the two campaigns were used to train ML models. In this way, our training set includes variation in four different input parameters.

The first campaign was generated by stepping through thickness-intensity coordinates, incrementing the focal distance by $3 \mu\text{m}$ and the thickness by $0.05 \mu\text{m}$, performing a full scan of focal depth values at $0.5 \mu\text{m}$ and every integer value until $5.0 \mu\text{m}$. At each point along the thickness-intensity curve, a full sweep of intensity was performed. Since, in a real experiment, the intensity can be controlled by varying a polarizing wave plate, the synthetic data set for this investigation varied the intensity by multiplying the maximum intensity value ($10^{19} \text{ W cm}^{-2}$) by the cosine-squared of an angle (which could be a polarizing waveplate), which was varied from 0° to 70° and back over the course of an intensity sweep. The resulting sweep is depicted in Figure 5.13a, creating a set of 1.15 million data points.

The second campaign was generated in a similar manner, but because, in a real experiment, neither main pulse nor pre-pulse laser intensity have an appreciable effect on target stability, both were able to be varied simultaneously. As such, the data set was generated by incrementing thickness by $0.05 \mu\text{m}$ from 0.5 to $5.0 \mu\text{m}$, taking a full scan of both main

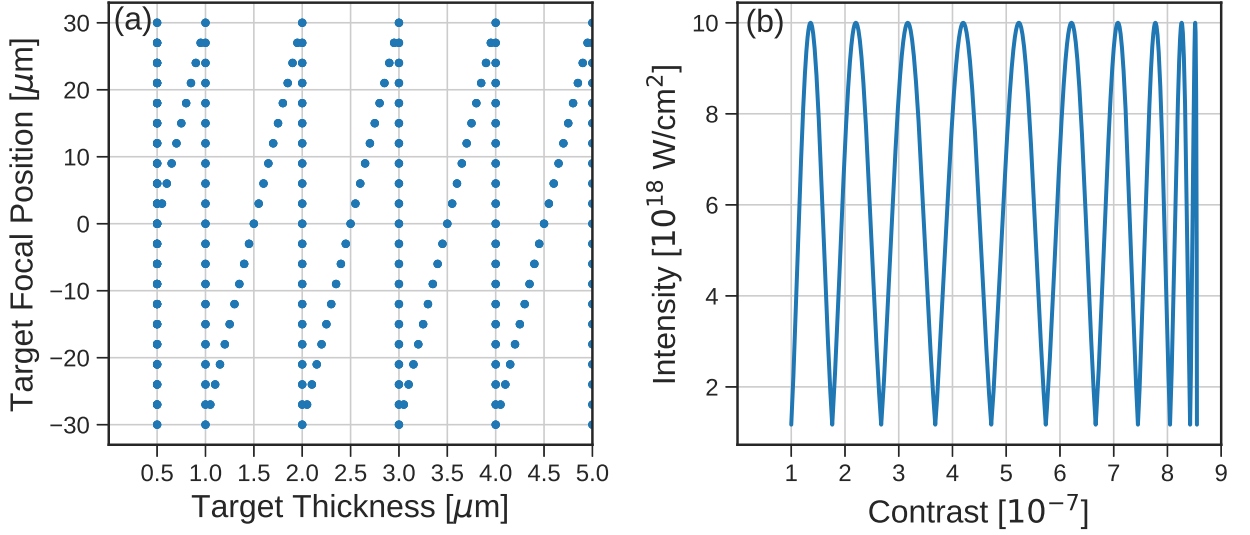


Figure 5.13: Synthetic data was generated in one of two “campaigns”. In (a) campaign 1, the target focus and thickness is varied in discrete steps and each blue dot varies the laser energy from minimum to maximum. In (b) campaign 2, the depicted intensity and contrast looping is performed for discrete steps in target thickness from $0.5 \mu\text{m}$ to $5\mu\text{m}$

pulse intensity and contrast at every thickness value. The pre-pulse contrast was varied in the same manner as the main pulse intensity, so the contrast was varied according to a cosine-squared function of another angle. The resulting data are depicted in Figure 5.13b, with an overall size of 1.27 million data points.

In both campaigns, choices about how many increments to make for different parameters were influenced by a constraint that each campaign last no more than about an hour on a 1 kHz repetition rate laser system. Both campaigns assumed 10% added gaussian noise, following the same prescription used in both section 5.2 and section 5.3. The combined training set, which includes data from both campaigns, has a total size of 2.42 million points. To better compare with earlier results shown in Figure 5.9a in which the ML models were trained with different numbers of training points, we randomly sampled from this data set to utilize a similar number of points. To test the accuracy of the trained ML mdoels, we use the same testing set utilized in Figure 5.9a, which did not include any noise. Our results are shown in Figure 5.14.

Figure 5.14 shows that, overall, the NN and SVGP models have a much higher MAPE than was seen earlier in Figure 5.9a. Also, a third order polynomial fits the data set almost as well as the NN and SVGP which indicates that NN and SVGP models are not able to fit the underlying model very well when trained on data split into the two campaigns we described. A possible improvement could be an experimental design where both the target

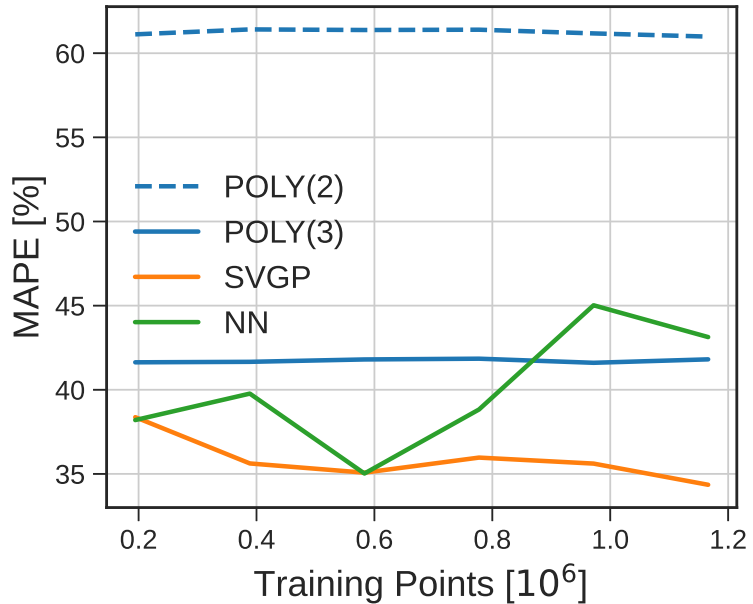


Figure 5.14: Testing set MAPE evaluated on several ML models trained on data combined from two separate campaigns shown in [Figure 5.13](#). The dashed line differs from the solid blue line in the polynomial degree.

The different data splits are chosen to be approximately the same as what was shown in [Figure 5.9](#).

focal position and the pre-pulse contrast are varied simultaneously, rather than keeping the contrast fixed and varying the target focal position (first campaign), and then varying the contrast while keeping the target focal position fixed (second campaign). But varying as many as four parameters simultaneously creates its own challenges for exploring a large parameter space in a relatively short amount of time ($\sim 1\text{-}2$ hours).

5.4 Conclusion

In [section 5.1](#), we reviewed the physics of the isothermal expansion model for which the Fuchs et al. model is based upon. Then, we showed the modifications that we made to the model to better fit data at the Extreme Light Laboratory at the Wright-Patterson Air Force Base and account for pre-expansion of the target. From this modified model, we were well equipped to construct a synthetic dataset that could have multiple inputs/outputs and added noise.

Then, in [section 5.2](#), we summarized our first machine learning effort which analyzed a 25,000 point dataset with three machine learning methods: gaussian process regression, neural networks, and support vector regression. In this work, we generally found that

the neural network model was the least accurate and had the worst performance on our optimization task. This was not that surprising because neural networks generally only work well for complex datasets. The gaussian process regression and support vector regression were both similarly accurate; in part, this was due to the relatively simple physics model we used. However, the gaussian process consumed a lot of memory and would be unsuitable for larger datasets.

Next, in [section 5.3](#), we described the second machine learning effort which expanded upon the first by using a dataset of over 1 million points. Here, we also used a more complex model that accounted for an additional input (pre-pulse contrast). We did a similar analysis and found that the added complexity actually made the neural network model a more favorable choice. We used a different implementation of the gaussian process which was capable of handling the million point dataset and achieved good accuracy, but still suffered from long run times. The added complexity also made it difficult for the simpler polynomial model to fit the data.

Throughout this chapter, we explored a novel idea in the field of plasma physics: generating a synthetic dataset based on modifications of established physical models to provide machine learning insights. Our model could, in principle, further be improved to take into account other phenomena that a 1D model could not capture like the shape of the target or the laser angle of incidence. Even though the model may not match up exactly to experiment, it would have the desired trends expected from a real experiment which can at least give us insights into how a hypothetical machine learning framework might operate. By offering the code and synthetic datasets publicly [[100](#), [101](#)], we hope that other researchers in this field can be better prepared to handle the vast amounts of data that future high repetition-rate lasers with continuously refreshing fluid targets can produce.

Chapter 6

OPTIMIZATION AND CONTROL OF A kHz LASER SYSTEM

The work of [chapter 5](#) has illustrated the usefulness of machine learning methods in the field of ion acceleration and what sort of quantities might be optimized. To generate enough data for the [ML](#) algorithms, the facilities need to use both a high-repetition rate laser (i.e. many shots per second) and a continuously refreshing target (e.g. a flowing liquid or tape drive target). Using such a system, no research group has yet obtained a stable and tunable MeV source of protons required for applications. At [RAL](#) using a solid Kapton tape, Loughran et al. [97] used [BO](#) on around 60 bursts of shots. At [Colarado State University \(CSU\)](#) with a flowing liquid target, multi-MeV deuteron acceleration [112] was demonstrated from a flowing liquid target, but only for 2 minutes and 60 total shots.

At the Wright-Patterson Air Force Base, a 1 kHz, mJ class laser system exists that is capable of producing MeV protons [22]. In comparison to the two previously mentioned laser facilities at [CSU](#) and [RAL](#), a 1 kHz laser shoots one thousand to two thousand times more shots per second! A laser system that shoots one thousand times more shots per second, however, will also roughly have a thousand times less laser energy per shot. Morrison et al. [22] was able to achieve 2 MeV protons on this kHz system at [WP-ELL](#), while higher energy Hz laser systems can easily achieve tens of MeV. To enhance the MeV proton yield within the existing mJ class laser system, the [TNSA](#) mechanism needs to be optimized as much as possible. This can be done in multiple ways:

- As explained in [chapter 4](#), multiple pulses can yield higher proton energies with the same amount of laser energy through [eTNSA](#). Even when the pulses are not spatially aligned, the preplasma induced from the first pulse can enhance the absorption from the second pulse and yield higher proton energies as long as the rear side of the target is relatively undisturbed [54]. Relevant parameters here would be pre-pulse contrast, time delay between pulses, and a variety of other spectral properties of the pulse could even be optimized through the use of an instrument like the DAZZLER (see Loughran

et al. [97] for an example).

- Generally, thinner targets see enhanced proton acceleration via the vacuum heating mechanism which is a well known scaling captured in the Fuchs et al. [79] model explored in [chapter 5](#). However, targets that are too thin may break up before the acceleration takes place. Relevant parameters here would be the thickness, composition, and shape of the target.

Evidently, many parameters influence the laser-target interaction in a very non-linear way which cannot be easily seen through the raw data. In this chapter, I give an overview of the kHz laser system at [WP-ELL](#) and particularly focus on the [data acquisition system \(DAQ\)](#) developed by fellow graduate student Nathaniel Tamminga and [CSUCI](#) professor Scott Feister. Then, the code and machine learning framework that I developed, with some help from Jack Felice, to send optimized parameters back to the [DAQ](#) is described. Finally, some results from this elementary machine learning feedback loop are discussed. The experimental operation of the laser was handled by the lab technician Kyle Frische. Miami University professor and former OSU graduate student Joseph Snyder helped with the experiments using his prior experience at the laboratory. Additionally, Anil Patnaik and Michael Dexter from AFIT and OSU professor Enam Chowdhury gave valuable feedback during weekly meetings for this effort. The results from this work are currently under consideration at *APL Machine Learning*.

6.1 Background

In this section, I will describe the experimental setup at the [WP-ELL](#) which uses a Ti:Sapphire based ultra-intense 780nm laser and a liquid sheet target.

6.1.1 Experimental Chamber

With a maximum energy of $\sim 9\text{mJ}$, [FWHM](#) period of 35 fs, the [WP-ELL](#) laser system is capable of producing pulses of peak intensity $5 \times 10^{18} \text{ W cm}^{-2}$ with a $1.8 \mu\text{m}$ [FWHM](#) spot size. By picking off a small amount of laser energy from the main pulse ($\sim 12 \mu\text{J}$), an artificial pre-pulse can be used with a tunable delay between the pulses. Each of the beams are focused by an [OAP](#) mirror. These features are shown in [Figure 6.1](#). Additionally, polarizing waveplates allow the main pulse and pre-pulse intensity to be reduced by up to a factor of ten by simply rotating the plate to a specific angle.

The sheet target, described in detail in George et al. [24], is formed by the grazing incidence of two extremely thin liquid streams of around $25 \mu\text{m}$ each. The target can be seen via shadowgraphy as seen in [Figure 6.2\(A\)](#). The laser interaction with the sheet target can be seen in [Figure 6.1](#) as the black dot in the center of the shadowgraph. We can see

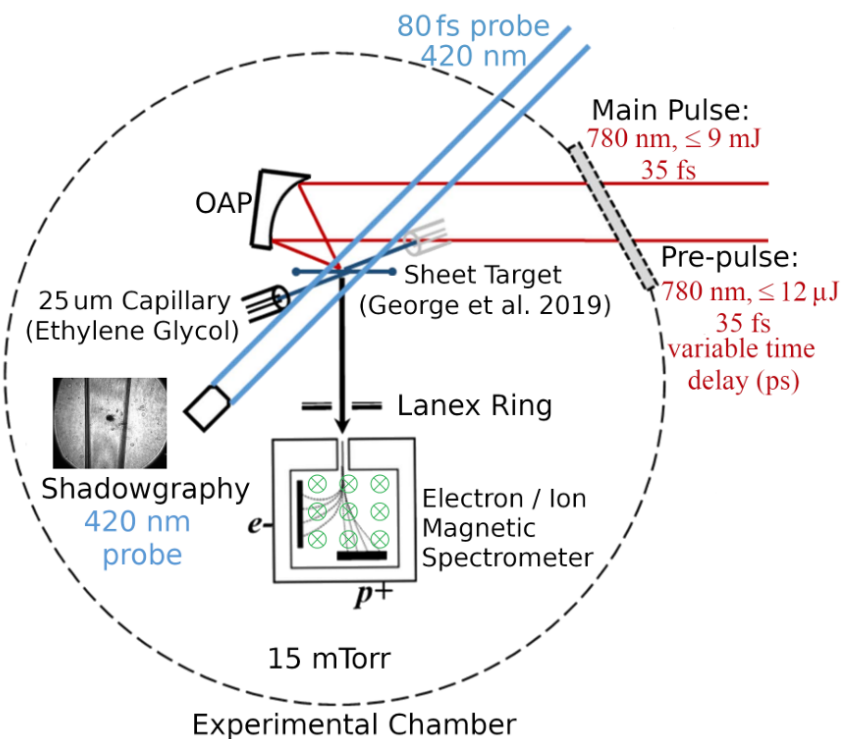


Figure 6.1: A schematic of the experimental chamber, targetry system, diagnostics, and laser pulses entering the chamber at a kHz repetition rate. Figure taken from a manuscript in review by Tammenga et al.

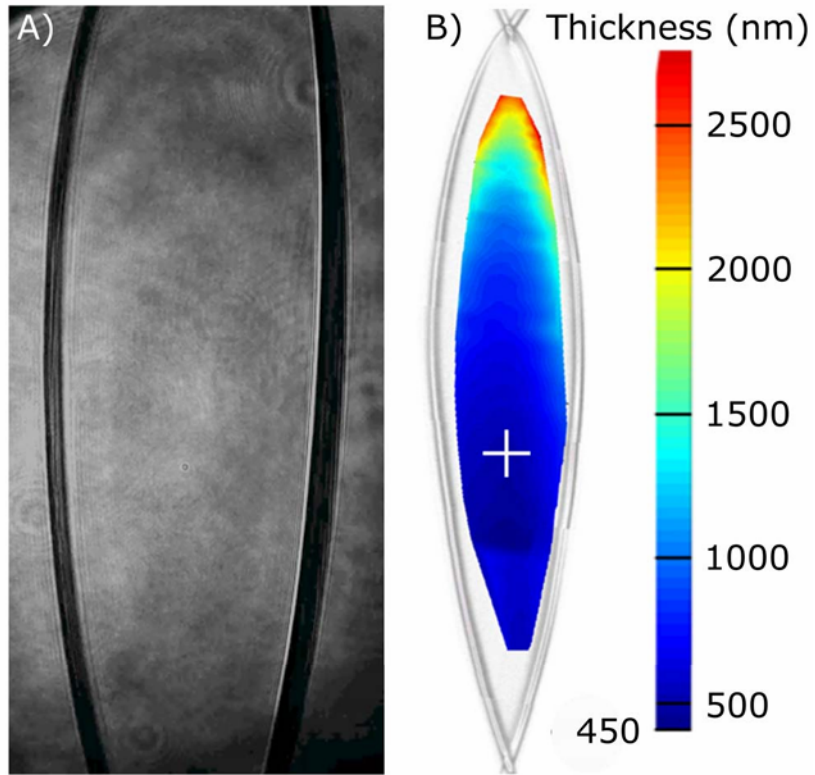


Figure 6.2: (A) Microscope Shadowgraphy image of the central region of the liquid sheet target in vacuum. (B) Spatially dependent thickness map across the liquid sheet, collected with a Filmetrics white-light interference profiler. The white cross indicates the location of the minimum sheet thickness at 450 nm. For scale, the width of the sheet in (B) is 560 μm . Figure reprinted from Figure 5 of George et al. [24].

in Figure 6.2(B) that the target has an oval shape which is why it is sometimes referred to as a “liquid-leaf” target [99]. Since background particles are deleterious to the laser-matter interaction [113], the chamber is pumped down to a pressure of 15 mTorr. Ethylene glycol is the chosen liquid in this experiment due to its ability to exist as a liquid at room temperature at these extremely low vacuum pressures, but other liquids (like H_2O or D_2O) can be used as well at a possibly higher pressure.

The electrons and ions accelerated normal to the rear of the sheet target travel through a Lanex Ring into the magnetic spectrometer. This spectrometer uses a magnet that deflects negative particles to the left and positive particles to the right (in reference to Figure 6.1). Using the fact that the cyclotron radius of a charged particle in a magnetic field varies based on its velocity, the final location of the deflected particle determines its kinetic energy. The charge coupled device (CCD) detectors are coated with scintillating material which converts the particle energy into a light signal that the CCDs can detect.

6.1.2 Data Sources

Spectrometers

The electron and proton spectra are collected from Mightex [CCD](#) cameras and stored in [Hierarchical Data Format 5 \(HDF5\)](#) files. They each have 3648 pixels where each pixel is 8 μm wide. The higher energy particles should be deflected less (which translates to hitting the bottom end of the detector for electrons and the left end of the detector for positive ions from [Figure 6.1](#)). The magnetic field profile has been mapped out in previous work [22] so that a one-to-one correspondence between pixel location and kinetic energy is established. These mappings for both electrons and protons are seen in [Figure 6.3](#).

The CCD pixels store counts up to 65,535¹⁸ which are collected over the desired exposure time. For example, if the Mightex cameras are set to collect at 100 Hz, they can have an exposure time of up to 10 ms. Pixels 0 to 900 for the proton CCD fall close to the direct line of sight of an undeflected particle and thus can receive stray signals from other radiation sources like x-rays. Since protons from this laser system have peaked at 2.5 MeV [22] (around pixel 1000), ignoring pixels 0 to 900 does not throw away any high energy proton data. Furthermore, 13 (additional) pixels are shielded from light which can be used to set a noise floor.

Laser Diagnostics

To accurately measure the main pulse and pre-pulse energy (or intensity) at a kHz rate, a tiny fixed percentage of the pulses are picked off and redirected at a diode. This diode measures a momentary increase in voltage over the course of 1 ms (due to the kHz collection rate) shown in [6.4a](#). The peak of this trace will be directly proportional to the energy of an individual shot. [6.4b](#) shows this voltage plotted over a range of 30,000 shots (30 seconds) where the laser energy was increased and decreased.

The calibration between the peak voltage and laser energy is shown in [Figure 6.5](#) which is clearly a linear relationship for both main and pre-pulse. As mentioned earlier, the angle of two polarizing waveplates controls the amount of energy that strikes the target. These two angles are tunable and can be accurately fit to the energy by using Malus' Law ($I = I_0 \cos^2(\theta)$).

Target Properties

As seen in [Figure 6.1](#), the sheet target is created by the interaction of two grazing incidence liquid microjets that shoot from two nozzles. These are situated on an XPS stage whose orientation and position can be tuned to micron-level precision.

¹⁸This number is the highest unsigned 16 bit integer

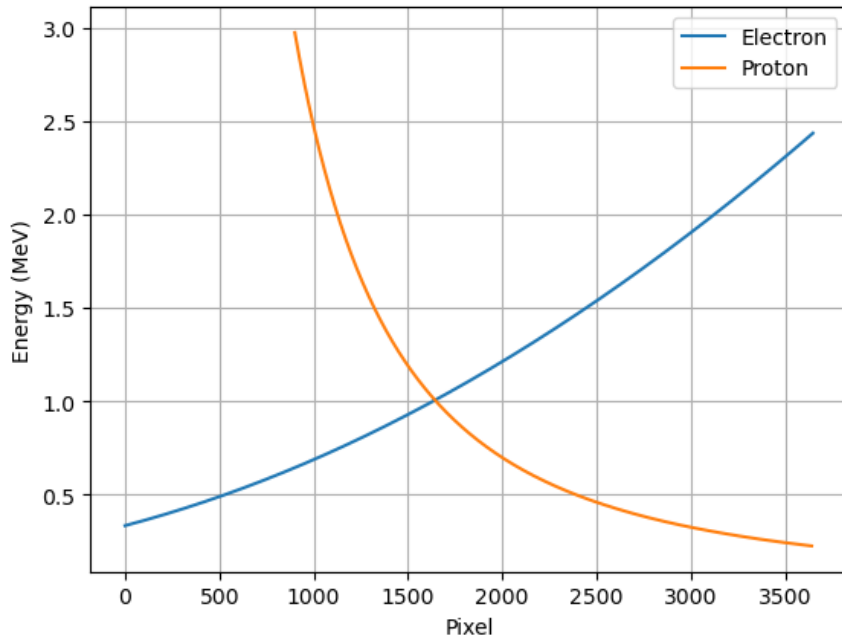


Figure 6.3: The pixel number to proton or electron kinetic energy mapping for the two CCDs present in the magnetic spectrometer. This is the same mapping that was used in Morrison et al. [22].

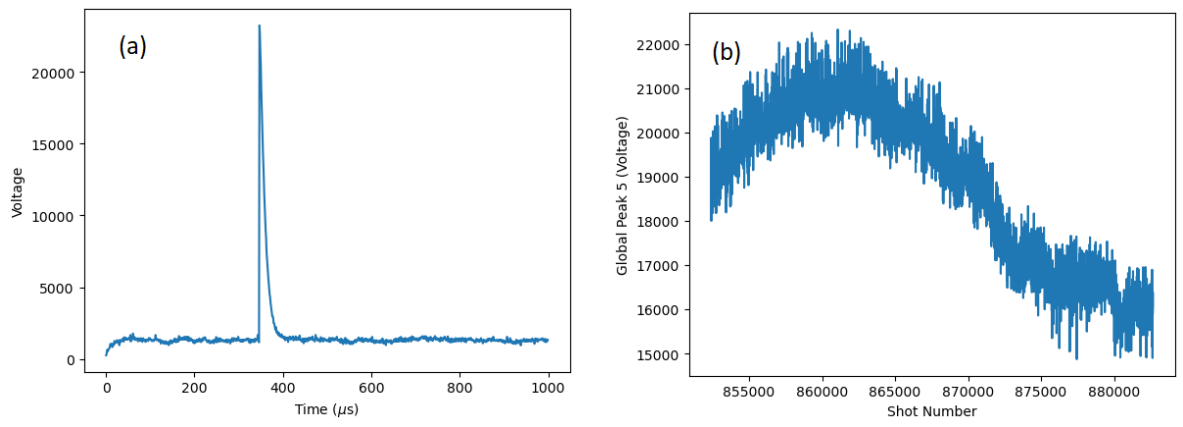


Figure 6.4: (a) An example of the voltage trace each individual shot registers on the laser diode. (b) The peak of the voltage trace is plotted for a range of shots.

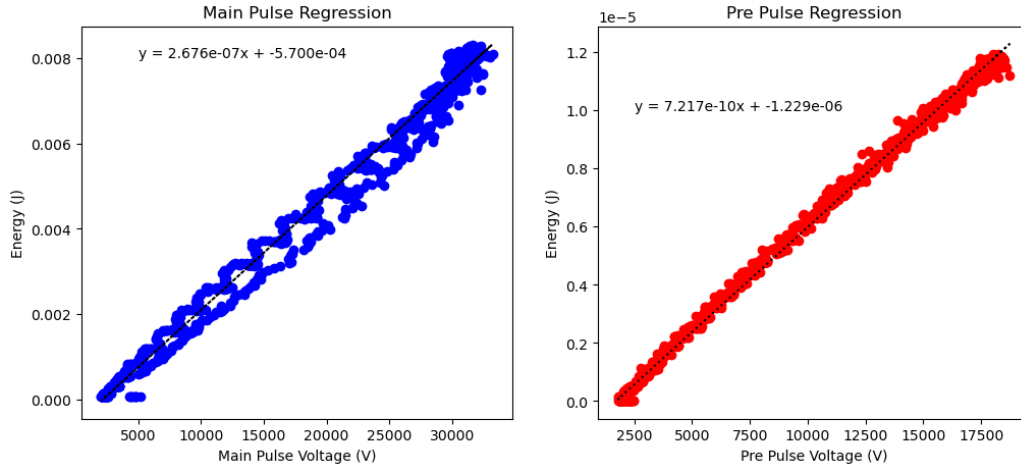


Figure 6.5: Linear relation from voltage to energy for both the main pulse (blue) and pre-pulse (red). The slope and intercept are displayed on the graphs.

In this work, we change the target position along the laser-axis direction which changes the distance between the peak focus of the laser and the target. Additionally, the XPS controllers have the ability to control other properties. The vertical target position can be changed which can, in principle, alter the target thickness as shown in Figure 6.2(B). Additionally, the nozzle angles and positions could be adjusted to modify the target shape. In this work, we only change the target position. Like the [CCDs](#) and diodes, the target data is also stored in the [HDF5](#) format (currently at a 5 Hz rate).

Other Sources

There are other potential radiation sources that can be measured but I will give two others as examples. The amount of ionizing radiation is already recorded the *Radiation Survey Log* that AFIT graduate student Benjamin Knight has created in units of mR/h (milli roentgen per hour). Second, neutrons have been detected [114] and optimizing their counts could give insights into high-repetition rate fusion.

6.2 Optimization Experiments

In this section, the data analysis suite I have developed will be explained in detail. Then, some results from one highlighted day will be explored to demonstrate the types of experiments that one could conduct using this setup.

6.2.1 Automated Data Extraction

Combining Data

Nathaniel and Scott have spent a great deal of time, before my involvement in the project, in making sure all the data sources described in subsection 6.1.2 are accurately synced up on a common index: the shot count. They have successfully integrated the lab with **Experimental Physics and Industrial Control System (EPICS)** which allows the values of the aforementioned data sources to be broadcasted throughout the lab network. In this way, we can extract the values of the waveplate angles, target positions, pre-pulse delay, and other values from any of the computers in the lab at any time. Furthermore, we can use **EPICS** commands from python scripts, LabVIEW interfaces, and other means to adjust these parameters in real time. Below, I will describe the process that I used to combine all the data and perform the analysis.

To start, I looked at the relevant locations at the lab computers to automatically grab the files from all the relevant data sources within a given time window (most of which were stored as **HDF5** files). I then created a pandas dataframe where each point corresponds to a unique Mightex shot count (i.e. an individual data point on the spectrometers). So, if the spectrometers were collecting at 20 Hz, I would take a rolling average of 50 nearby shots to compress the 1 kHz main and pre-pulse data down to 20 Hz. On the other hand, the target position and delay time were interpolated to fill values at a 20 Hz rate (since they collected at a 5 and 2 Hz rate respectively).

Then, to smooth the spectra, I subtracted out the noise using counts from the light shielded pixels and applied a median filter of window size 15 (replaces the given pixel counts with the median of the adjacent 15 pixel counts inclusive). From the spectra, I extracted two metrics: the 99th percentile energy/pixel E_{\max} and the total **CCD** counts N . Furthermore, I provided some extra processing to improve the data quality. First, I threw out data points that were oversaturated – that is the counts were so high that they were getting maxed out (beyond unsigned 16 bit precision) for a given pixel. Second, I removed points that didn't contain a sufficient number of electron or proton counts. Third, I implemented a measure to catch and fix the shot count if one of the spectrometers temporarily froze and reset its internal shot count¹⁹. Finally, I merged all the data sources together in one pandas dataframe which was then saved to a compressed **HDF5** file.

Data Visualization

Given a merged and filtered dataset, visualizing the data is easy. Figure 6.6 shows an interactive GUI based on data collected from June 14, 2024. In Figure 6.6(B), the main

¹⁹This is something that happened many times, especially when we collected the Mightex data at a higher rate (like 50 or 100 Hz). This is a “band-aid” fix that should not be needed in a future experiment

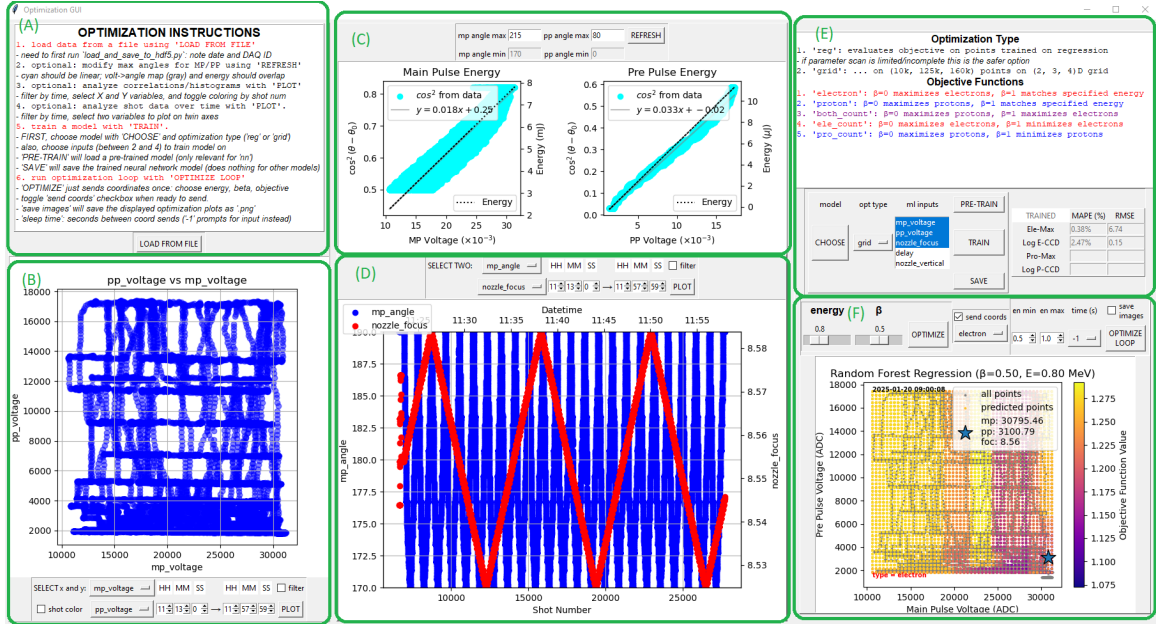


Figure 6.6: (A) A list of instruction on how to use the GUI and a button that loads in data already saved to a compressed HDF5 file. (B) A panel that shows two variables plotted against each other. (C) The mapping between cosine-squared of the waveplate angle and the measured voltage on the laser diodes. (D) Two variables are plotted as a function of time and shot number. (E) Instructions for the optimization task with options to choose a machine learning model, desired inputs, and displayed error metrics after training the model. (F) A visual of the optimization task which shows darker purple colors in regions of the parameter space that best optimize the chosen metric from Equation 6.1.

pulse and pre-pulse parameter space is adequately explored over a 45 minute time frame. In Figure 6.6(C), the cosine-squared mapping between the waveplate angle and diode voltage for both main and pre-pulse is shown. In the lab, the angle of the main pulse waveplate drifts over time, so an initial angle θ_0 is automatically inferred from the data corresponding to the waveplate angle that registers maximum voltage. In Figure 6.6(D), the main pulse and target focus position (`nozzle_focus`) are plotted as a function of shot number (and time) which shows approximately 25,000 shots worth of data.

To visualize the electron/proton spectrum, I used a different graphical user interface (GUI) which first loads data from a file shown in Figure 6.7(A). In Figure 6.7(B), the spectrum is plotted throughout the run and the bright yellow spots correspond to shot numbers and pixels with high counts. In Figure 6.7(C), a diagnostic plot is shown that measures the number of skipped shots in the data²⁰. In Figure 6.7(D, E) the electron spectrum for a specified shot is plotted as a function of either pixel number or energy in

²⁰Sometimes, especially when running the spectrometers at a higher repetition rate, shots can be skipped over due to the inability of the virtual machines to keep up with the data acquisition

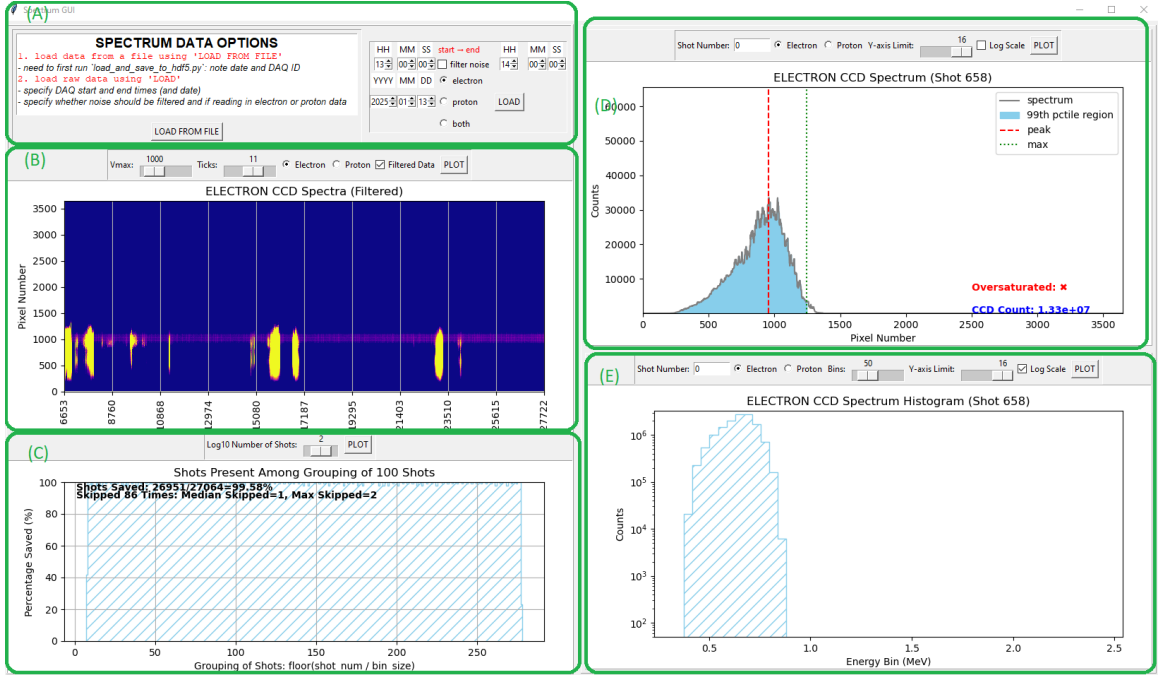


Figure 6.7: (A) A list of instructions on how to load in the data. (B) A heatmap that shows the pixel counts for the shot numbers throughout the run. (C) A diagnostic that shows where (if any) shots are erroneously being missed due the lab equipment. (D) An electron spectrum plotted for a specified shot. (E) An electron spectrum binned by energy in MeV on a log scale.

MeV. These can either be plotted on a linear y-scale or a log y-scale.

6.2.2 Optimization Feedback Loop

The developed ML framework was tested out on various days in the summer of 2024. In this subsection, I will highlight one particular day: June 14, 2024 which varied the main-pulse, pre-pulse and target position according to [Table 6.1](#). The data seen in [Figure 6.6](#) and [Figure 6.7](#) are also from this day.

These three quantities were simultaneously varied with three different periods so that the 3D parameter space would be adequately explored. The approximately 25,000 data points from this 45 second run were stored in a consolidated [HDF5](#) file. After this, we used the optimization [GUI](#) in [Figure 6.6\(E\)](#) to quickly fit a regression with specified hyperparameters on the collected data. Similar to [section 5.3](#), we used min-max scaling on all the inputs due to the fixed parameter bounds in [Table 6.1](#), but use standard z-score scaling on the outputs (logarithm of the ccd counts and 99th percentile energy). This model is used to smooth over noisy data points and we can apply a metric (just like what was done in [section 5.2](#) and [section 5.3](#)) to optimize for two different properties. Here, we use the following objective

Explored Parameter	Max	Min	Scan Period
Main Pulse Energy	8.4 mJ	$\lesssim 1$ mJ	80 s
Pre-Pulse Energy	12 μ J	$\lesssim 1$ μ J	104 s
Target Position	+30 μ m	-30 μ m	700 s

Table 6.1: A description of the experimental parameters, the range they were scanned through, and the period of the parameter scan. This table was reproduced from forthcoming work in Tamminga et al. (2025).

function

$$f(KE_{\text{cutoff}}, N_e) = 1 + (1 - \beta) \cdot \left(1 - \frac{\log_{10}(N_e)}{8}\right) + \beta \frac{|KE_c - KE_{c,\text{goal}}|}{KE_{c,\text{goal}}} \quad (6.1)$$

which looks notably similar to [Equation 5.32](#) if the logarithm of the [CCD](#) electron counts N_e replaces the conversion efficiency η . We attempted to perform a similar optimization task as explored in [chapter 5](#), but the electron data signals were largely concentrated at the same energy (regardless of input conditions) which can be seen in [Figure 6.7\(D, E\)](#). This spectrum peaks around 0.7 or 0.8 MeV but can have a higher or lower number of counts based on the input parameters. We found (unsurprisingly) that the conditions with highest electron counts correspond to maximum main pulse intensity, minimum pre-pulse intensity, and close to peak focus. An example of this can be seen in [Figure 6.6\(F\)](#) which highlights the main pulse and pre-pulse optimal conditions with a blue star. For this run, 8.555 mm was the absolute position of the target when peak focus was achieved which matches the peak focus listed in the figure legend.

Even though the electron spectra did not offer a lot of interesting physics to explore, we did successfully implement a feedback loop which sent the optimized main pulse, pre-pulse, and focus conditions back to motion controllers and waveplates in the lab via the [EPICS](#) protocol. An example of this can be seen in [Figure 6.8](#) where, during a second data collection, optimized parameters from the first run were sent via [EPICS](#) to change the electron spectra in real-time. Each value of β specified a slightly different set of input parameters that were tested for 30 seconds before moving on to the next value of β . We can see that the higher values of β have maximum electron kinetic energy closer to 0.7 MeV in comparison to the lower values of β (with the notable exception $\beta = 0$). Importantly, these steps were all taken automatically through the use of a Python script.

6.3 Conclusion

The chapter started by overviewing the experimental setup in [section 6.1](#) of the [WP-ELL](#) which includes a 1 kHz femtosecond laser, up to 100 Hz particle spectrometers, and a

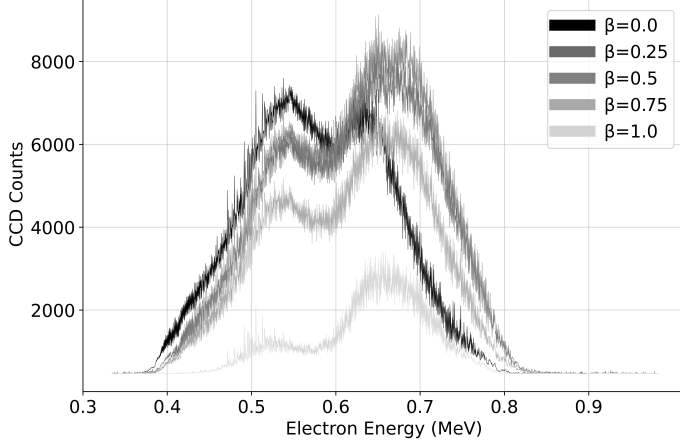


Figure 6.8: Electron spectra plotted for various levels of β for a specified cutoff energy $KE_{c,\text{goal}} = 0.7$ MeV. The different spectra are predicted optimal parameters from a random forest model trained on data collected in an earlier run.

free-flowing liquid target. Many parameters like the main/pre-pulse peak intensity, focus position in reference to the target, pulse delays, and more can be easily adjusted independent of one another. Then, we explained the optimization experiment in [section 6.2](#) where three input parameters were varied simultaneously over the course of one data collection run. This data was used to train a [ML](#) model that could map these three input target conditions to features of an electronic spectra: the maximum energy and total counts on the [CCD](#). The trained model was then used to predict optimal inputs according to [Equation 6.1](#)). Finally, these predicted optima were sent via [EPICS](#) to the relevant lab equipment in an automated way to explore laser and target conditions that yield a desired spectrum. We showed in [Figure 6.8](#) that this feedback loop can work in principle to balance two competing properties: maximum kinetic energy and high electron counts.

While this work is certainly important, it is still in early stages. We have the ability to collect proton spectra which can be more difficult to obtain but have more use for applications. However, the amount of proton data that we are able to get is usually minimal – much of the explored parameter spaces end up with no proton signal. To make real progress, we would need to make improvements on the experimental side to obtain a more stable target that could reliably generate MeV protons for a range of different input conditions.

Furthermore, our current feedback loop involves fitting a relatively simple regression to the data – something that is only possible when the size of the data is small (tens of thousands) and there are only a few different parameters. A more useful model that could feasibly handle larger and more complex datasets would be the [NN](#) as evidenced by [section 5.3](#). Additionally, [GPU](#)-accelerated computations would be necessary to operate this feedback loop in real-time. After obtaining several high-quality datasets scanning different

parameters, we could pre-train the [NN](#) so that when presented with a limited amount of new data from a different day, it could more quickly assess the ideal laser conditions. Nonetheless, the work presented here represents an important first step in incorporating [ML](#) methods to optimize [TNSA](#) accelerated protons in real-time.

Chapter 7

CONCLUSION

In [chapter 1](#), I discussed the features of chirped-pulse lasers that enabled the creation of ultra-intense laser systems used today. When used to accelerate ions from flat targets, these lasers have a multitude of applications including cancer therapy, radiography, and materials characterization. The relevant plasma physics necessary to understand these laser-matter interactions was reviewed in [chapter 2](#) which includes the primary effect studied in this work: target normal sheath acceleration. In [chapter 3](#), I explained the basics of particle-in-cell codes and machine learning which were the computational techniques used in this work.

In [chapter 4](#), I summarized the existing literature on using multiple pulses to improve the target normal sheath acceleration mechanism. In particular, I highlighted two works [\[18, 90\]](#) which simulated two femtosecond pulses of equal energy that arrive at the same location and time to enhance accelerated proton beams (in comparison to one pulse with the same total energy). I conducted similar simulations based on the longer, picosecond scale Titan laser at Lawrence Livermore National Laboratory. These simulations were done to complement the experiment that our research group conducted early in 2024 and yielded similar qualitative and quantitative results.

In [chapter 5](#), I explained my main contribution to the research group during my PhD studies: studying machine learning models through the use of synthetic proton acceleration data. I reviewed the relevant physics in the datasets which includes *plasma expansion into a vacuum* [\[20\]](#) and the Fuchs et al. model [\[79\]](#) which are partly based on empirical estimates from prior experiments. I detailed the synthetic datasets with some additional modifications to account for target pre-expansion due to an artificially injected pre-pulse. Then in two projects, I explored various machine learning models in their ability to accurately fit the synthetic data. These projects primarily showed that neural networks have the potential to be useful models for large, complex datasets. Their strengths lie in being resilient to noise, their ability to update with new data (via transfer learning), and their capability to leverage GPU computations. However, when faced with a limited amount of data, gaussian

processes are preferred due to their uncertainty measure that can help suggest new points to explore. Synthetic data offers an alternative to computationally expensive particle-in-cell simulation data which can be a useful tool to prototype future machine learning frameworks in this field.

In [chapter 6](#), I overview the experimental laser facility at the Wright-Patterson Air Force Base for which [chapter 5](#) was based on. I described my contribution to the project: a graphical user interface that automatically processed data from the lab and suggested new laser parameters to explore based on certain criteria like maximum kinetic energy and total electron counts. Operating at 1 kHz, this system is capable of collecting around 3 orders of magnitude more data points than many other modern 1 Hz *high* repetition-rate system that have been used in recent years [112, 115]. This makes it particularly suitable for utilizing machine learning models like neural networks optimized for complex data. I demonstrated at the lab with my code that this type of optimization is possible, but the narrow region of parameter space that produced a good proton signal limited the applicability of my work.

While future laser facilities will be able to more readily access higher intensities that utilize radiation pressure acceleration mechanisms [54], target normal sheath acceleration will continue to remain relevant for some time due to high repetition-rated systems that can produce vast quantities of data at a lower intensity. Continuously refreshing targets created from liquid micro-jets (like the one at Wright-Patt [24]) are getting better at supporting higher acquisition rates [112, 115] which will allow scientists to leverage data to understand physical processes not yet understood from theory. I am proud to have contributed insights to the field of laser-driven proton acceleration by studying the double pulse enhanced target normal sheath acceleration mechanism, constructing synthetic datasets to understand what sorts of optimizations are possible, and realizing a basic optimization feedback loop.

To expand on this work, one could try to develop a more comprehensive theory for the double pulse enhancement that justifies its implementation in the lab. After target stability improvements and data acquisition advancements, different laser and target properties (including the double pulse setup) could be varied to collect many data points. This could be used for machine learning efforts to not only better understand target normal sheath acceleration, but tune parameters to drive higher quality proton beams of a desired energy and angular spread. Due to recent advances in both machine learning and repetition-rated targetry, I am optimistic that future efforts will enable laser-plasma accelerators to be a viable alternative to conventional proton (and other types of radiation) accelerators to realize medical and scientific applications.

BIBLIOGRAPHY

- [1] MeetOptics. Laser fundamentals: operation and beam characteristics. <https://www.meetoptics.com/academy/laser-fundamentals#how-do-lasers-work>. Accessed: 2025-01-30.
- [2] Marco Arrigoni and Jean-Luc Tapié. Chirped pulse amplification. *Photonics Views*, 16(3):78–82, 2019.
- [3] I.V. Yakovlev. Stretchers and compressors for ultra-high power laser systems. *Quantum Electronics*, 44(5):393, may 2014.
- [4] Radhe Mohan. A review of proton therapy – current status and future directions. *Precision Radiation Oncology*, 6(2):164–176, 2022.
- [5] R. Betti and O. Hurricane. Inertial-confinement fusion with lasers. *Nature Physics*, 12:435–448, May 2016.
- [6] Frédéric Boivin, Simon Vallières, Sylvain Fourmaux, Stéphane Payeur, and Patrizio Antici. Quantitative laser-based x-ray fluorescence and particle-induced x-ray emission. *New Journal of Physics*, 24(5):053018, may 2022.
- [7] Joseph Richard Harrison Smith. *Advanced Simulations and Optimization of Intense Laser Interactions*. PhD thesis, The Ohio State University, May 2020. Available at http://rave.ohiolink.edu/etdc/view?acc_num=osu1589302684037632.
- [8] S. C. Wilks, W. L. Kruer, M. Tabak, and A. B. Langdon. Absorption of ultra-intense laser pulses. *Phys. Rev. Lett.*, 69:1383–1386, Aug 1992.
- [9] Paul Gibon and A. R. Bell. Collisionless absorption in sharp-edged plasmas. *Phys. Rev. Lett.*, 68:1535–1538, Mar 1992.
- [10] D. W. Forslund, J. M. Kindel, and K. Lee. Theory of hot-electron spectra at high laser intensity. *Phys. Rev. Lett.*, 39:284–288, Aug 1977.
- [11] F. Brunel. Not-so-resonant, resonant absorption. *Phys. Rev. Lett.*, 59:52–55, Jul 1987.

- [12] Paul Gibbon. *Short Pulse Laser Interactions with Matter*. Imperial College Press, 2005.
- [13] M. Roth and M. S. Schollmeier. Ion acceleration - target normal sheath acceleration. In *Proceedings of the 2014 CAS-CERN Accelerator School: Plasma Wake Acceleration*, volume 1, pages 231–270, 2 2016.
- [14] K. V. Lezhnin, F. F. Kamenets, V. S. Beskin, M. Kando, T. Zh. Esirkepov, and S. V. Bulanov. Effect of electromagnetic pulse transverse inhomogeneity on ion acceleration by radiation pressure. *Physics of Plasmas*, 22(3):033112, 03 2015.
- [15] WarpX collaboration. Particle-in-cell method. <https://warpx.readthedocs.io/en/latest/theory/pic.html>. Accessed: 2025-02-07.
- [16] K. Markey, P. McKenna, C. M. Brenner, D. C. Carroll, M. M. Günther, K. Harnes, S. Kar, K. Lancaster, F. Nürnberg, M. N. Quinn, A. P. L. Robinson, M. Roth, M. Zepf, and D. Neely. Spectral enhancement in the double pulse regime of laser proton acceleration. *Phys. Rev. Lett.*, 105:195008, Nov 2010.
- [17] G. G. Scott, J. S. Green, V. Bagnoud, C. Brabetz, C. M. Brenner, D. C. Carroll, D. A. MacLellan, A. P. L. Robinson, M. Roth, C. Spindloe, F. Wagner, B. Zielbauer, P. McKenna, and D. Neely. Multi-pulse enhanced laser ion acceleration using plasma half cavity targets. *Applied Physics Letters*, 101(2):024101, 07 2012.
- [18] J. Ferri, E. Siminos, and T. Fülöp. Enhanced target normal sheath acceleration using colliding laser pulses. *Communications Physics*, 2:40, 4 2019.
- [19] Weipeng Yao, Motoaki Nakatsutsumi, Sébastien Buffecheoux, Patrizio Antici, Marco Borghesi, Andrea Ciardi, Sophia N. Chen, Emmanuel d’Humières, Laurent Gremillet, Robert Heathcote, Vojtěch Horný, Paul McKenna, Mark N. Quinn, Lorenzo Romagnani, Ryan Royle, Gianluca Sarri, Yasuhiko Sentoku, Hans-Peter Schlenvoigt, Toma Toncian, Olivier Tresca, Laura Vassura, Oswald Willi, and Julien Fuchs. Optimizing laser coupling, matter heating, and particle acceleration from solids using multiplexed ultraintense lasers. *Matter and Radiation at Extremes*, 9(4):047202, 04 2024.
- [20] P. Mora. Plasma expansion into a vacuum. *Phys. Rev. Lett.*, 90:185002, May 2003.
- [21] John J. Felice, Ronak Desai, Nathaniel Tamminga, Joseph R. Smith, Alona Kryshchenko, Chris Orban, Michael L. Dexter, and Anil K. Patnaik. Towards automated learning with ultra-intense laser systems operating in the khz repetition rate regime, 2025.

- [22] John T. Morrison, Scott Feister, Kyle D. Frische, Drake R. Austin, Gregory K. Ngirmang, Neil R. Murphy, Chris Orban, Enam A. Chowdhury, and W. M. Roquemore. MeV proton acceleration at kHz repetition rate from ultra-intense laser liquid interaction. *New Journal of Physics*, 20(2):022001, February 2018.
- [23] John J. Felice, Ronak Desai, Nathaniel Tamminga, Joseph R. Smith, Alona Kryshchenko, Chris Orban, Michael L. Dexter, and Anil K. Patnaik. Towards automated learning with ultra-intense laser systems operating in the khz repetition rate regime. *Contributions to Plasma Physics*, page e202400080, 2024.
- [24] K. M. George, J. T. Morrison, S. Feister, G. K. Ngirmang, J. R. Smith, A. J. Klim, J. Snyder, D. Austin, W. Erbsen, K. D. Frische, and et al. High-repetition-rate (\geq kHz) targets and optics from liquid microjets for high-intensity laser–plasma interactions. *High Power Laser Science and Engineering*, 7:e50, 2019.
- [25] Albert Einstein. The quantum theory of radiation. *Physikalische Zeitschrift*, 18(121), 1917.
- [26] Donna Strickland and Gerard Mourou. Compression of amplified chirped optical pulses. *Optics Communications*, 56(3):219–221, 1985.
- [27] NobelPrize.org. Press release. <https://www.nobelprize.org/prizes/physics/2018/press-release/>, 2018. Accessed: 2024-12-19.
- [28] Mayo Clinic Staff. Radiation therapy. <https://www.mayoclinic.org/tests-procedures/radiation-therapy/about/pac-20385162>, 2024. Accessed: 02-07-2025.
- [29] W. H. Bragg and R. Kleeman. Xxxix. on the particles of radium, and their loss of range in passing through various atoms and molecules. *The London, Edinburgh, and Dublin Philosophical Magazine and Journal of Science*, 10(57):318–340, 1905.
- [30] Robert R. Wilson. Radiological use of fast protons. *Radiology*, 47(5):487–491, 1946. PMID: 20274616.
- [31] James F. Ziegler, M.D. Ziegler, and J.P. Biersack. Srim – the stopping and range of ions in matter (2010). *Nuclear Instruments and Methods in Physics Research Section B: Beam Interactions with Materials and Atoms*, 268(11):1818–1823, 2010. 19th International Conference on Ion Beam Analysis.
- [32] <https://cancer.osu.edu/for-patients-and-caregivers/learn-about-cancers-and-treatments/clinical-services-at-the-james/radiation-oncology/treatment/proton-therapy>. Accessed: 2024-12-19.

- [33] Natalia Matuszak, Wiktoria Maria Suchorska, Piotr Milecki, Marta Kruszyna-Mochalska, Agnieszka Misiarz, Jacek Pracz, and Julian Malicki. Flash radiotherapy: an emerging approach in radiation therapy. *Reports of Practical Oncology and Radiotherapy*, 27(2):343 – 351, 2022.
- [34] Ute Linz and Jose Alonso. Laser-driven ion accelerators for tumor therapy revisited. *Phys. Rev. Accel. Beams*, 19:124802, Dec 2016.
- [35] Derek B. Schaeffer, Archie F. A. Bott, Marco Borghesi, Kirk A. Flippo, William Fox, Julien Fuchs, Chikang Li, Fredrick H. Séguin, Hye-Sook Park, Petros Tzeferacos, and Louise Willingale. Proton imaging of high-energy-density laboratory plasmas. *Rev. Mod. Phys.*, 95:045007, Dec 2023.
- [36] R A Simpson, D A Mariscal, J Kim, G G Scott, G J Williams, E Grace, C McGuffey, S Wilks, A Kemp, N Lemos, B Z Djordjevic, E Folsom, D Kalantar, R Zacharias, B Pollock, J Moody, F Beg, A Morace, N Iwata, Y Sentoku, M J-E Manuel, M Mauldin, M Quinn, K Youngblood, M Gatu-Johnson, B Lahmann, C Haefner, D Neely, and T Ma. Demonstration of tnsa proton radiography on the national ignition facility advanced radiographic capability (nif-arc) laser. *Plasma Physics and Controlled Fusion*, 63(12):124006, nov 2021.
- [37] A. B. Zylstra, C. K. Li, H. G. Rinderknecht, F. H. Séguin, R. D. Petrasso, C. Stoeckl, D. D. Meyerhofer, P. Nilson, T. C. Sangster, S. Le Pape, A. Mackinnon, and P. Patel. Using high-intensity laser-generated energetic protons to radiograph directly driven implosions. *Review of Scientific Instruments*, 83(1):013511, 01 2012.
- [38] Los Alamos Neutron Science Center. Proton radiography. <https://lansce.lanl.gov/facilities/pRad/index.php>, 2023. Accessed: 2025-01-31.
- [39] M. Passoni, L. Fedeli, and F. Mirani. Superintense laser-driven ion beam analysis. *Scientific Reports*, 9, JUN 24 2019.
- [40] Andreas Döpp, Christoph Eberle, Sunny Howard, Faran Irshad, Jinpu Lin, and Matthew Streeter. Data-driven science and machine learning methods in laser-plasma physics. *High Power Laser Science and Engineering*, page 1–50, 2023.
- [41] F.F. Chen. *Introduction to Plasma Physics and Controlled Fusion*. Springer, 3 edition, 2015.
- [42] Andrew Zangwill. *Modern Electrodynamics*. Cambridge University Press, 2012.
- [43] Andrea Macchi. *A Superintense Laser-Plasma Interaction Theory Primer*. Springer, 2013.

- [44] William Kruer. *The Physics of Laser Plasma Interactions*. CRC Press, 2003.
- [45] N. G. Denisov. On a singularity of the field of an electromagnetic wave propagated in an inhomogeneous plasma. *Soviet Physics JETP*, 4(4):544–553, 5 1957.
- [46] D. W. Forslund, J. M. Kindel, Kenneth Lee, E. L. Lindman, and R. L. Morse. Theory and simulation of resonant absorption in a hot plasma. *Phys. Rev. A*, 11:679–683, Feb 1975.
- [47] J. P. Freidberg, R. W. Mitchell, R. L. Morse, and L. I. Rudinski. Resonant absorption of laser light by plasma targets. *Phys. Rev. Lett.*, 28:795–799, Mar 1972.
- [48] K. G. Estabrook, E. J. Valeo, and W. L. Kruer. Two-dimensional relativistic simulations of resonance absorption. *The Physics of Fluids*, 18(9):1151–1159, 09 1975.
- [49] M. K. Grimes, A. R. Rundquist, Y.-S. Lee, and M. C. Downer. Experimental identification of “vacuum heating” at femtosecond-laser-irradiated metal surfaces. *Phys. Rev. Lett.*, 82:4010–4013, May 1999.
- [50] P. B. Corkum. Plasma perspective on strong field multiphoton ionization. *Phys. Rev. Lett.*, 71:1994–1997, Sep 1993.
- [51] NobelPrize.org. Press release. <https://www.nobelprize.org/prizes/physics/2023/press-release/>, 2023. Accessed: 2024-12-19.
- [52] David J. Griffiths. *Introduction to Electrodynamics*. Cambridge University Press, 4 edition, 2017.
- [53] W. L. Kruer and Kent Estabrook. $\mathbf{J} \times \mathbf{b}$ heating by very intense laser light. *The Physics of Fluids*, 28(1):430–432, 01 1985.
- [54] A. Macchi, M. Borghesi, and M. Passoni. Ion acceleration by superintense laser-plasma interaction. *Rev. Mod. Phys.*, 85:751–793, May 2013.
- [55] Zheng-Ming Sheng, Su-Ming Weng, Lu-Le Yu, Wei-Min Wang, Yun-Qian Cui, Min Chen, and Jie Zhang. Absorption of ultrashort intense lasers in laser–solid interactions*. *Chinese Physics B*, 24(1):015201, jan 2015.
- [56] T. H. Tan, G. H. McCall, and A. H. Williams. Determination of laser intensity and hot-electron temperature from fastest ion velocity measurement on laser-produced plasma. *The Physics of Fluids*, 27(1):296–301, 01 1984.
- [57] S. J. Gitomer, R. D. Jones, F. Begay, A. W. Ehler, J. F. Kephart, and R. Kristal. Fast ions and hot electrons in the laser–plasma interaction. *The Physics of Fluids*, 29(8):2679–2688, 08 1986.

- [58] M. Allen, P. K. Patel, A. Mackinnon, D. Price, S. Wilks, and E. Morse. Direct experimental evidence of back-surface ion acceleration from laser-irradiated gold foils. *Phys. Rev. Lett.*, 93:265004, Dec 2004.
- [59] J. E. Crow, P. L. Auer, and J. E. Allen. The expansion of a plasma into a vacuum. *Journal of Plasma Physics*, 14(1):65–76, 1975.
- [60] Yasuaki Kishimoto, Kunioki Mima, Tsuguhiro Watanabe, and Kyoji Nishikawa. Analysis of fast-ion velocity distributions in laser plasmas with a truncated Maxwellian velocity distribution of hot electrons. *The Physics of Fluids*, 26(8):2308–2315, 08 1983.
- [61] A. Maksimchuk, S. Gu, K. Flippo, D. Umstadter, and V. Yu. Bychenkov. Forward ion acceleration in thin films driven by a high-intensity laser. *Phys. Rev. Lett.*, 84:4108–4111, May 2000.
- [62] E. L. Clark, K. Krushelnick, M. Zepf, F. N. Beg, M. Tatarakis, A. Machacek, M. I. K. Santala, I. Watts, P. A. Norreys, and A. E. Dangor. Energetic heavy-ion and proton generation from ultraintense laser-plasma interactions with solids. *Phys. Rev. Lett.*, 85:1654–1657, Aug 2000.
- [63] R. A. Snavely, M. H. Key, S. P. Hatchett, T. E. Cowan, M. Roth, T. W. Phillips, M. A. Stoyer, E. A. Henry, T. C. Sangster, M. S. Singh, S. C. Wilks, A. MacKinnon, A. Offenberger, D. M. Pennington, K. Yasuike, A. B. Langdon, B. F. Lasinski, J. Johnson, M. D. Perry, and E. M. Campbell. Intense high-energy proton beams from petawatt-laser irradiation of solids. *Phys. Rev. Lett.*, 85:2945–2948, Oct 2000.
- [64] S. C. Wilks, A. B. Langdon, T. E. Cowan, M. Roth, M. Singh, S. Hatchett, M. H. Key, D. Pennington, A. MacKinnon, and R. A. Snavely. Energetic proton generation in ultra-intense laser-solid interactions. *Physics of Plasmas*, 8(2):542–549, 02 2001.
- [65] C. Perego, A. Zani, D. Batani, and M. Passoni. Extensive comparison among target normal sheath acceleration theoretical models. *Nuclear Instruments and Methods in Physics Research Section A: Accelerators, Spectrometers, Detectors and Associated Equipment*, 653(1):89–93, 2011. Superstrong 2010.
- [66] P. Mora. Thin-foil expansion into a vacuum. *Phys. Rev. E*, 72:056401, Nov 2005.
- [67] M. Passoni and M. Lontano. One-dimensional model of the electrostatic ion acceleration in the ultraintense laser-solid interaction. *Laser and Particle Beams*, 22(2):163–169, 2004.

- [68] Maurizio Lontano and Matteo Passoni. Electrostatic field distribution at the sharp interface between high density matter and vacuum. *Physics of Plasmas*, 13(4):042102, 04 2006.
- [69] M. Passoni and M. Lontano. Theory of light-ion acceleration driven by a strong charge separation. *Phys. Rev. Lett.*, 101:115001, Sep 2008.
- [70] C. Perego, D. Batani, A. Zani, and M. Passoni. Target normal sheath acceleration analytical modeling, comparative study and developmentsa). *Review of Scientific Instruments*, 83(2):02B502, 02 2012.
- [71] A. P. L Robinson, A. R. Bell, and R. J. Kingham. Effect of target composition on proton energy spectra in ultraintense laser-solid interactions. *Phys. Rev. Lett.*, 96:035005, Jan 2006.
- [72] B. J. Albright, L. Yin, B. M. Hegelich, Kevin J. Bowers, T. J. T. Kwan, and J. C. Fernández. Theory of laser acceleration of light-ion beams from interaction of ultrahigh-intensity lasers with layered targets. *Phys. Rev. Lett.*, 97:115002, Sep 2006.
- [73] P. K. Patel, A. J. Mackinnon, M. H. Key, T. E. Cowan, M. E. Foord, M. Allen, D. F. Price, H. Ruhl, P. T. Springer, and R. Stephens. Isochoric heating of solid-density matter with an ultrafast proton beam. *Phys. Rev. Lett.*, 91:125004, Sep 2003.
- [74] A. J. Mackinnon, Y. Sentoku, P. K. Patel, D. W. Price, S. Hatchett, M. H. Key, C. Andersen, R. Snavely, and R. R. Freeman. Enhancement of proton acceleration by hot-electron recirculation in thin foils irradiated by ultraintense laser pulses. *Phys. Rev. Lett.*, 88:215006, May 2002.
- [75] S. Vallieres. Enhanced laser-driven proton acceleration using nanowire targets. *Scientific Reports*, 11, 1 2021.
- [76] Joseph. Strehlow. A laser parameter study on enhancing proton generation from microtube foil targets. *Scientific Reports*, 12, 6 2022.
- [77] P. McKenna, D.C. Carroll, O. Lundh, F. Nürnberg, K. Markey, S. Bandyopadhyay, D. Batani, R.G. Evans, R. Jafer, S. Kar, and et al. Effects of front surface plasma expansion on proton acceleration in ultraintense laser irradiation of foil targets. *Laser and Particle Beams*, 26(4):591–596, 2008.
- [78] J. Ferri, L. Senje, M. Dalui, K. Svensson, B. Aurand, M. Hansson, A. Persson, O. Lundh, C.-G. Wahlström, L. Gremillet, E. Siminos, T. C. DuBois, L. Yi, J. L. Martins, and T. Fülöp. Proton acceleration by a pair of successive ultraintense femtosecond laser pulses. *Physics of Plasmas*, 25(4):043115, 04 2018.

- [79] J. Fuchs, P. Antici, E. D’Humières, E. Lefebvre, M. Borghesi, E. Brambrink, C. Cecchetti, M. Kaluza, V. Malka, M. Manclossi, S. Meyroneinc, P. Mora, J. Schreiber, T. Toncian, H. Pépin, and P. Audebert. Laser-driven proton scaling laws and new paths towards energy increase. *Nature Physics*, 2, 12 2005.
- [80] T. Tajima and J. M. Dawson. Laser electron accelerator. *Phys. Rev. Lett.*, 43:267–270, Jul 1979.
- [81] E. Esarey, C. B. Schroeder, and W. P. Leemans. Physics of laser-driven plasma-based electron accelerators. *Rev. Mod. Phys.*, 81:1229–1285, Aug 2009.
- [82] C.K. Birdsall and A.B. Langdon. *Plasma Physics Via Computer Simulation*. Series In Plasma Physics. Taylor & Francis, 2004.
- [83] T D Arber, K Bennett, C S Brady, A Lawrence-Douglas, M G Ramsay, N J Sircombe, P Gillies, R G Evans, H Schmitz, A R Bell, and C P Ridgers. Contemporary particle-in-cell approach to laser-plasma modelling. *Plasma Physics and Controlled Fusion*, 57(11):113001, sep 2015.
- [84] D.R. Welch, D.V. Rose, R.E. Clark, T.C. Genoni, and T.P. Hughes. Implementation of an non-iterative implicit electromagnetic field solver for dense plasma simulation. *Computer Physics Communications*, 164(1):183–188, 2004. Proceedings of the 18th International Conference on the Numerical Simulation of Plasmas.
- [85] Aurélien Géron. *Hands-on machine learning with scikit-learn, Keras, and tensorflow: Concepts, tools, and techniques to build Intelligent Systems*. O'Reilly Media, 2023.
- [86] F. Pedregosa, G. Varoquaux, A. Gramfort, V. Michel, B. Thirion, O. Grisel, M. Blondel, P. Prettenhofer, R. Weiss, V. Dubourg, J. Vanderplas, A. Passos, D. Cournapeau, M. Brucher, M. Perrot, and E. Duchesnay. Scikit-learn: Machine learning in Python. *Journal of Machine Learning Research*, 12:2825–2830, 2011.
- [87] D.H. Wolpert and W.G. Macready. No free lunch theorems for optimization. *IEEE Transactions on Evolutionary Computation*, 1(1):67–82, 1997.
- [88] J. Fuchs, C. A. Cecchetti, M. Borghesi, T. Grismayer, E. d’Humières, P. Antici, S. Atzeni, P. Mora, A. Pipahl, L. Romagnani, A. Schiavi, Y. Sentoku, T. Toncian, P. Audebert, and O. Willi. Laser-foil acceleration of high-energy protons in small-scale plasma gradients. *Phys. Rev. Lett.*, 99:015002, Jul 2007.
- [89] A P L Robinson, D Neely, P McKenna, and R G Evans. Spectral control in proton acceleration with multiple laser pulses. *Plasma Physics and Controlled Fusion*, 49(4):373, feb 2007.

- [90] Nashad Rahman, Joseph R. Smith, Gregory K. Ngirmang, and Chris Orban. Particle-in-cell modeling of a potential demonstration experiment for double pulse enhanced target normal sheath acceleration. *Physics of Plasmas*, 28(7):073103, 07 2021.
- [91] Imran Khan and Vikrant Saxena. Tnsa based proton acceleration by two oblique laser pulses in the presence of an axial magnetic field. *New Journal of Physics*, 26(8):083026, aug 2024.
- [92] A Arefiev, T Toncian, and G Fiksel. Enhanced proton acceleration in an applied longitudinal magnetic field. *New Journal of Physics*, 18(10):105011, oct 2016.
- [93] A. Morace, N. Iwata, and Y. Sentoku. Enhancing laser beam performance by interfering intense laser beamlets. *Nat Commun*, 10:2995, 7 2019.
- [94] Adam Paszke, Sam Gross, Francisco Massa, Adam Lerer, James Bradbury, Gregory Chanan, Trevor Killeen, Zeming Lin, Natalia Gimelshein, Luca Antiga, Alban Desmaison, Andreas Kopf, Edward Yang, Zachary DeVito, Martin Raison, Alykhan Tejani, Sasank Chilamkurthy, Benoit Steiner, Lu Fang, Junjie Bai, and Soumith Chintala. Pytorch: An imperative style, high-performance deep learning library. In H. Wallach, H. Larochelle, A. Beygelzimer, F. d'Alché-Buc, E. Fox, and R. Garnett, editors, *Advances in Neural Information Processing Systems*, volume 32. Curran Associates, Inc., 2019.
- [95] Sören Jalas, Manuel Kirchen, Philipp Messner, Paul Winkler, Lars Hübner, Julian Dirkwinkel, Matthias Schnepp, Remi Lehe, and Andreas R. Maier. Bayesian optimization of a laser-plasma accelerator. *Phys. Rev. Lett.*, 126:104801, Mar 2021.
- [96] E J Dolier, M King, R Wilson, R J Gray, and P McKenna. Multi-parameter bayesian optimisation of laser-driven ion acceleration in particle-in-cell simulations. *New Journal of Physics*, 24(7):073025, jul 2022.
- [97] B. Loughran, M. J. V. Streeter, H. Ahmed, S. Astbury, M. Balcazar, M. Borghesi, N. Bourgeois, C. B. Curry, S. J. D. Dann, S. DiIorio, and et al. Automated control and optimization of laser-driven ion acceleration. *High Power Laser Science and Engineering*, 11:e35, 2023.
- [98] B Z Djordjević, A J Kemp, J Kim, J Ludwig, R A Simpson, S C Wilks, T Ma, and D A Mariscal. Characterizing the acceleration time of laser-driven ion acceleration with data-informed neural networks. *Plasma Physics and Controlled Fusion*, 63(9):094005, aug 2021.

- [99] B. Schmitz, D. Kreuter, O. Boine-Frankenheim, and Daniele Margarone. Modeling of a liquid leaf target tnsa experiment using particle-in-cell simulations and deep learning. *Laser and Particle Beams*, 2023:e3, 2023.
- [100] Ronak Desai. Datasets and code from “applying machine learning methods to laser acceleration of protons: lessons learned from synthetic data”. <https://doi.org/10.5281/zenodo.12752264>, July 2024.
- [101] Ronak Desai and John J. Felice. Datasets and code from “towards automated learning with ultra-intense laser systems operating in the khz repetition rate regime”. <https://doi.org/10.5281/zenodo.14009491>, October 2024.
- [102] M. Passoni, L. Bertagna, and A. Zani. Target normal sheath acceleration: theory, comparison with experiments and future perspectives. *New Journal of Physics*, 12(4):045012, apr 2010.
- [103] J. Schreiber, F. Bell, F. Grüner, U. Schramm, M. Geissler, M. Schnürer, S. Ter-Avetisyan, B. M. Hegelich, J. Cobble, E. Brambrink, J. Fuchs, P. Audebert, and D. Habs. Analytical model for ion acceleration by high-intensity laser pulses. *Phys. Rev. Lett.*, 97:045005, Jul 2006.
- [104] M. H. Key, M. D. Cable, T. E. Cowan, K. G. Estabrook, B. A. Hammel, S. P. Hatchett, E. A. Henry, D. E. Hinkel, J. D. Kilkenny, J. A. Koch, W. L. Kruer, A. B. Langdon, B. F. Lasinski, R. W. Lee, B. J. MacGowan, A. MacKinnon, J. D. Moody, M. J. Moran, A. A. Offenberger, D. M. Pennington, M. D. Perry, T. J. Phillips, T. C. Sangster, M. S. Singh, M. A. Stoyer, M. Tabak, G. L. Tietbohl, M. Tsukamoto, K. Wharton, and S. C. Wilks. Hot electron production and heating by hot electrons in fast ignitor research. *Physics of Plasmas*, 5(5):1966–1972, 05 1998.
- [105] C. D. Decker, W. B. Mori, K.-C. Tzeng, and T. Katsouleas. The evolution of ultra-intense, short-pulse lasers in underdense plasmas. *Physics of Plasmas*, 3(5):2047–2056, 05 1996.
- [106] Don M. Miller. Reducing transformation bias in curve fitting. *The American Statistician*, 38(2):124–126, 1984.
- [107] RAPIDS Development Team. *RAPIDS: Libraries for End to End GPU Data Science*, 2023.
- [108] Jacob R Gardner, Geoff Pleiss, David Bindel, Kilian Q Weinberger, and Andrew Gordon Wilson. Gpytorch: Blackbox matrix-matrix gaussian process inference with gpu acceleration. In *Advances in Neural Information Processing Systems*, 2018.

- [109] Marian Tietz, Thomas J. Fan, Daniel Nouri, Benjamin Bossan, and skorch Developers. *skorch: A scikit-learn compatible neural network library that wraps PyTorch*, July 2017.
- [110] Ke Alexander Wang, Geoff Pleiss, Jacob R. Gardner, Stephen Tyree, Kilian Q. Weinberger, and Andrew Gordon Wilson. Exact gaussian processes on a million data points, 2019.
- [111] James Hensman, Alex Matthews, and Zoubin Ghahramani. Scalable variational gaussian process classification, 2014.
- [112] F. Treffert, C. B. Curry, H.-G. J. Chou, C. J. Crissman, D. P. DePonte, F. Fiuzza, G. D. Glenn, R. C. Hollinger, R. Nedbailo, J. Park, C. Schoenwaelder, H. Song, S. Wang, J. J. Rocca, M. Roth, S. H. Glenzer, and M. Gauthier. High-repetition-rate, multi-MeV deuteron acceleration from converging heavy water microjets at laser intensities of 10²¹ W/cm². *Applied Physics Letters*, 121(7):074104, 08 2022.
- [113] J. Snyder, J. T. Morrison, S. Feister, K. D. Frische, K. M. George, M. Le, C. Orban, G. Ngirmang, E. Chowdhury, and W. Roquemore. Background pressure effects on mev protons accelerated via relativistically intense laser-plasma interactions. *Scientific Reports*, 10, 2020.
- [114] Benjamin M. Knight, Connor M. Gautam, Colton R. Stoner, Bryan V. Egner, Joseph R. Smith, Chris M. Orban, Juan J. Manfredi, Kyle D. Frische, Michael L. Dexter, Enam A. Chowdhury, and et al. Detailed characterization of khz-rate laser-driven fusion at a thin liquid sheet with a neutron detection suite. *High Power Laser Science and Engineering*, 12:e2, 2024.
- [115] M. J. V. Streeter and et al. Stable laser-acceleraetion of high-flux proton beams with plasma collimation. *Nature Communications*, 16, 2025.
- [116] R.W. Hockney and J.W. Eastwood. *Computer Simulation Using Particles*. CRC Press, 1988.
- [117] R.W Hockney. Measurements of collision and heating times in a two-dimensional thermal computer plasma. *Journal of Computational Physics*, 8(1):19–44, 1971.
- [118] D.C. Montgomery and D.A. Tidman. *Plasma Kinetic Theory*. McGraw-Hill advanced physics monograph series. McGraw-Hill, 1964.

Appendix A

ENERGY CONSERVATION IN EPOCH PARTICLE-IN-CELL SIMULATIONS DUE TO FINITE NUMBERS OF PARTICLES

This appendix focuses on unpublished work that was done jointly with Ricky Oropeza and Joseph Smith. My contributions to this project were primarily done as a pre-candidacy student. PIC simulations provide a useful but imperfect model of various plasma phenomena. In this work, the impact of the finite number of particles in a PIC simulation on the energy conservation is considered and explored through ultra-intense laser interactions with a thin, near solid density target in the TNSA regime.

A.1 Background

Explicit PIC codes tend to gain energy over time through what can be attributed as numerical errors. In this section, we consider which plasma and simulation parameters affect this numerical energy gain and derive various scalings.

A.1.1 Electric Field Fluctuations

In PIC simulations, we compute the velocities at the next timestep through eq. (3.12) which is dependent on the time-step Δt . Due to using a finite grid, approximating real particles with macro particles, and using a finite Δt , we will develop some errors in calculating the electric field δE . The corresponding force miscalculation $\delta F = q\delta E\Delta t$ would deliver an impulse $m\delta v$ and result in a velocity difference [116] of

$$\delta v = \frac{q}{m} \Delta t \delta E \quad (\text{A.1})$$

We can make an assumption that these field calculation errors will be randomly distributed which can be treated as a random walk in velocity space. If we consider Δv as the total

deviation of the calculated velocity from the true value, we should expect $\langle \Delta v \rangle = 0$ due to the symmetry of this random walk. However, the squared deviations on average will increase over time; for n time-steps (each with the same random error δE), we would have

$$\langle \Delta v^2 \rangle = n\delta v^2 = n \frac{q^2}{m^2} \Delta t^2 \delta E^2 \quad (\text{A.2})$$

We can see that the average change in kinetic energy $\Delta KE \equiv \frac{1}{2}m\langle v^2 \rangle$ increases linearly with the number of time-steps n [116]. Additionally, since $\Delta KE \propto \frac{1}{m}$, the heavier particles (i.e. ions) can usually be neglected when examining the artificial heating [116]. Hockney postulates a related expression [117] for ΔKE in another work as

$$\Delta KE \sim \frac{q^2}{m} \langle E^2 \rangle \tau_{\text{corr}} \Delta t \quad (\text{A.3})$$

where τ_{corr} can be identified with the period of plasma oscillations $\sim \omega_{p,e}^{-1}$. Then, expressing the charge of one electron macro-particle as $q = e \frac{N}{N_{mac}} = \frac{en}{n_{mac}} = \frac{en\Delta x^2}{n_{ppc}}$, where Δx is the cell size²¹ and n_{ppc} is the number of electron macro-particles per cell, the kinetic energy increase becomes

$$\Delta KE = \left(\frac{e}{m_e}\right) \frac{en\Delta x^2}{n_{ppc}} \langle E^2 \rangle \frac{2\pi}{\omega_{pe}} \Delta t \quad (\text{A.4})$$

Hockney uses a result from Chapter 8.2 of Montgomery and Tidman [118] for the squared electric field fluctuations

$$\frac{\langle E^2 \rangle}{8\pi} = \frac{k_B T}{2} \int \int_{-\infty}^{+\infty} \frac{dk_x dk_y}{(2\pi)^2} \frac{1}{(1 + (k_x^2 + k_y^2)\lambda_D^2)} \quad (\text{A.5})$$

which can be solved by letting $u = k\lambda_D$ where $k = \sqrt{k_x^2 + k_y^2}$ and integrating with respect to the polar area element $k dk d\phi$

$$\langle E^2 \rangle = \frac{k_B T}{4\pi\epsilon_0\lambda_D^2} \text{Log}(1 + u_{max}^2) \quad (\text{A.6})$$

Here, $u_{max} = k_{max}\lambda_D$ corresponds to the maximum wavenumber $k_{max} = \frac{2\pi}{\Delta x}$ considered which is limited by the resolution.

A.1.2 Empirical Heating Estimates

Using Equations 2.17, 2.15, A.4, and A.6 ΔKE can now be expressed as

$$\Delta KE = \frac{n_e^{3/2} \Delta x^2}{n_{ppc}} \text{Log}(1 + u_{max}^2) \quad (\text{A.7})$$

²¹It is to the second power because we are focusing on a 2D simulation in this section.

An empirical estimate for the heating can be obtained by asserting a general scaling of the heating time $\tau_H \simeq \frac{n_{\text{ppc}}^\alpha}{\omega_{p,e}} \left(\frac{\lambda_{D,0}}{\Delta x} \right)^d$, where d (should be the dimension) and α are constants that can be fit through simulations. If we assert a linear energy increase with time $\frac{dT}{dt} = T_0/\tau_H$, we develop a formula (again using Equations 2.17 and 2.15) for the linear energy increase

$$\frac{dT_{eV}}{dt_{ps}} = C_H \frac{T_{0,eV}^{1-d/2} \Delta x_{nm}^d n_{23}^{(d+1)/2}}{n_{\text{ppc}}^\alpha} \quad (\text{A.8})$$

and when $\alpha = 1$ and $d = 2$, we obtain eq. (30) from Arber et al. [83]

$$\frac{dT_{eV}}{dt_{ps}} = C_H \frac{\Delta x_{nm}^2 n_{23}^{3/2}}{n_{\text{ppc}}} \quad (\text{A.9})$$

where C_H is a constant determined by the shape function and the use of current smoothing. This looks notably similar to Equation A.7 without the log term which helps motivate its physical origin. The cell size, number density, time, and temperature are expressed in nm, 10^{23}cm^{-3} , ps, and eV due to being convenient units for PIC simulations. A more sophisticated empirical model could also account for two dimensionless timescales: $\omega_{p,e}\Delta t$ and $v_{\text{th}}\Delta t$, but Hockney [117] notes that these can be ignored by constraining $\omega_{p,e}\Delta t$ to be $\omega_{p,e}\Delta t = \min((2\lambda_D/\Delta x)^{-1}, 1)$ [117].

A.2 Simulation

A.2.1 Methods

A number of simulations were performed using the EPOCH code with a 2D(3v) geometry. The laser and target was based on the experimental facility at **WP-ELL** described in chapter 6 and the relevant simulation parameters are listed in Table A.1. The laser emerges perpendicularly from one of the boundaries and is incident on a diagonally oriented target with incidence angle 45° . The target was initialized with all ions singly ionized (C^+ , O^+ , H^+) with abundances in proportion to the chemical composition of ethylene glycol. The simulations ran for 500 fs and the energy acquired in protons, electrons, carbon, and oxygen was tracked throughout this time. This energy is highlighted in Figure A.1 for a simulation with many particles per cell that has a minimal amount of numerical heating.

A.2.2 Results

According to Equation A.9, if the number of particles per cell is low, one should expect more numerical heating and the energy in electrons (the green region in Figure A.1) to be larger than expected. However, in this simulation setup, there are multiple species which can all have different numbers of particles per cell. From running these simulations, it became clear that the electron particles per cell is not the only relevant number (even

Laser	Wavelength: Peak Intensity Pulse Duration: Spot Size	780 nm: $2.1671\text{e}18 \text{ W cm}^{-2}$ 42 fs FWHM: $1.87 \mu\text{m}$ FWHM
Target	Material Density Thickness	Ionized Ethylene Glycol $2 \times 10^{22} \text{ cm}^{-3}$ 460 nm
Sim	Resolution Total Time Initial Particle Temperature Simulation Area	10 nm 500fs 1 eV $28 \mu\text{m} \times 28 \mu\text{m}$

Table A.1: Summary of Simulation Parameters (constant)

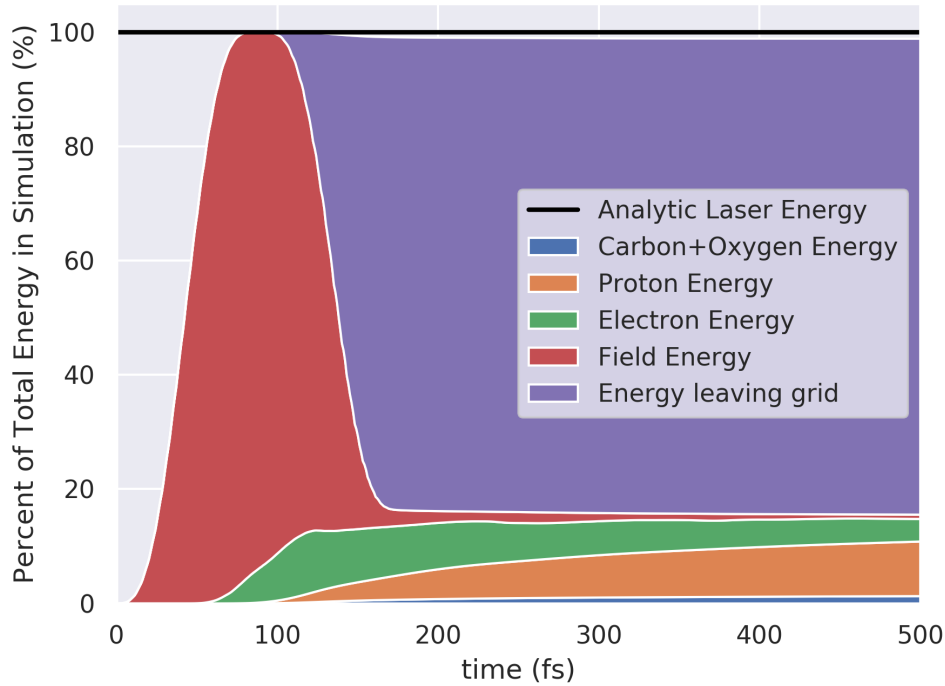


Figure A.1: The total energy and how it is distributed over time in the simulation. The black line is amount of energy that should be in the system from the laser pulse in the simulation.

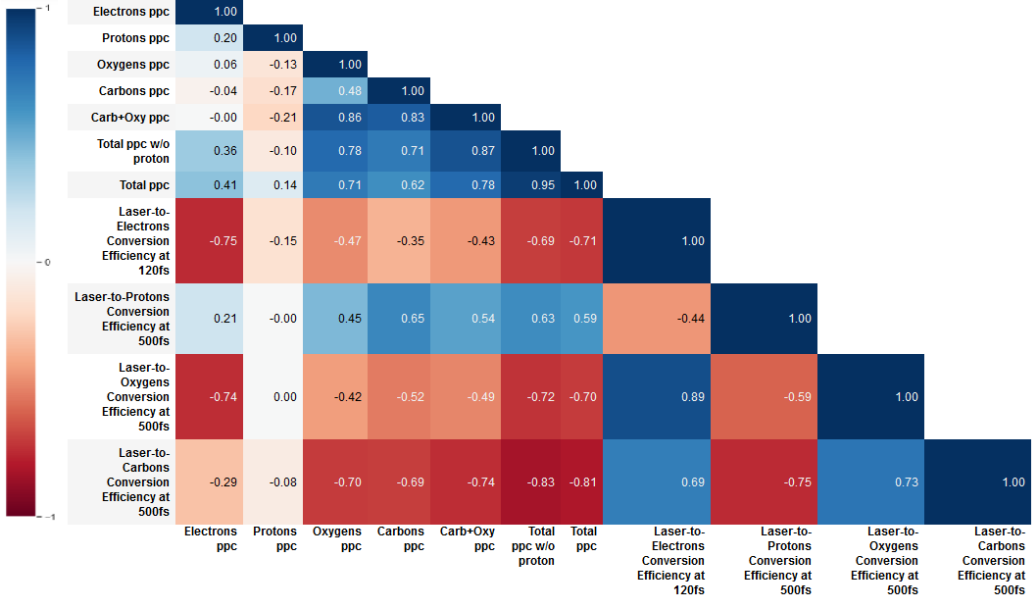


Figure A.2: A spearman correlation matrix of the inputs and outputs of all the simulations

though it is the most influential). When oxygen and carbon ionize, they release electrons, so the carbon and oxygen particles per cell should also be important quantities that arise in a scaling like [Equation A.9](#). To analyze the effect of varying the number of particles per cell, we conducted a set of 44 simulations that are listed in [Table A.2](#). The specific numbers of particles per cell were chosen by utilizing a Sobol sequence which attempts to fill up the 4D parameter space (particles per cell for each species) in such a way to not leave large gaps ([CITATION](#)). This table clearly shows how changing the number of particles per cell (in an otherwise identical simulation setup) influences the amount of energy that gets delivered to each species. The true conversion efficiencies should be close to the values for the simulations with many particles per cell (e.g. simulations 42 and 43) and conversion efficiencies higher than these simulations should be regarded as numerical effects.

To analyze which factors influence the numerical heating gain, we first looked at a spearman correlation matrix in [Figure A.2](#) which can show the correlations between the relevant simulation inputs and outputs in [Table A.2](#). When looking at the row with the electron conversion efficiency – which is the quantity most relevant to artificial heating – we see that the electron particles per cell has the strongest correlation. However, the correlations with oxygen and carbon particles per cell are not negligible either. As mentioned earlier, the non-zero correlations should be influenced by the electrons that get ionized from carbon and oxygen throughout the simulations. From this physical insight, I came up with a formula to modify the electron particles per cell to the effective particles per cell

Sim #	$n_{\text{ppc,e}}$	$n_{\text{ppc,p}}$	$n_{\text{ppc,O}}$	$n_{\text{ppc,C}}$	$n_{\text{ppc,total}}$	η_e at 120fs	η_p at 500fs	η_O at 500fs	η_C at 500fs
1	5.0	38.0	42.0	59.0	144.0	11.435	9.672	0.816	0.671
2	7.0	121.0	60.0	100.0	288.0	11.260	9.748	0.817	0.643
3	9.0	9.0	9.0	9.0	36.0	11.977	6.917	1.158	0.887
4	9.0	9.0	9.0	9.0	36.0	11.907	6.881	1.137	0.868
5	15.0	94.0	173.0	100.0	382.0	11.198	9.552	0.811	0.642
6	18.0	52.0	145.0	200.0	415.0	11.114	9.567	0.781	0.631
7	20.0	66.0	118.0	45.0	249.0	11.190	9.171	0.808	0.660
8	23.0	23.0	164.0	255.0	465.0	11.032	9.368	0.781	0.641
9	26.0	37.0	282.0	136.0	481.0	11.051	9.368	0.758	0.633
10	29.0	86.0	36.0	164.0	315.0	11.107	9.119	0.786	0.669
11	29.0	86.0	36.0	36.0	187.0	11.134	8.695	0.826	0.685
12	29.0	86.0	36.0	36.0	187.0	11.113	8.635	0.807	0.685
13	32.0	77.0	227.0	227.0	563.0	10.953	9.300	0.759	0.634
14	35.0	35.0	54.0	54.0	178.0	11.065	8.915	0.791	0.678
15	35.0	35.0	54.0	54.0	178.0	11.045	8.916	0.783	0.664
16	37.0	26.0	100.0	173.0	336.0	11.046	9.329	0.749	0.646
17	40.0	74.0	218.0	127.0	459.0	10.984	9.308	0.758	0.637
18	43.0	43.0	191.0	264.0	541.0	10.978	9.432	0.730	0.627
19	46.0	91.0	91.0	36.0	264.0	11.030	8.938	0.768	0.667
20	49.0	60.0	64.0	209.0	382.0	10.980	9.335	0.727	0.636
21	52.0	18.0	255.0	91.0	416.0	10.990	9.298	0.748	0.658
22	54.0	54.0	154.0	154.0	416.0	10.947	9.352	0.727	0.630
23	57.0	12.0	127.0	145.0	341.0	11.106	9.465	0.732	0.651
24	60.0	49.0	27.0	27.0	163.0	11.111	8.655	0.782	0.691
25	60.0	49.0	27.0	27.0	163.0	11.102	8.661	0.783	0.679
26	60.0	49.0	27.0	245.0	381.0	11.071	9.330	0.712	0.652
27	63.0	97.0	291.0	54.0	505.0	10.954	9.281	0.744	0.637
28	66.0	20.0	264.0	191.0	541.0	11.018	9.543	0.738	0.650
29	69.0	69.0	18.0	18.0	174.0	11.117	8.319	0.819	0.705
30	69.0	69.0	18.0	18.0	174.0	11.108	8.339	0.809	0.717
31	74.0	40.0	182.0	18.0	314.0	11.043	8.949	0.774	0.649
32	77.0	32.0	82.0	82.0	273.0	10.965	9.376	0.734	0.653
33	83.0	72.0	245.0	27.0	427.0	10.960	9.160	0.739	0.641
34	86.0	29.0	73.0	273.0	461.0	10.999	9.560	0.704	0.634
35	89.0	89.0	45.0	118.0	341.0	10.893	9.352	0.701	0.643
36	91.0	46.0	236.0	182.0	555.0	10.887	9.563	0.698	0.622
37	94.0	15.0	209.0	64.0	382.0	10.948	9.401	0.724	0.648
38	97.0	63.0	109.0	236.0	505.0	10.895	9.587	0.703	0.626
39	119.0	119.0	70.0	70.0	378.0	10.885	9.397	0.712	0.644
40	131.0	82.0	131.0	131.0	475.0	10.800	9.557	0.689	0.614
41	187.0	203.0	11.0	13.0	414.0	11.061	8.580	0.783	0.725
42	257.0	64.0	92.0	58.0	471.0	10.852	9.663	0.694	0.619
43	257.0	64.0	92.0	58.0	471.0	10.834	9.611	0.687	0.624
44	294.0	164.0	32.0	41.0	531.0	10.915	9.484	0.713	0.652

Table A.2: Particles per cell and conversion efficiencies for all 44 simulations.

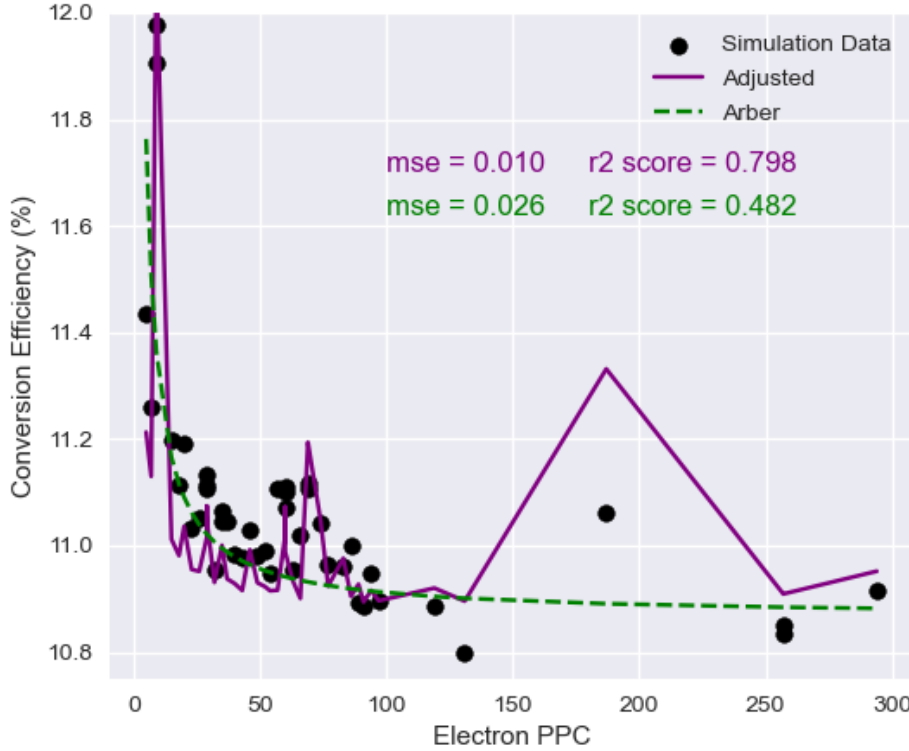


Figure A.3: Plot of Arber et al. model (Equation A.9) compared to the effective particle per cell model (using Equation A.10) plotted against the electron particles per cell.

$$\frac{1}{n_{\text{ppc,eff}}} = \frac{1}{n_{\text{ppc,e}}} + \frac{Z_O^* - 1}{n_{\text{ppc,O}}} + \frac{Z_C^* - 1}{n_{\text{ppc,C}}} \quad (\text{A.10})$$

where Z_O^* and Z_C^* are the effective ionization states²² of oxygen and carbon that were extracted from the simulations and reported in Table A.3. These ionization states were calculated by taking a sum of the ionization state (e.g. $Z = 1, 2, 3, \dots$) weighted by the macro-particle count in each state and dividing by the total macro-particle count.

In Figure A.3, the original Arber scaling from Equation A.9 and adjusted scaling (with Equation A.10) are plotted as a green dashed line and purple solid line with a scatter plot of the simulation data. While the Arber model is a smooth function of the electron particles per cell, the data clearly has points where it jumps up and down which the adjusted model captures more of. It is important to note that both models only used one free parameter: the heating constant C_H from Equation A.9. The plot itself shows the r^2 correlation score

²²The ionization states were subtracted by 1 because the simulation started out singly ionized.

Sim #	Z_O^*	Z_C^*
1	2.176142756	2.375174888
2	2.327658955	2.421891557
3	3.143308831	2.915937614
4	3.154803787	2.927684972
5	2.496638636	2.527135231
6	2.441216019	2.508804562
7	2.584687195	2.627203273
8	2.387585622	2.486757853
9	2.392126498	2.531181839
10	2.564046446	2.634346386
11	2.543839748	2.644390761
12	2.412445491	2.530124101
13	2.291655813	2.471869382
14	2.421709685	2.575093874
15	2.406534033	2.577752667
16	2.264716398	2.48188157
17	2.246043951	2.485791191
18	2.178764825	2.432073341
19	2.361060481	2.5738224
20	2.167570944	2.425260178
21	2.185477012	2.443200305
22	2.140609639	2.414440722
23	2.126992307	2.407471987
24	2.142192439	2.403501354
25	2.393986109	2.625379573
26	2.412863167	2.619551359
27	2.17524236	2.480400199
28	2.046239782	2.345317225
29	2.518141858	2.688972667
30	2.514367481	2.694657044
31	2.372678171	2.648680619
32	2.071785068	2.380991226
33	2.208017982	2.547074535
34	1.992876487	2.30745977
35	2.046732563	2.365068347
36	1.952194826	2.286210998
37	2.035659427	2.37849725
38	1.930691366	2.266609743
39	1.987261106	2.345904477
40	1.897934111	2.254506282
41	2.494837238	2.719446774
42	1.878585202	2.274410676
43	1.870289532	2.27367933
44	1.961455166	2.362095052

Table A.3: Effective ion charge for all simulations

and [MSE](#) which is more favorable for the model adjusted to effective particles per cell.

A.3 Conclusion

Throughout this chapter, I explored a common question that many simulation researchers face: how many particles per cell should be utilized per species in a [PIC](#) simulation? I first addressed this question theoretically by building upon the work of Hockney and Eastwood [116] and Arber et al. [83]. Then, I utilized a set of 2D [PIC](#) simulations²³ to evaluate the effectiveness of the Arber et al. model ([Equation A.9](#)) with and without the effective particle per cell adjustment ([Equation A.10](#)) in capturing the data. While the Arber et al. model definitely has correct trends with the electron particles per cell, it does not fully capture information about the other species. The effective particle per cell is a better predictor of the numerical heating, but not perfect by any means.

To continue this work, I believe an extensive set of thousands of [PIC](#) simulations would need to be conducted over a more exhaustive combination of particles per cell. These simulations should also be performed over several different resolutions (i.e. $\lambda_D/\Delta x$) due to making a noticeable difference in the scaling properties of the numerical heating from my own experience. Current simulation practitioners rely on an archaic method of deciding the numbers of particles per cell: starting out at a low resolution and increasing resolution and particles per cell until the simulation results stay relatively consistent. With modern day advances in computing clusters and machine learning capabilities, I believe that more useful empirical estimates can be developed to both understand the nature of numerical heating better and save time for computational scientists.

²³These were conducted by Ricky Oropeza.